

# TASK-SPECIFIC UNCERTAINTY FOR POINT CLOUD MEASUREMENTS

by

Pooya Sharifani

A dissertation submitted to the faculty of  
The University of North Carolina at Charlotte  
in partial fulfillment of the requirements  
for the degree of Doctor of Philosophy in  
Mechanical Engineering

Charlotte

2024

Approved by:

---

Dr. Edward Morse

---

Dr. Jimmie Miller

---

Dr. Konstantinos Falaggis

---

Dr. Wesley Williams



## ABSTRACT

POOYA SHARIFANI. Task-Specific Uncertainty for Point Cloud Measurements.  
(Under the direction of DR. EDWARD MORSE)

In this research, we have developed a data fusion technique to integrate the measurement point clouds collected from a workpiece. One dataset was obtained using a high-accuracy, low-density, and low-throughput tool, and a low-accuracy, high-density, and high-throughput instrument generated the other dataset. By fusing these two datasets we were able to achieve a high-accuracy and high-density point cloud of the workpiece. This will speed up the required time needed to measure the industrial parts at scale. To develop this model, we first generated a 1D simulation as a proof of concept for our study. Next, this model was expanded to a 2D simulation, and performed the fusion test on a workpiece surface. Then, the fusion model was applied to a cylindrical shape workpiece in 3D. Our results suggest that the fusion model that we have developed in this work can be utilized at various scales to make high-density, high-accuracy, and high-throughput measurements of industrial parts feasible.

## DEDICATION

To my dearest mother and father for doing their best in their life to nourish me with their values and give me strength to strive for what it is worth to become the best version of myself.

To my beloved soulmate for her endless love and unforgettable support throughout this long journey. Your sacrifices to grant me the opportunity to achieve this will remain in my mind forever. To my only brother for his never-ending endeavor for advancement and making my world more cheerful.

## ACKNOWLEDGEMENTS

I want to acknowledge the immense amount of help and support from my Ph.D. advisor, Dr. Edward Morse, for his enlightening profound knowledge during the years of my doctoral study. I am thankful to my committee members for their bright ideas and productive support throughout this study. I am grateful to the affiliates program at CPM (Center for Precision Metrology - UNC Charlotte) for their unwavering support during the years of this study by holding informative semi-annual meetings to contribute to key projects that address specific concerns in manufacturing metrology. These meetings brought the opportunity to discuss the technical details and review the progress of our industrial projects with industry leaders. Also, it is important to mention the great support from the ASPE student chapter at UNCC to provide a collaborative environment to help students pursue excellence in their research. I want to thank Dr. Katherine Hall-Hertel, Dr. Lisa Russell-Pinson, and Dr. Yuri Godin for their kind support above and beyond their responsibilities. Last but not least, I thank my friends for building a constructive and collaborative studying atmosphere to grow and learn.

## Table of Contents

List of Figures .....	ix
1 Introduction.....	1
2 Literature review .....	6
2.1 Multisensor data fusion .....	6
2.2 Operations on multisensor data fusions .....	9
2.3 Sensor technologies for dimensional measurement.....	10
2.3.1 Optical sensors .....	10
2.3.2 Triangulation sensors.....	11
2.3.3 Deflectometry .....	11
2.3.4 Confocal microscopy.....	11
2.3.5 White light interferometry .....	12
2.3.6 Focus variation.....	12
2.3.7 Image sensor .....	12
2.3.8 Tactile sensors.....	12
2.3.9 Computed tomography .....	14
2.3.10 Scanning probe microscopy.....	14
2.4 Data fusion in metrology.....	15
2.4.1 Computed Tomography (CT) .....	16
2.4.2 Scanning probe microscopy:.....	16

2.5	Multisensor CMMs.....	16
2.5.1	Multi-source Remote Sensing Data Fusion.....	18
2.5.2	Structure in laser scanner point clouds .....	19
2.5.3	Extraction of smooth surfaces.....	19
2.6	Measurement uncertainty in performance verification .....	20
3	Methodology.....	22
3.1	Experimental design and setup .....	22
3.2	1D model.....	27
3.2.1	Polynomial fitting and moving average .....	28
3.2.2	Spline fitting and moving averages .....	31
3.2.3	Spline fitting and Gaussian filtering.....	32
3.3	2D model.....	35
3.3.1	Building surface point grids.....	35
3.3.2	Fusion process.....	39
3.4	2D experiment.....	44
3.4.1	Instruments and workpiece specs.....	44
3.4.2	CMM measuring strategy .....	48
3.4.3	Laser scanner measuring strategy .....	67
3.4.4	Data fusion strategy .....	71
3.4.5	Data fusion analysis.....	76

3.5	3D experiment.....	78
4	Results .....	82
4.1	1D model.....	82
4.1.1	Polynomial and moving average fitting .....	82
4.1.2	Spline fitting and moving averages .....	86
4.1.3	Spline fitting and Gaussian filtering.....	89
4.2	2D model.....	93
4.3	2D experiment.....	100
4.3.1	Data acquisition .....	100
4.3.2	Data fusion.....	104
4.3.3	Data fusion analysis.....	112
4.4	3D experiment.....	126
5	Discussion.....	132
6	Conclusion.....	135
	References .....	136



## List of Figures

Figure 1. Collaborative radar data collection and multi-radar data fusion.....	2
Figure 2. Multisensor 3D coordinate vision measurement in the industry .....	2
Figure 3. Modeling a door handle.....	3
Figure 4. Registering process of images with different angles .....	4
Figure 5. Data stitching model.....	4
Figure 6. Methods for data acquisition .....	8
Figure 7. Different methods of data acquisition .....	10
Figure 8. Influence of tactile probing system .....	13
Figure 9. Different illumination parameters in image fusion.....	15
Figure 10. High accuracy dataset.....	23
Figure 11. Fitted high-accuracy data points .....	23
Figure 12. Fitter lower accuracy dataset .....	24
Figure 13. Fitted lower accuracy dataset with defect.....	25
Figure 14. High and low accuracy datasets.....	25
Figure 15. Two high-density datasets stitched together .....	26
Figure 16. Low accuracy dataset systematic error .....	27
Figure 17. Low pass, High pass, and Bandpass filters.....	34
Figure 18. Low-density measured points.....	37
Figure 19. High-density measured points.....	38
Figure 20. High-density measured surface.....	39
Figure 21. CMM: Leitz PMM-F 30.20.16 .....	44
Figure 22. Laser Scanner: Romer Absolute Arm – 7525 SEI .....	45

Figure 23. Aluminum workpiece used for the 2D experiment with a local thermometer on the rotary table .....	46
Figure 24. CMM ambient thermometer.....	47
Figure 25. Workpiece measured by articulate arm laser scanner .....	48
Figure 26. USECSY command: select a defined coordinate system for the tool .....	49
Figure 27. Set the active probe on the tool.....	50
Figure 28. Selecting the prob to be mounted on the holder.....	50
Figure 29. CMM ram taking stylus from the rack .....	51
Figure 30. Defining artifact by the "DfnArtefact" .....	52
Figure 31. Artifact specs.....	52
Figure 32. "QualifyTool" command settings .....	53
Figure 33. Artifact north pole touch from Quindos software .....	54
Figure 34. Rotary table coordinate system calibration.....	54
Figure 35. Create a coordinate system with 3 planes .....	55
Figure 36. Create a coordinate system from 2 planes and a center bore.....	56
Figure 37. Create a coordinate system by 1 plane, a center bore, and a directing cylinder .....	56
Figure 38. Create a plane on a surface with 3 points .....	57
Figure 39. Create an axis using 2 points .....	58
Figure 40. Create a circle by measuring 3 points .....	58
Figure 41. Create a coordinate system based on 3 elements .....	59
Figure 42. Create circular points to measure the plane surface .....	60
Figure 43. Collect nominal points .....	60

Figure 44. Coordinate system on the workpiece .....	61
Figure 45. 135 points for the high-accuracy low-density dataset.....	62
Figure 46. OPEN a new file on QUINDOS .....	63
Figure 47. For loop command .....	64
Figure 48. Save the script .....	65
Figure 49. 4680 points for the high-accuracy high-density dataset .....	66
Figure 50. Articulate arm laser scanner over the part.....	68
Figure 51. Laser scanner raw dataset of the part.....	69
Figure 52. A new coordinate system on the workpiece geometry acquired by the laser scanner.....	71
Figure 53. Freeform surface workpiece and the CMM stylus tip .....	71
Figure 54. Correction for the stylus nominal height through the surface slope.....	72
Figure 55. Stylus height adjustment based on surface partial derivative.....	73
Figure 56. High-density low-accuracy and low-density high-accuracy datasets.....	73
Figure 57. Gaussian filtered defects from high-density low-accuracy dataset.....	74
Figure 58. Separated points from the Gaussian-filtered high-density low-accuracy dataset .....	75
Figure 59. Subtracting 135 points laser arm data from their CMM points counterparts .....	75
Figure 60. Interpolated CMM defect-free points .....	76
Figure 61. Adding the extracted local defects to the CMM defect-free interpolated dataset.....	76
Figure 62. steam turbine exhaust muffler used for the 3D data fusion .....	78

Figure 63. ATOS GOM 3D Scan to measure the aerial topography.....	79
Figure 64. High-density point cloud of the cylinder part which measured by the 3D scanner.....	79
Figure 65. The cylinder part on the CMM rotary table .....	80
Figure 66. High-accuracy low-density point cloud collected by CMM.....	80
Figure 67. Alignment markers on part surface front view and top cross-section .....	81
Figure 68. High accuracy points.....	82
Figure 69. Polynomial fitted high accuracy points .....	83
Figure 70. Low accuracy dataset .....	84
Figure 71. Low accuracy moving average.....	84
Figure 72. Difference between low accuracy and its moving average.....	85
Figure 73. High-accuracy dataset with high-frequency offsets .....	86
Figure 74. Spline fitted high accuracy points.....	86
Figure 75. 15 and 45 moving averages on Low accuracy points.....	87
Figure 76. 15 and 45 moving average difference .....	88
Figure 77. The difference between 15 and 45 moving averages is added to the H.A. fitted curve.....	89
Figure 78. Gaussian filtering and 15 moving average difference on low accuracy dataset .....	90
Figure 79. Gaussian fitting and 15 points moving average difference over the low accuracy dataset added to the high accuracy fitted curve.....	91
Figure 80. Gaussian filtering and 45 moving average difference on low accuracy dataset .....	91

Figure 81. Gaussian fitting and 45 points moving average difference over the low accuracy dataset added to the high accuracy fitted curve .....	92
Figure 82. The actual surface model with defects and no noise.....	93
Figure 83. Low-density high-accuracy dataset.....	94
Figure 84. High-density, low-accuracy dataset.....	94
Figure 85. Gaussian-filtered defects from low-accuracy high-density dataset.....	95
Figure 86. Condensing the high-accuracy dataset by interpolation .....	95
Figure 87. Estimated surface fused from both channels .....	96
Figure 88. Actual surface and fused data difference .....	97
Figure 89. Low-density dataset Interpolation methods comparison with the initial actual surface.....	97
Figure 90. Difference between actual surface and fusion result made by linear interpolation.....	98
Figure 91. Difference between actual surface and fusion result made by spline interpolation.....	98
Figure 92. Difference between actual surface and fusion result made by cubic interpolation.....	98
Figure 93. Difference between actual surface and fusion result made by Akima interpolation.....	99
Figure 94. Rectangular probing path for part measurement (100 points) .....	100
Figure 95. Workpiece topography by a rectangular grid (100 points).....	101
Figure 96. Radial probing path for part measurement (135 points) .....	102
Figure 97. Workpiece topography by a radial grid (135 points) .....	102

Figure 98. Radial probing path for part measurement (4680 points) .....	103
Figure 99. Workpiece topography by a radial grid (4680 points) .....	103
Figure 100. 135 CMM points and 26400 laser scanner points aligned.....	105
Figure 101. Separated 26400 laser scanner points with the same circumference as the CMM dataset .....	105
Figure 102. Gaussian low-pass filtered defects on arm dataset.....	106
Figure 103. Gaussian high-pass filtered defects on arm dataset .....	107
Figure 104. Gaussian-filtered defects from high-density low-accuracy dataset.....	108
Figure 105. 135 points from Gaussian-filtered high-density dataset that are nearest neighbors to the CMM points .....	109
Figure 106. Subtracted defects from the CMM points .....	110
Figure 107. V4 interpolated defect-free CMM dataset.....	111
Figure 108. Data fusion result from the CMM and laser scanner .....	112
Figure 109. $\Delta Z$ of High-density low-accuracy vs. generated fused dataset.....	113
Figure 110. $\Delta Z$ of High-density low-accuracy vs. generated fused dataset histogram .....	113
Figure 111. 135 CMM points vs. nearest neighbor points from 4680 reference CMM dataset.....	114
Figure 112. $\Delta Z$ histogram of the reference 4680 and 135 CMM points datasets .....	115
Figure 113. Reference 4680 CMM points vs. their nearest neighbors from the laser scanner dataset.....	116
Figure 114. $\Delta Z$ histogram of reference 4680 points and their laser scanner nearest neighbors .....	116

Figure 115. Reference 4680 CMM points vs. their nearest neighbor fusion	
points (135 CMM points) .....	117
Figure 116. $\Delta Z$ histogram of the 4680 reference CMM points and their	
nearest neighbor fusion points (135 CMM points) .....	118
Figure 117. 75 CMM points serve as a low-density, high-accuracy dataset.....	119
Figure 118. 45 CMM points serve as low-density, high-accuracy dataset.....	119
Figure 119. 15 CMM points serve as low-density, high-accuracy dataset.....	120
Figure 120. Reference 4680 CMM points vs. their nearest neighbor fusion	
points (75 CMM points) .....	121
Figure 121. $\Delta Z$ histogram of 4680 reference CMM points and their nearest	
neighbor fusion points (75 CMM points).....	121
Figure 122. Reference 4680 CMM points vs. their nearest neighbor fusion	
points (45 CMM points) .....	122
Figure 123. $\Delta Z$ histogram of 4680 reference CMM points and their nearest	
neighbor fusion points (45 CMM points).....	123
Figure 124. Reference 4680 CMM points vs. their nearest neighbor fusion	
points (15 CMM points) .....	124
Figure 125. $\Delta Z$ histogram of 4680 reference CMM points and their nearest	
neighbor fusion points (15 CMM points).....	124
Figure 126. Benchmark CMM points vs. raw and fusion datasets.....	125
Figure 127. CMM and 3D scanner point cloud alignment.....	126
Figure 128. Raw CMM point cloud .....	127
Figure 129. Raw 3D scanner point cloud .....	127

Figure 130. Gaussian-filtered defects from high-density dataset .....	128
Figure 131. Distances between the CMM points and their corresponding nearest neighbors .....	128
Figure 132. The defect-free surface of the cylinder .....	129
Figure 133. Linear interpolation of the defect-free dataset .....	130
Figure 134. The point cloud of the data fusion result .....	130
Figure 135. Histogram of the distances between data fusion and raw high-density dataset .....	131



## 1 Introduction

Data fusion is a vital concept in dimensional metrology because it provides more accurate topography and reduces the uncertainty of the workpiece model by using diverse measurements. These measurements are generated using one or more measuring devices. The purpose of data fusion is to combine various measurements so that the specification of each instrument can reduce the fused result uncertainty.

Data fusion is the process of combining data from several information sources (sensors) into a common representational format so that the metrological evaluation can benefit from all available sensors' information and data. The basic motivation is the improvement in the quality and usability of the measurement result. In image fusion we overlay, and fuse images of the same scene taken at different angles, times, or by different sensors. [1-4]

Data fusion has a broad application in different industries including manufacturing, biomedical, meteorology, image processing, and many more. For example, as shown in Figure 1, in meteorology to forecast the weather in a particular area, information could be provided from different satellites and ground weather stations, and it is important to integrate and analyze these datasets efficiently via data fusion.[5-7]

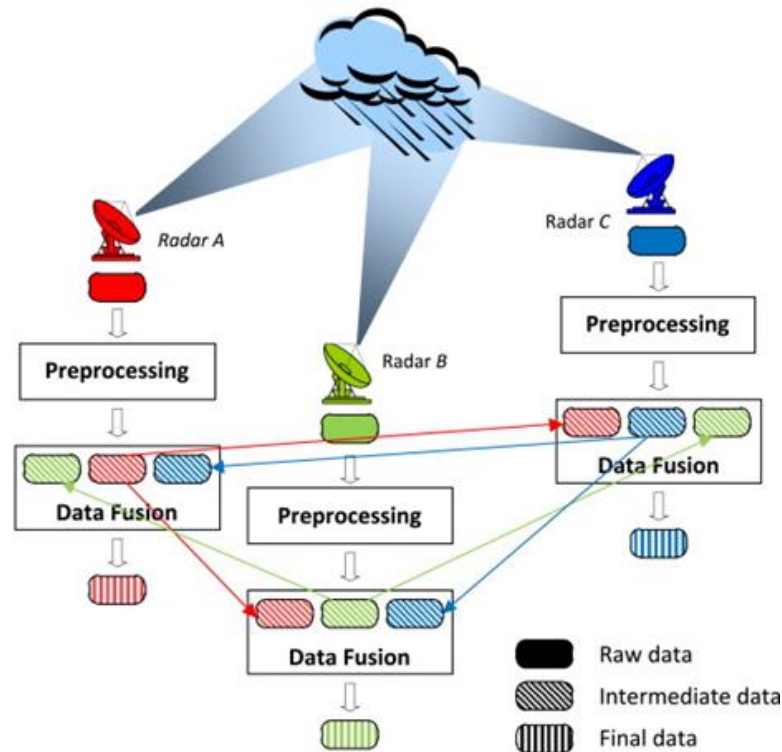


Figure 1. Collaborative radar data collection and multi-radar data fusion [7]

Another example in the automotive industry would be tire manufacturing where the vibration elimination on tires highly depends on the precise symmetry of the features of different axes of the tire. Hence, for prototype testing engineers check the surface features upon the different angles to build an overall surface geometry (Figure 2).[1]

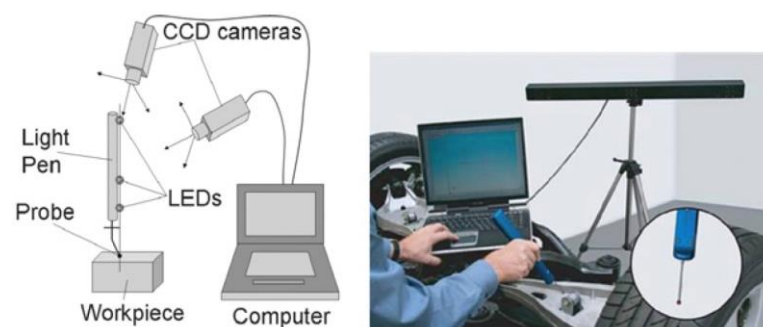


Figure 2. Multisensor 3D coordinate vision measurement in the industry [1]

Another example according to Figure 3 would be combining multiple sensors based on various sensitivities to generate a point cloud of the part geometry. Each of these tools may have advantages and disadvantages compared to one another. Selecting the right tool to achieve higher accuracy in the shortest possible time is the intention behind this approach. Therefore, setting up the right strategy to achieve this goal depends on the tools' specifications and workpiece features.[1, 8, 9]

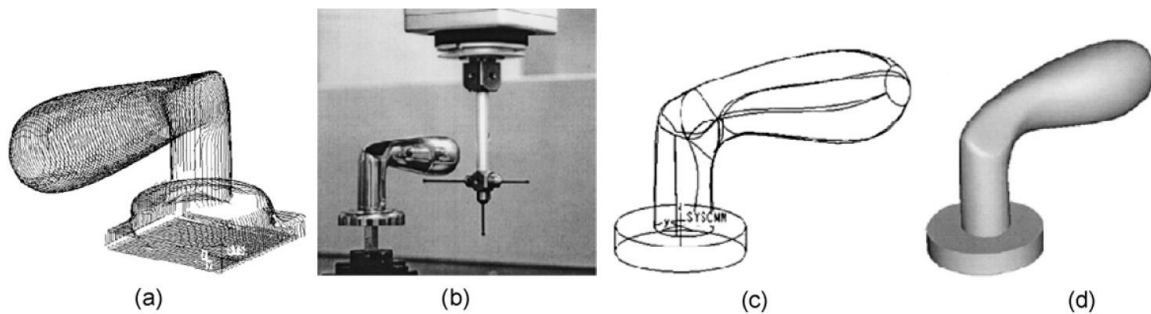


Figure 3. Modeling a door handle (a) Point clouds obtained by the optical sensor, (b) CMM measurements, (c) Aligning the coordinate systems of datasets, (d) Generating part model by data fusion [1]

Before the data fusion step, during which the measurement data is captured in the respective sensors, coordinate systems need to be aligned and transformed into one common coordinate system that overlays two or more images from various imaging equipment or sensors taken at different times and angles which is called registration as illustrated in Figure 4. In other words, registration is the transformation(s) of coordinate systems that bring single-view coordinates into a unified coordinate system.[10, 11]



Figure 4. Registering process of images with different angles [12]

Stitching is a precise method of complex surface measurement, which requires a large area from a homogeneous sensor as shown in Figure 5. This can be obtained by stitching individual measurements together. This registration is based on the sensors' positioning towards the object being measured. Stitching interferometry can provide a two-dimensional metrology map of the surface under test with sub-nanometer height resolution and precision.[13]

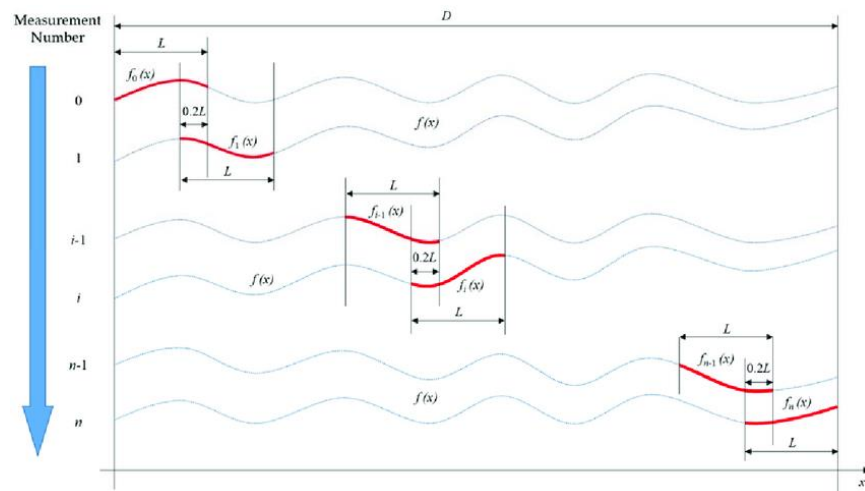


Figure 5. Data stitching model [14]

In the past, technicians would spend long hours on accurate devices to collect high-accuracy point clouds of a workpiece which could increase the manufacturability cost of a project. Data fusion is a great method to speed up the inspection process. Hence, data fusion can benefit many industries that need fast and accurate measurement at the same time. The niche of a robust toolbox to integrate the datasets from different devices that have measured the same workpiece with various accuracies is what can be developed to answer this demand.

In this work, we have used the data fusion technique to first start with integrating two datasets into the 1D model, then expand it to the 2D model, and finally apply it to 2D and 3D workpieces to pragmatically generate fused surface topography. For this experiment, we have used the CMM as our high-accuracy measuring device and the articulate arm laser scanner as our high-density device. This fused dataset from these two devices would potentially benefit from both measuring tools to have high-accuracy and high-density.

## 2 Literature review

Data fusion is a vital concept in dimensional metrology because it provides more accurate topography and reduces the uncertainty of the workpiece model by using various measurements. These measurements are generated using one or more measuring devices. The purpose of data fusion is to combine various measurements so that the specifications of each instrument can reduce the fused result uncertainty.

### 2.1 Multisensor data fusion

The synergistic effect can improve the performance of the system by increasing spatial and temporal coverage resulting in enhanced resolution, increasing robustness to uncertainty, suppressing noises, and improving accuracy.[15]

Homogenous sensors are the sensors that capture the same (or relatively same) physical measurands.[1] However, inhomogeneous sensors capture different features of a scene. Pre-processing information such as feature extraction, classification, and data compression is necessary when using inhomogeneous sensors.

Large volume metrology or LVM is the simultaneous use of different systems such as laser trackers and 3D scanners.[1] Applications of large-volume metrology in industry include the assembly of instrument components with large sizes and the reconstruction of surfaces to ensure the accuracy of measured sizes. Multisensor data fusion systems can be categorized into competitive, cooperative, and complementary integrations based on their sensors' configurations.[16] In the competitive approach, each instrument measures the target points independently and the redundant information is fused by evaluating the mean of each pixel. SpatialAnalyzer is a widely

used software for large-volume metrology applications. On the other hand, in a cooperative strategy, data is collected using two or more independent sensors from a single system or different ones. In this method, the information collected cannot be obtained from individual sensors but is rather the combination of all sensors.[4] For instance, data collected from one sensor might contain distance measurement information while another sensor in the same system gathered angular measurements. The combination of all data gathered results in the 3D measurements of a workpiece. A practical example of cooperative sensor configuration is a coordinate measuring machine (CMM) that integrates different high-precision sensors and computes topography based on the collected points.

Complementary sensor configuration happens when sensors do not directly depend on each other but are combined to obtain a more comprehensive image of the measurand under observation. For instance, images obtained by homogenous sensors that show different locations on the surface based on the height of the surface can be fused for the final result.[17, 18]

One drawback of the cooperative approach in comparison to the competitive one is that it is based on a more complicated fusion model since it requires open measurement systems that gather distance and angular measurements by the system sensors. However, a cooperative strategy leads to better metrological performance, and it is required specifically in conditions where sensors are not able to capture independent localizations of the data points (Figure 6).

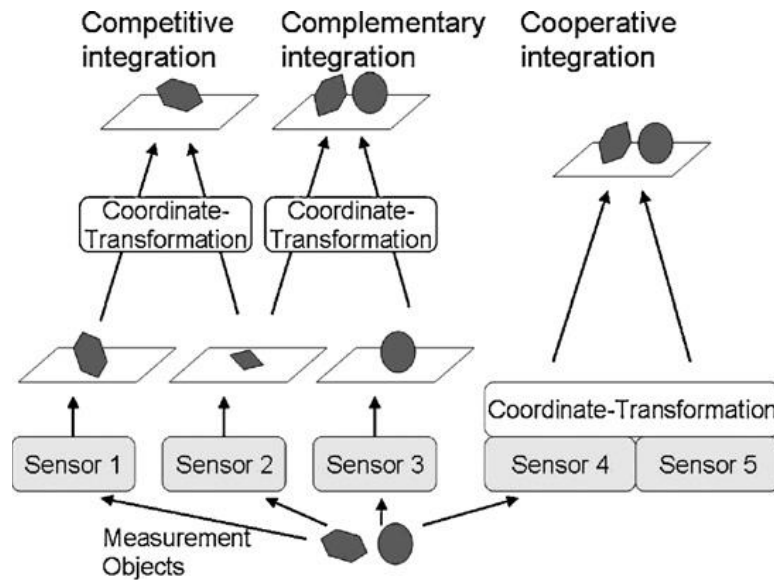


Figure 6. Methods for data acquisition [19]

According to an article published by Boudjemaa et al.,[4] data fusion problems can be classified based on the aspect of data fused to 1. Fusion across sensors 2. Fusion across attributes 3. Fusion across domains 4. Fusion across time.

In fusion across sensors, one property is measured using multiple sensors, for instance, optical and tactile sensors used to measure the dimension of an object collecting two or more data sets. On the other hand, fusion across attributes means that several sensors measure different quantities of an experimental situation.[20] A data fusion problem is called fusion across domains if one attribute is measured in different ranges and domains using several sensors. An example of this method could be when two images of an object are captured from different viewpoints using different illumination conditions. Next, these series of images are combined which leads to better representation of the image's characteristics.[21, 22] Lastly, in fusion across time, new measurement data is fused with historical data from an earlier calibration to determine



the system more accurately. An example of this data fusion problem could be determining filtering in dynamic measurements such as in Kalman filters.

## 2.2 Operations on multisensor data fusions

In data fusion, information is represented as raw data measured by a few sensors and their mathematical interpretation.[23] Next, signal level, feature level, and symbol level abstractions are differentiated. On signal level, data from different sensors are combined when the measurement data and their registrations are comparable. Feature level fusion can be implemented when temporal or spatial coherence between the sensor data on the signal level does not exist. On the symbol level, decisions are made based on the probability density function. In dimensional metrology, data fusion is mostly on the signal level although other abstractions might also be required in some instances.[24, 25]

Next, the registration operation transforms measurement data obtained in a sensor's coordinate system into one common coordinate system. Typically, the least square criterion is used to determine transformation parameters. Registration can be either based on surface descriptions or features. Feature-based methods can be used if measurement data contains easily detectable features.[21]

The registration process can be done in two steps: coarse and fine registration. Usually, in these cases, the datasets that will be fused later have different resolutions or are captured from different viewpoints or using different sensors.

There are different kinds of 3D registration methods for instance application of markers, using sensor positions to transform data into one coordinate system, and

numerical methods which can be further divided into coarse and fine registration processes.[26] In coarse registration, a feature-based strategy is used to register the first alignment of data. However, in fine registration, a similarity metric is determined which uses the entire data set.[27]

## 2.3 Sensor technologies for dimensional measurement

Tactile data acquisition, optical sensors, and computed tomography are different sensor technologies used in dimensional metrology as shown in Figure 7.

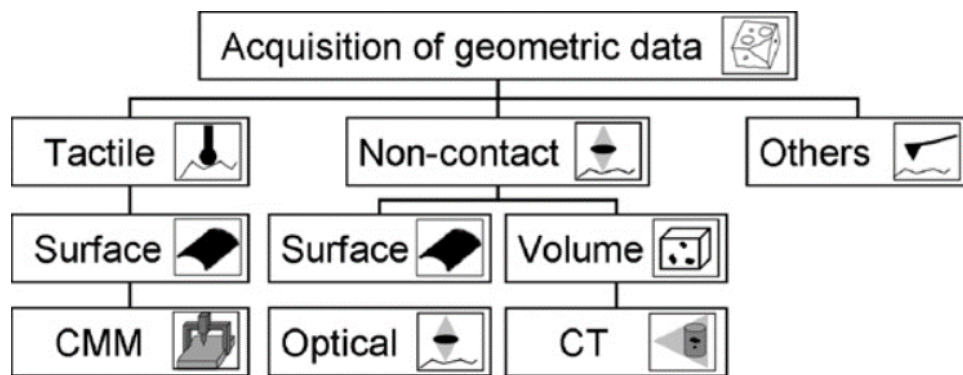


Figure 7. Different methods of data acquisition [1]

### 2.3.1 Optical sensors

Optical metrology enables fast measurement of high-density data points of flexible and soft surfaces through non-contact methods.[28] However, there are some drawbacks associated with optical sensors including occlusion, low accuracy, and sensitivity to surface conditions.[29] Data generated from optical sensors often includes redundant and missing data as well as some noises. Optical sensors can be categorized into 3 broad classes: point sensors, line sensors, and areal sensors for 1D, 2D, and 3D measurements, respectively.[30] Interaction between the sensor material

and surface as well as the geometry of the surface to be measured contribute to the accuracy of optical sensors.

### 2.3.2 Triangulation sensors

One important application of triangulation sensors is in measuring complex surfaces such as car bodies in automotive industries.[31] Measuring areas of these sensors range from mm to cm.[28] 3D sensors can be used in the case of complex surfaces with high point density.[32] To improve the resolution and accuracy even further (compared to 1D and 2D sensors), the phase shift algorithm can be applied to these 3D sensors.

### 2.3.3 Deflectometry

Specular properties of painted car bodies and optical devices require certain measurement techniques. Deflectometry can be used for three-dimensional measurement of specular surfaces. In this technique, stripe patterns are generated on a projection screen using a data projector. Reflection from the surfaces can then be captured using a digital camera and transferred to a computer for processing.[33]

### 2.3.4 Confocal microscopy

In confocal microscopy, only points that lie in the focal plane produce peaks, and lights emitted from areas above and below the focal plane are prevented in the optical path. This feature results in a high signal-to-noise ratio, high axial resolution, and increased contrast.

### 2.3.5 White light interferometry

A broadband light source with a small coherent length is used in this method to decrease interference range and measurement of rough surfaces. With these interferometers, a vertical resolution of 0.1nm for measurands of 200nm to a few mm can be achieved. The resolution of lateral measurement depends on the objective's numerical aperture.

### 2.3.6 Focus variation

First, the area of the workpiece is imaged onto a CCD camera using a microscope, and the image stack is recorded by changing the z-axis which is the distance between the objective and the workpiece. Next, the z-position with the highest contrast is determined for every pixel.

### 2.3.7 Image sensor

Image sensors are used in various applications including quality control and process monitoring. They are also applied in fields where repetitive inspections or automatic inspections are required.[34] The resolution of image sensors can be improved using subpixel techniques from sub-micrometer range to higher resolutions. Large data points can be captured at the same time without moving the optical head. However, there are geometric (e.g., field of view, depth of field, and visibility) and radiometric (e.g., dynamic range, illumination, and contrast) constraints associated with using high-density images.

### 2.3.8 Tactile sensors

Tactile sensors are often used in cases where the surface allows us to have lower point data density, for instance in prismatic workpieces or shapes without a large

variation. The measurements can be in one, two, or three dimensions ranging from a micrometer to several millimeters. Tactile systems are slower than optical systems, however, they have a higher accuracy. Tactile systems function through mechanical interaction with the workpiece and can be divided into two modes: discrete-point and scanning mode. In the discrete-point method the sensor is lifted-off between each two measurements and after touching the surface. On the other hand, in the scanning method, the tip ball is always in contact with the surface. Using the scanning method more points can be recorded in unit time as compared to the discrete method, however with higher uncertainty.

Additionally, in tactile sensors, if the tip balls contain more than one contact point, sharp edges, or peaks, a smoothed approximation of the surface might be obtained according to Figure 8.

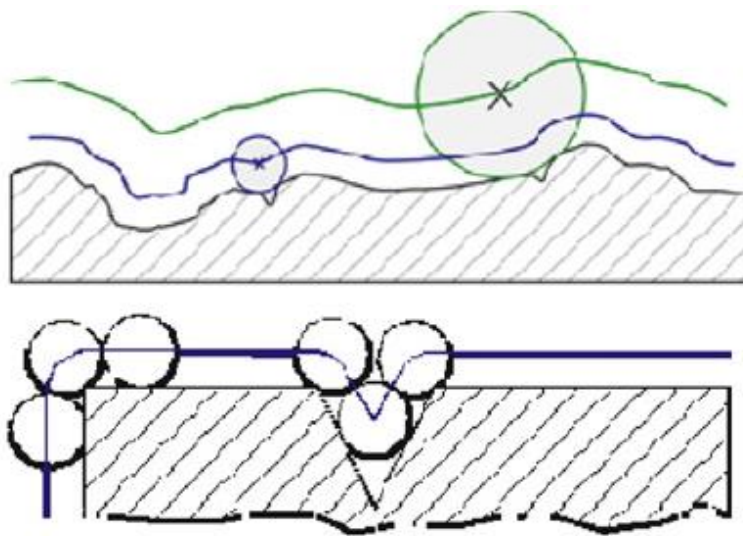


Figure 8. Influence of tactile probing system [35]

### 2.3.9 Computed tomography

In computed tomography systems, the workpiece is placed between an area detector and an X-ray tube. A rotary table is used to record X-ray projections from the workpiece in various orientations. Next, 3D volume data which consists of local material densities are calculated and this data is utilized to calculate the workpiece's surface.

Computed tomography systems generate precise information on the workpiece without destroying it in a time-efficient manner. Hence, they are used in testing and manufacturing workpieces such as gearboxes and injection nozzles.[28] There are different factors influencing the performance of computed tomography including the distance between the workpiece, detector, and the measurand as well as axial geometrical errors. Properties related to an object including its dimensions, geometry, and material composition can also impact the performance of these systems.[36]

### 2.3.10 Scanning probe microscopy

In scanning probe microscopy, a mechanical probe is used to generate magnified features that result in its atomic resolution. A small tip interacts with the surface and scans through the surface to measure points on the object. These interactions can be mechanical, optical, magnetic, thermal, and quantum electric. The advantages of using scanning electron microscopy are low force implementation on the surface, high resolution in sub-nanometer scale, and simultaneous measurement of materials properties and topography.[37]

In dimensional metrology, data fusions are used for atomic force microscopes (AFM) with three modes: contact, intermittent, and non-contact. For soft specimens, the

intermittent mode is generally used to avoid damage. In general, the intermittent and contact modes generate a higher resolution compared to the non-contact mode.

## 2.4 Data fusion in metrology

Applications of data fusion in metrology are vast in areas including robotics, non-destructive testing, pattern recognition medicine, geoscience, and finances.[38] Here we can see some examples of data fusion in dimensional metrology:

Image fusion: In image fusion, the images of the same scenes that are taken at different time points and from different angles with different sensors are fused.

Visual inspection: High-quality images that are obtained by image fusion using different sensors (multi-modal analysis) are required in the field of visual inspection. Limiting ourselves to only one camera does not result in an acceptable visual quality due to the interaction between the object, observation optics, and illumination. Additionally, limitation in 2D sensors' sensitivity contributes to the poor visual quality problem. To address this issue, multi-modal data analysis can be used enabling us to acquire the same scene using various sensors or different illumination parameters.

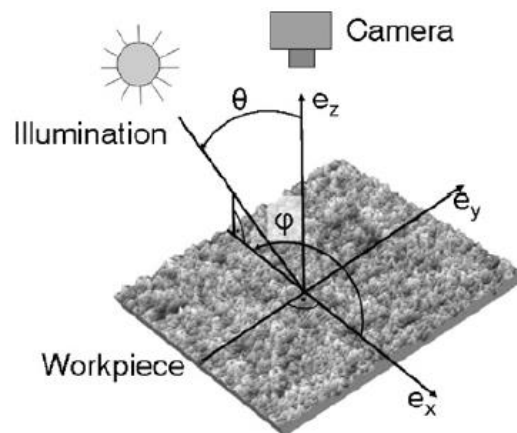


Figure 9. Different illumination parameters in image fusion [1]

We can apply fusion on the pixel level to enhance image quality. As shown in Figure 9, the illumination direction can be altered to obtain a series of images using homogenous sensors.[39] Next, the useful information (usually present in one or a few images) is selected for further transformation by coding the images to obtain the highest local contrast and finally fusing them.[24, 40]

#### 2.4.1 Computed Tomography (CT)

Fusing data obtained from X-ray CT with components of CMM improves the accuracy of CT such that it can be used in industrial coordinate metrology. Based on a study performed by Neuschaefer Rube et al., the combination of captured data by optical, tactile, and CT sensors is not required to be based on integrating the sensors into multi-sensor CMM.[41]

#### 2.4.2 Scanning probe microscopy:

Fusion of AFM data increases the accuracy of topography information.[42] The process includes 1. Deconvolution of tip geometry, 2. registration and data fusion. Multiresolution techniques such as wavelength transformation are used in registration methods.

### 2.5 Multisensor CMMs

Multisensor CMMs are incredibly high-precision sensors that have several advantages including 1. The first overview of the object is obtained by applying different sensors and this data guides more precise sensors.



2. Using inhomogeneous sensors generates data that cannot be created from single sensors, and this results in more information gaining from the object and eliminating ambiguities.

CMM 2.5D systems contain a measurement stage in XY positions with different 1D probing systems. These systems can be used for measuring large flat parts and parts with a broad range of height distributions. Different kinds of sensors can be installed on a fixed bridge.[1] The relative positions of these sensors can be calibrated. This enables us to switch between sensors while using a CMM machine. Additionally, using the same coordinate system allows coarse registration of data that are obtained with different sensors.

Using 3D measuring sensors, the measuring range can be extended by stitching. 3D systems are designed based on larger CMMs with some changes in their coordinate axes to reduce uncertainty and improve resolution. Maximum flexibility and testing of 3D geometries can be achieved using 3D positioning equipped with a probing 3D system. In these systems, measuring vision systems, different optical and tactile sensors are combined along with sensors based on computed tomography or special sensors such as fiber probes.[1] Because of commercial reasons, the method of combining captured data from different sensors is not published by the manufacturer and the of different measurement results' uncertainty is not considered. Based on the tracked sensors, there are other multisensory examples. Lasers are used to track reflectors or articulated scan arms, or other trackers such as CMM are utilized. Handheld scanners are one of the most recent developments in this field. Furthermore, structured light systems based

on photogrammetry are part of the available multisensor coordinate measuring instruments.[18]

### 2.5.1 Multi-source Remote Sensing Data Fusion

Remote sensing data fusion is one of the most prevalent techniques in data fusion that integrates data obtained with different spatial and spectral resolutions from sensors used in satellites, aircraft, and ground systems to produce results that are more accurate and detailed.

There are many challenges associated with fusing remotely sensed data because of requirements such as landscape complexity, temporal and spectral variations of the input data, and accurate data co-registration.

Remote sensing data fusion can be classified into three different levels: decision level, feature level, and pixel/data level.[43] In pixel-level data fusion, the raw data acquired using multiple sensors are combined into single-resolution data. Single-resolution data is more informative than the input data and illustrates changes between datasets acquired at different times.

In the feature selection method, features including edges, lines, corners, and texture parameters are extracted from different sources and next combined into a new feature map that can be used for further processing in place of the original data. Hence, this method is beneficial in cases where many available spectral bands make it too difficult to analyze each band separately.

Various methods can be used to extract these features depending on the characteristics of the source data specifically when the data is heterogeneous. For

instance, in image processing, this fusion requires pixel-level registration of the images. Hence, the feature maps obtained are used for pre-processing of image segmentation and change detection.

Lastly, in decision-level data fusion, results from multiple algorithms are combined to result in a final fused decision. Soft fusion is when the combined results are expressed as confidence instead of decisions. We can name a few methods for decision fusion including voting methods, statistical methods, and fuzzy logic-based methods.[44]

### 2.5.2 Structure in laser scanner point clouds

The first step to extracting information from point clouds is to recognize object surfaces. The success of this step determines applications including extraction of the bare Earth surface from airborne laser data, production of 3D city models, and reverse engineering of the industrial sites. Methods of extraction of the surfaces can be classified into two major categories: 1) segmentation of point clouds based on the proximity of points similarity of locally estimated surface normal, and 2) directly estimating surface parameters through clustering locating maxima in parameters. The second method is more flexible but can be used for shapes that can be described using only a few parameters.

### 2.5.3 Extraction of smooth surfaces

Grouping nearby points with the same property can lead to the extraction of smooth surfaces. Briefly, the point clouds can be segmented into different groups that represent the surface and hence it is a point cloud segmentation problem. This method is similar to image segmentation problems.

If the object under study is known to be polyhedral, then the segmentation algorithm determines the planar surface. This can be categorized as smooth surface extraction.[45]

## 2.6 Measurement uncertainty in performance verification

One of the first and most important publications in the area of measurement uncertainty is the “Guide to the Expression of Uncertainty in Measurement” or GUM.[46] GUM protocol is widely used as a national standard in different countries as well as National Metrology Institutes.[47] GUM is also being used in calibration and testing laboratories as a requirement of accreditation bodies.[48]

The first step to apply GUM to estimate measurement uncertainty is to define the measurand. Calibration of measuring instruments or calibration of important metrological characteristics is one type of measurement.[49] Based on the International Vocabulary of Metrology (IVM), in general, there are two types of measuring instruments: indicating measuring instruments such as micrometers, and material measures such as gage blocks.[50] There are three types of measurements in the calibration process: 1) assignment of values, 2) measurements used for adjustment, and 3) verifications to a defined tolerance.

There is a discussion going on that for CMM, performance verification is not a type of calibration.[51] In the calibration of materials, an assigned property is quantified. The assigned value can be an error or value measured under certain conditions. If these conditions are not in line with the definition of the measurand, additional uncertainty measurements should be considered.[52] On the other hand, performance

verification of an indicating measuring instrument does not result in an assigned quantity. In this case, the measured value is an error or set of errors observed under any set of conditions. These errors are errors of indication, and their associated specifications, tolerance, or limit value are called maximum permissible errors or MPE.

## 3 Methodology

The main goal of this research is to develop a model-based algorithm for data fusion and evaluate different approaches' accuracy. The most robust method will be chosen and applied to the real data acquired from the experiments. This study contains the 1D model, 2D model, experiment setup, and its analysis. In data fusion, we usually begin with two or more datasets from one object that need to be combined to enhance our interpretation of its measurand. The measurand in this study is the length of industrial parts if it is studied in 1D, the topographic surface map of a part in 2D, or the dimensions of a part in 3D space.

### 3.1 Experimental design and setup

As mentioned previously, the main intention of this study is to find the most efficient way to fuse datasets from different terminals to benefit from each data channel. In the case of the data channels in this research, one is a low-density dataset which is acquired by a more accurate tool (CMM). The other data channel is obtained using a relatively less accurate tool where its generated dataset has a higher density (laser scanner). Each one of these tools' specifications is explained further in the tool specification section.

To better delineate the problem, a few different situations are explained below:

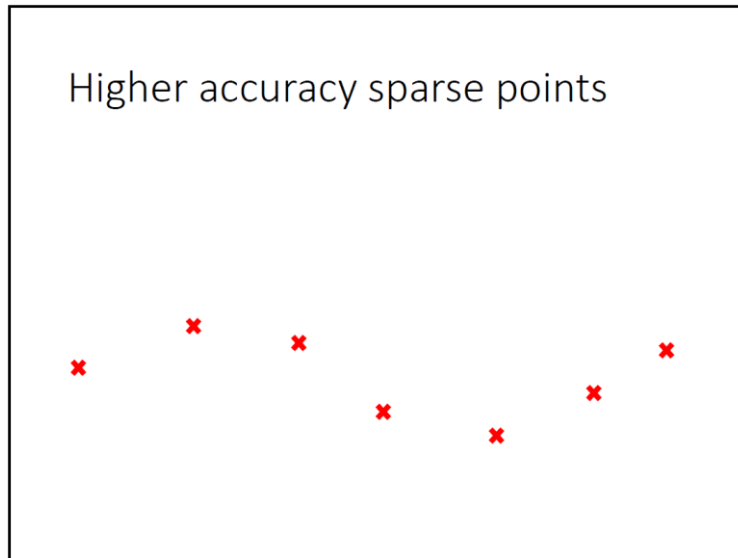


Figure 10. High accuracy dataset

The first dataset is from a high-accuracy tool which is relatively lower in density and slower in data acquisition as illustrated in Figure 10. To find the middle points between the acquired points in the higher-density dataset we can use different fitting methods as in Figure 11.

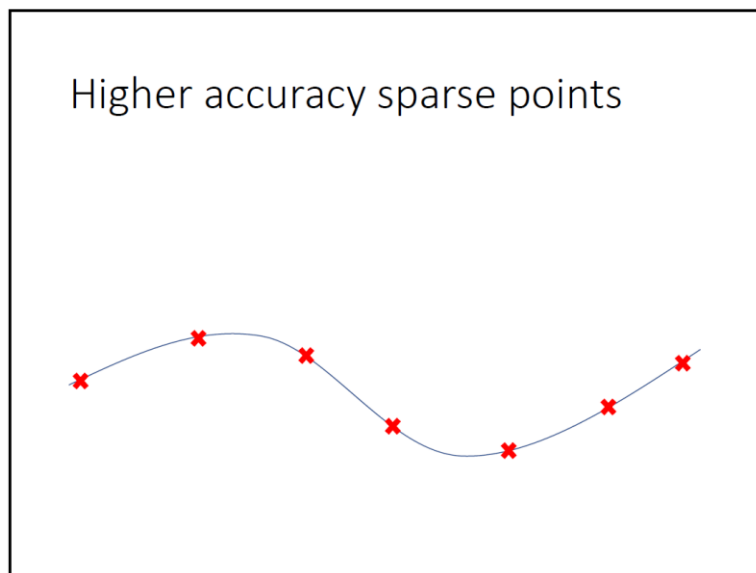
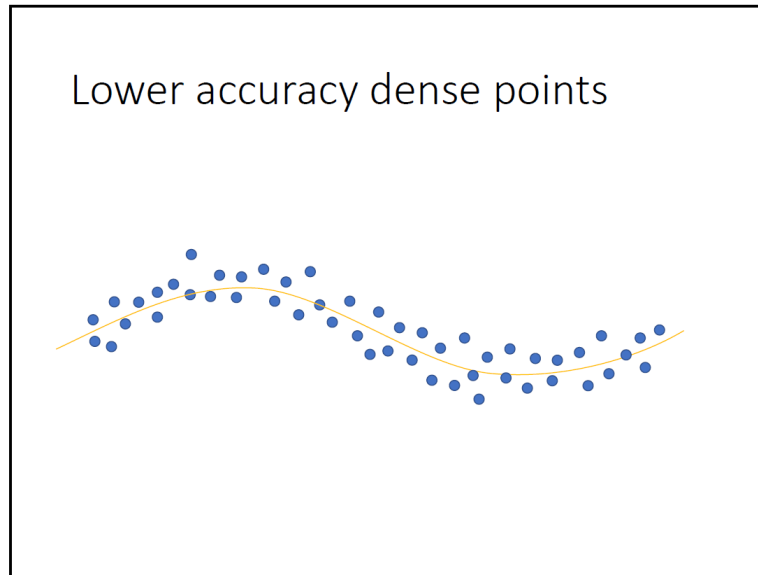


Figure 11. Fitted high-accuracy data points

On the other hand, the lower accuracy data points are taken by a tool that has a higher throughput and is usually faster in data acquisition as plotted in Figure 12. Then lower accuracy dataset can be fitted similarly with one of the fitting methods.



*Figure 12. Fitter lower accuracy dataset*

Another case for a lower accuracy dataset is when there is a defect and therefore the collected data shows a bump because of that. When this dataset is fitted, this defect will appear in the fitting curve. A sample dataset with its fitting is illustrated in Figure 13.



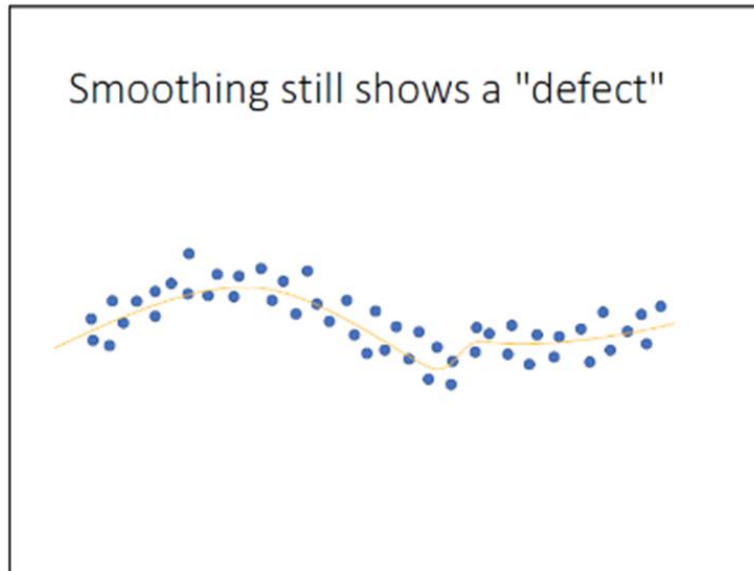


Figure 13. Fitted lower accuracy dataset with defect

The next question at this point is how to integrate these two datasets to avoid intervening with the noise while the high-accuracy dataset is efficiently correcting the lower-accuracy dataset in Figure 14.

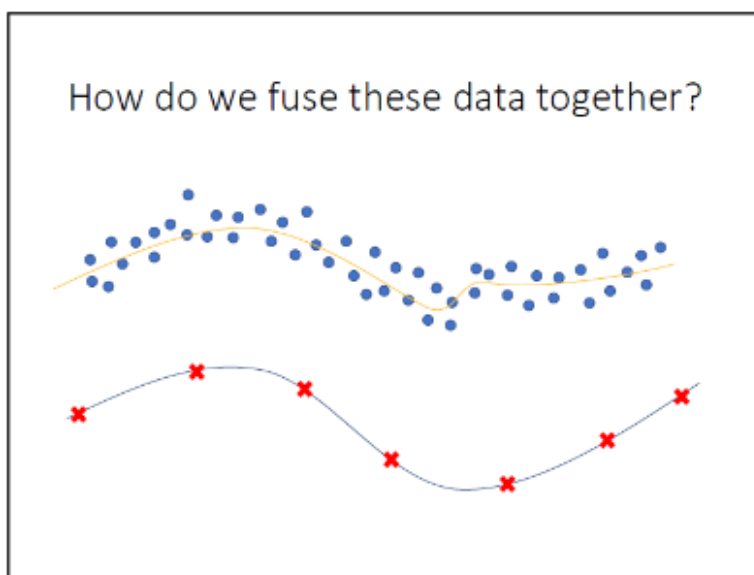
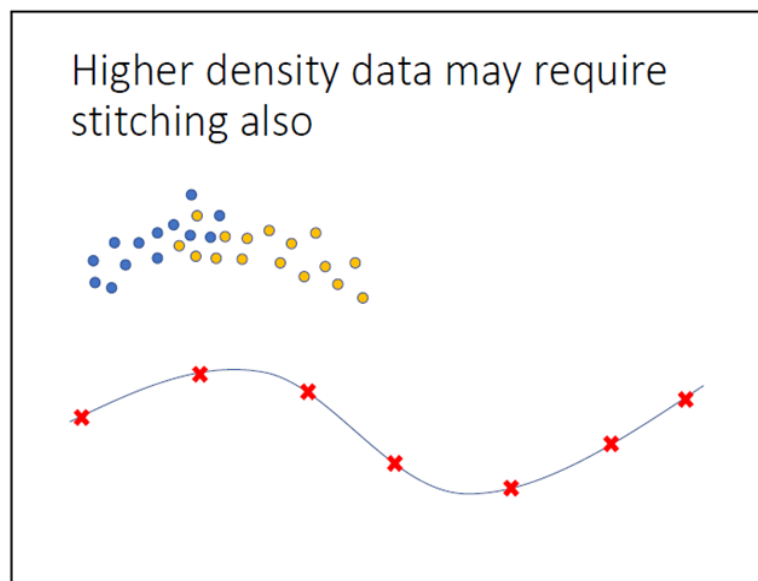


Figure 14. High and low accuracy datasets

There are a couple of different techniques which are required to combine two correlating datasets. The first technique is registration which is the transformation(s) of coordinate systems that bring single-view coordinates into a unified coordinate system. The other one is stitching in which we measure large and complex surfaces using a homogeneous sensor and this captured measurement can be stitched together as shown in Figure 15. To register the measurements, the relative sensor position compared to the measuring object is important.



*Figure 15. Two high-density datasets stitched together*

In the next step, the high-accuracy dataset can be compared with its corresponding points from the fitted lower-accuracy dataset. The difference between these points can be identified as the systematic error of the low-accuracy tool. This systematic error can be used to correct the low-accuracy dataset as illustrated in Figure 16.

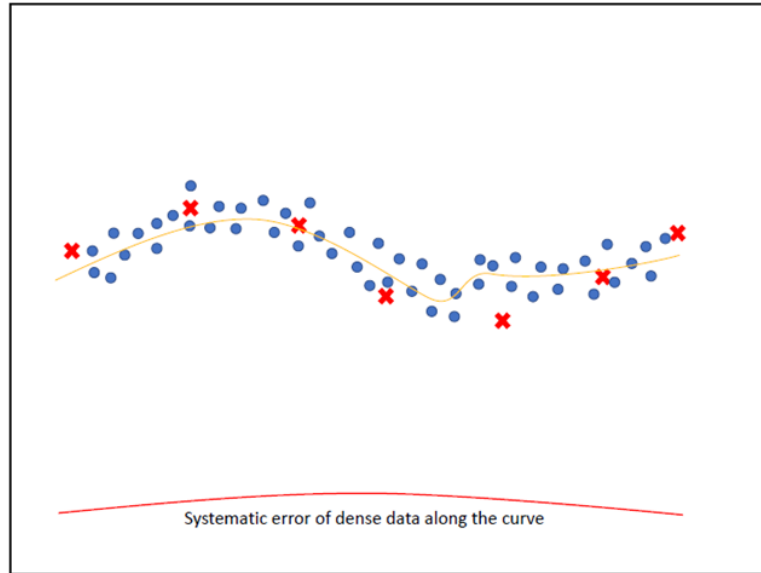


Figure 16. Low accuracy dataset systematic error

After correcting the low-accuracy dataset with the identified systematic error these two datasets should be fused to generate a final dataset that inherits the accuracy of the high-accuracy dataset and the density of the low-accuracy dataset. The fusion operation merges two or more sets of measured coordinates into a unified set of measured coordinates.

In the next section, different scenarios for data fusion will be elaborated.

### 3.2 1D model

In 1D measurement, we encounter the length of a part that has been collected with two instruments. These two instruments generate datasets that can be different in measurement resolution, measurement node density, and measurement throughput. In this model, we assume the first dataset specifies high accuracy and low-density points

compared to the second data grid which has less accuracy (noisy) but higher density. Here we test three different methods to fuse these two datasets in 1D dimension.

In all these approaches, the first dataset (high accuracy – low density) needs to be populated to obtain the same density as the second dataset (low accuracy – high density) to make the integration possible in a data processing step. On the other hand, the second dataset, which is noisy, needs to be smoothed to remove the noise.

### 3.2.1 Polynomial fitting and moving average

In the first approach, the low-density dataset is condensed by the polynomial interpolated fitting. Polynomial regression is a regression analysis where the relationship of dependent variable  $y$  and dependent variable  $x$  can be modeled using an  $n$ th-degree regression model. In other words, polynomial regression is a kind of linear regression in which the polynomial equation is fitted on the curvilinear data points between dependent and independent variables. Expansion of the baseline variables resulting from independent variables is known as higher-degree terms. These variables can be used in classification problems as well.[53]

In polynomial fitting, the least square method is used to minimize the variance of the residuals under the Gauss-Markov Theorem.[54] Residual is the difference between the measured value and the value estimated by the model. The least square is calculated by the formula below:

$$y = a_0 + a_1x + a_2x^2 + e$$

*Equation 1*

$$S_r = \sum_{i=1}^n (y - a_0 - a_1x - a_2x^2)^2$$

Equation 2

In formula (1), we have the equation for quadratic polynomial function where  $a_0$ ,  $a_1$ , and  $a_2$  are the model's coefficients and  $e$  is the error.

Formula (2) is the equation for the least square method where the error between the actual value and the value estimated by equation (1) is calculated. The error is next squared and summed through all the data points represented by  $n$ .

In this approach, we have used moving average functions to denoise the high-density dataset. It is a simplified form of a low-pass filter. The major difference between traditional low-pass filters and moving averages is that the low-pass filter can be used to focus on specific response frequency, however, the moving average filter is a more direct technique to smooth out a response. Moving average helps in reducing the noise while retaining important information about sharp step responses. Moving average is an optimal filter for reducing random white noise while retaining the sharpest step responses. The moving average filter works by averaging a specific number of points in the input data and generating responses for each of these data points. The equation of the moving average can be expressed as:

$$y[i] = \frac{1}{M} \sum_{j=0}^{M-1} x[i + j]$$

Equation 3

In equation 3,  $x$  represents the input data,  $y$  is the response, and  $M$  is the number of points to be averaged over, specified by the user. [55] The simple idea behind this equation is that the average of the last ' $M$ ' entries in the input data is calculated and utilized to generate the output.

The user has control over the window size of the moving average. However, it is critical to choose the right window size. If the window size is too small, then data will remain noisy and if it is too large, the response is over-corrected, and we may lose critical information. Hence, choosing the correct window size can be achieved through trial and error.[56-58]

Eventually, for the first approach, the difference between the moving average and the high-density raw dataset is calculated. Next, the difference between the 15-point moving average and the high-density raw dataset is added to the low-density polynomial fitted curve. This will generate a curve that inherits the surface behavior of the high-density dataset and the local features of the low-density dataset.

In the MATLAB code, the flow starts with loading the raw dataset for the high-accuracy and low-accuracy datasets and naming them as new arrays. Next, to use the moving average on all the data points, note that the first 15 and last 15 data points could not completely be fitted in the moving average window size. Therefore, the first 15 data points are flipped and added to the beginning of the data series. The same procedure is applied for the last 15 data points to be compatible with moving average calculations. Lastly, the difference between the moving average and the original output is computed and used to calculate the standard deviation and the range.

### 3.2.2 Spline fitting and moving averages

In the second approach, the high-accuracy sparse dataset is fitted by the cubic smoothing spline function. A spline of order  $K$  is a piecewise polynomial function with degree  $K$  which continues and has continuous derivatives of orders  $1, \dots, K-1$ .

If  $K$  is 3, it is called a cubic spline, a continuous function with continuous first and second derivatives. The continuity in the lower-order derivatives results in a very smooth spline.[59-61]

The cubic spline function formula is as follows:

$$\underbrace{p \sum_{j=1}^n w_j |y_j - f(x_j)|^2}_{\text{error measure}} + (1 - p) \underbrace{\int \lambda(t) |D^2 f(t)|^2 dt}_{\text{roughness measure}}$$

Equation 4

In equation 4,  $n$  is the total number of inputs,  $y_j$  and  $x_j$  are the  $j^{\text{th}}$  input of  $y$  and  $x$  respectively.  $D^2 f$  refers to the second derivative of “ $f$ ”.  $w$  is the error measure weight with the default value of 1.  $\lambda$  is the piecewise constant function in the roughness measure with the default value of 1. In general, the cubic spline function chooses a value for smoothing parameter  $p$  based on the given input  $x$ .

Next, two moving averages with 15 and 45-point window sizes are applied to the less accurate dense dataset. Then the difference between these two moving averages on each point is calculated and added to the high-accuracy spline fitted curve. It needs to be noted that the difference between the 15 and 45 moving averages is denoising the

low accuracy dense dataset. Similar to the first approach, both moving averages are applied to the elongated low-accuracy, dense dataset by flipping the first and last variables of the original X and Y values.

### 3.2.3 Spline fitting and Gaussian filtering

In the third approach, the high-accuracy sparse dataset is fitted to a curve by the cubic smoothing spline as explained in the previous section. On the other hand, the low-accuracy dense dataset is fitted by the Gaussian filter.

The Gaussian filter is a filter with its impulse response being independent of the Gaussian function. It has the properties of having no overshoot to step function input and optimizing the rise and fall time. Gaussian filters work by suppressing high frequencies and minimizing the spatial spread. Mathematically speaking a Gaussian filter changes the input signal by convolution with a Gaussian function known as Weierstrass transform.

The impulse response and frequency response of the one-dimensional Gaussian filter is as follows:

$$g(x) = \frac{1}{\sqrt{2\pi}\sigma} e^{-x^2/(2\sigma^2)}$$

*Equation 5*

$$\hat{g}(f) = e^{-f^2/(2\sigma_f^2)}$$

*Equation 6*



In equations 5 and 6, the impulse response and frequency response given by the Fourier transform, are expressed with standard deviation as parameters.  $X$  is the distance from the origin in the horizontal axis, and  $\sigma$  is the standard deviation of the Gaussian distribution.

By choosing Gaussian filtering, we are assuming that errors and uncertainties in data and models follow a normal distribution with a mean of zero. [62-64]

In the MATLAB code, the “gausswin” function specifies the length of the Gaussian window. Then the convolution of the low-accuracy dense points and the Gaussian window is calculated. Lastly, the difference between the convolution results and low accuracy dense points is added to the cubic spline fitted curve on the high accuracy sparse dataset to fuse the two data series.

The “conv” function returns the convolution of two vectors “u” and “v” as specified by shape. In this research, we have used the “same” shape that returns only the central part of the convolution the same size as u.

$$w(k) = \sum_j u(j)v(k - j + 1)$$

*Equation 7*

Equation 7 represents the convolution of two vectors u and v which is the overlap area under the point as v slides across u. It is the same function as multiplying polynomials with elements of coefficients the same as u and v. [65-68]

Criteria that need consideration in these approaches are the balance of the interpolation between the low-density points and the smoothing of the high-density points which depends on the instruments being utilized.

If the high-density instrument is susceptible to more noise, using more filters can be effective in making this dataset closer to the low-density references. However, it should be considered that using too many intensive filters can remove some of the small-scale information that existed in the raw data that might affect the overall shape of the part. In this regard, we can introduce two types of filters based on Figure 17. One is the low-pass, and the other is the high-pass filter. Combining these two creates a filter that is called a bandpass filter. The low pass filter relays the frequencies below a certain level and the high pass filter does the opposite. The bandpass filter relays the frequencies in between two ranges.[69]

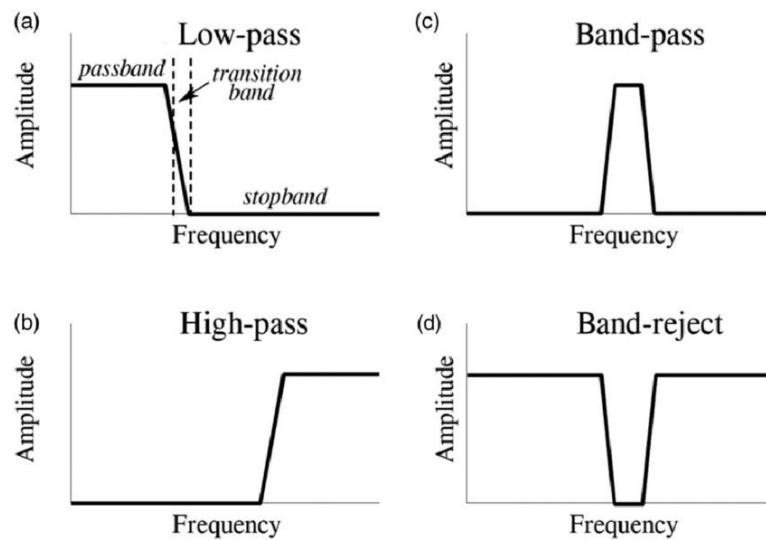


Figure 17. Low pass, High pass, and Bandpass filters [69]

### 3.3 2D model

In the 2D model, we have a surface topography of a part where the height values are the main measurand across the length and width of the part. So, the instruments collect these three numbers as raw data. Different devices could be utilized which may have different measurement resolution, measurement node density, and measurement throughput. They could be tactile sensors such as CMM, profilometer, or AFM or optical instruments such as laser tracker, laser scanner, or scanning electron microscope. In all these instruments one of the main goals is to measure the surface topography of the workpiece.

#### 3.3.1 Building surface point grids

In this model we initially created two datasets, the first one is more accurate but sparse and the second one is less accurate but denser. Then we tried to find the best approach to integrate these two datasets and compare different enhanced accuracy results.

First, we create simulated datasets for the low-density and high-density grids in MATLAB. The “meshgrid” command does this by taking the first point and last point and then by defining the step size between these two ranges, it creates the grid. For both datasets, the X and Y ranges are between 0 and 100 mm. The step sizes for the low-density and high-density datasets are 10 mm and 0.5 mm respectively.

```
[X1,Y1] = meshgrid(0:10:100);
```

For the Z surface values we used a sinusoidal function to form a wavy plane as follows:

```
Z1 = 0.5*sin((X1+Y1)/(100/pi));
```

Then by adding some local defects, this surface has become similar to a real part with defects on its surface. These defects are a combination of multiple equations and summing them up to shape the surface of the low-density dataset. The defects that are used are as follows:

A double-sided surface defect by using an exponential function:

```
def_L1 = (X1-50).*exp(-(X1-50).^2 - (Y1-50).^2);
```

A Boolean defect:

```
def_L2 = (sqrt((X1-40).^2 + (Y1-40).^2)<5) .* (X1 > Y1) .* (X1-Y1)/18;
```

Two exponential functions:

```
def_L3 = (1/sqrt(2*pi)).*exp(-((X1-70).^2/2)-((Y1-70).^2/2));
```

```
def_L4 = (-1/sqrt(2*pi)).*exp(-((X1-30).^2/2)-((Y1-80).^2/2));
```

A sphere function:

```
def_L5 = 0.4-((X1-80).^2)-((Y1-30).^2);
```

Another Boolean function

```
def_L5(def_L5<0)=0;
```

Another double-sided surface defect:

```
def_L6 = (1/sqrt(2*pi)).*exp(-((X1-80).^2/2)-((Y1-50).^2/2));
```

Lastly, by summing up these defects with the Z wavy plane, this dataset represents the low-density, high-accuracy surface with all its defects as shown in Figure 18.

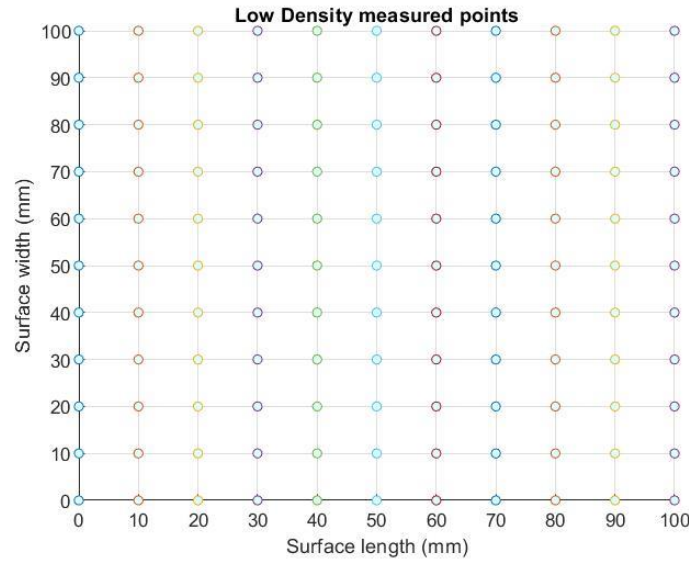


Figure 18. Low-density measured points

On the other hand, the high-density dataset uses the “meshgrid” with a step size of 0.5 mm as follows:

```
[X2,Y2] = meshgrid(0:0.5:100);
```

All the same local defects from the low-density dataset are also added here to the high-density dataset to create its surface as follows:

```
def_H1 = (X2-50).*exp(-(X2-50).^2 - (Y2-50).^2);
def_H2 = (sqrt((X2-40).^2 + (Y2-40).^2)<5) .* (X2 > Y2) .* (X2-Y2)/18;
def_H3 = (1/sqrt(2*pi).*exp(-((X2-70).^2/2)-((Y2-70).^2/2)));
def_H4 = (-1/sqrt(2*pi).*exp(-((X2-30).^2/2)-((Y2-80).^2/2)));
def_H5 = 0.4-((X2-80).^2)-((Y2-30).^2);
def_H5(def_H5<0)=0;
def_H6 = (1/sqrt(2*pi).*exp(-((X2-80).^2/2)-((Y2-50).^2/2)));
```

```
all_def_H = def_H1+def_H2+def_H3+def_H4+def_H5+def_H6;
```

After building the high-density dataset with the local defects, adding global noise and form to this dataset could make it less accurate compared to the low-density dataset. The noise that has been added to this dataset is a normally distributed random value as follows:

```
noise = 0.05*(1/sqrt(12))*(randn(201));
```

Two types of forms are also added to apply global deviation as follows:

```
form1 = 0.1*cos((X2+Y2)/(100/pi));
```

```
form2 = 0.0001*(X2.^2 - Y2.^2);
```

In the end, by combining all these local defects and global noise and forms the high-density, low-accuracy dataset is generated as shown in Figures 19 and 20.

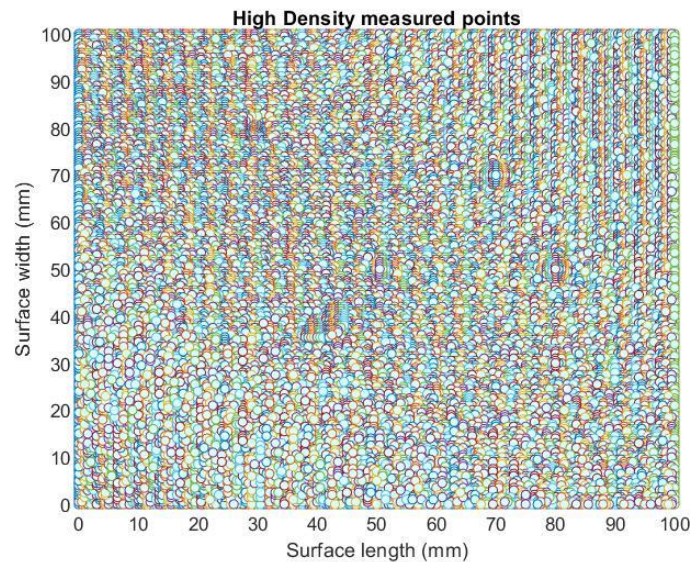


Figure 19. High-density measured points

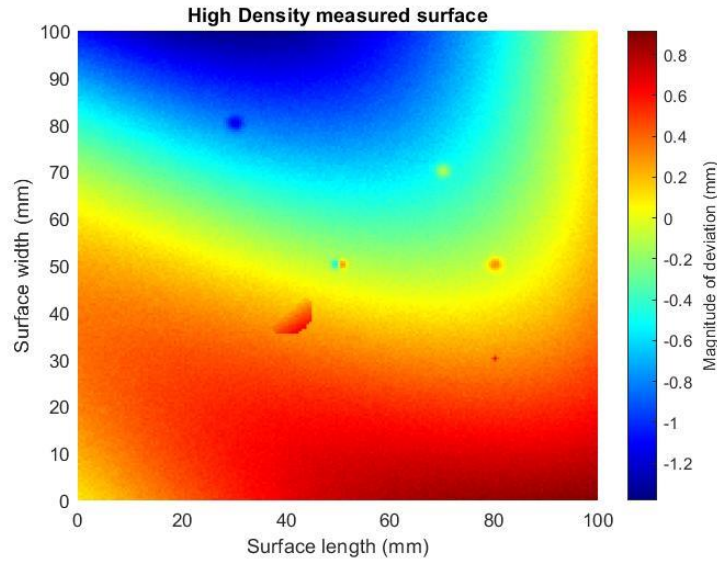


Figure 20. High-density measured surface

### 3.3.2 Fusion process

To fuse the two produced datasets and generate a high-density and high-accuracy dataset as a result, the following steps from the 1D model have been selected to be applied:

1. Since the high-density dataset is noisy, it needs to be smoothed out through a filter. Different filtering methods were tested for 2D interpolation with various methods including “Cubic”, “Spline” and “Akima” and the “Gaussian” filter. Among all, the Gaussian filter had the best performance to make the smoothed surface closest to the real part. To make this judgment, the smoothed surface with each one of these filtering methods was compared with the real surface (noise and form-free high-density surface), the Z value difference from the two datasets was compared, and the mean and standard deviation were computed to find the best method.

To smooth out the high-density dataset with the Gaussian filter (`imgaussfilt`), a positive number as this filter's quotient was defined to pick the number of the standard deviation which is desired to distribute this filtering method over.

This concept could apply a pass-filtering method to the dataset. Two separate sigma values, to define the Gaussian filter distribution range could perform a bandpass filtering in this case. Therefore, for the first Gaussian filter we use  $\sigma = 0.3$  and for the second filter, we use  $\sigma = 10$ . These two sets of numbers have been tested based on our dataset and the noise type applied to them (`randn`). For future datasets, these two variables should be adjusted accordingly.

In this bandpass filter that is used here, the smaller value sigma (coarse or low pass filter) removes the surface noise, and the larger sigma value (fine or high pass filter) removes the surface defects. The residual surface feature of the coarse filter (low-pass) is the low-frequency defects over the surface and the remainder of the fine filter (high-pass) is the noise over the surface shape. Hence, the difference between these two filters is only the surface defects.

With this method, the defects are separated from the high-density dataset for the following steps:

```
Z2_gaus_coarse = imgaussfilt(Z2_final,0.3);
Z2_gaus_fine = imgaussfilt(Z2_final,10);
Z2_gaus_diff = Z2_final - Z2_gaus_coarse - Z2_gaus_fine;
```



2. The second step to integrate these two datasets is to interpolate the low-density dataset. This step is necessary to equalize the grid size for both datasets. Initially, the low-density dataset was 11x11 points and the high-density dataset was 201x201 points. Therefore, the low-density dataset needs to be converted to a 201x201 point grid. This condensation is possible by data interpolation. Before interpolating the low-density dataset, it is important to consider the exceptional situation. One of these exceptions is when the low-density has measured a point which was a bump or a valley defect on the surface. In that case, interpolating the low-density dataset including these local surface defects, and adding it to the high-density defect dataset will result in a double defective surface which is undesirable.

Therefore, this interpolation must be applied to the low-density dataset with any possible defects removed from it.

To remove the potential defective points from the low-density dataset, we create a for loop in the script to take the Z value of the Gaussian-filtered defect points which have the same X and Y coordinates as the low-density dataset. In this for loop, we first create an array of all zeros with the same size as the low-density dataset. In this case, it will be 11x11. Then for every point in the low-density dataset, we collect the Z value of the corresponding X and Y coordinates from the Gaussian-filtered defect dataset. These Z values will be subtracted from their low-density dataset counterparts. These steps in MATLAB are as follows:

```
Z2_adj = zeros(size(X1,1),size(Y1,2));
```

```

for i=1:size(X2,1)
    for j=1:size(Y2,2)
        a=(X2(i,j)==X1 & Y2(i,j)==Y1);
        [row,col]=find(a==1);
        Z2_adj(row,col) = Z2_gaus_diff(i,j);
    end
end

Z1_adj = Z1_final - Z2_adj;

```

3. Now that the defect-free low-density dataset is prepared, it is time to interpolate this dataset to equalize its size with the high-density dataset.

There are different methods to interpolate including:

- Linear: Interpolation of the values at neighboring grid points
- Nearest: Interpolation at the query point nearest to the sample grid point
- Cubic: Interpolation at a query point is based on a cubic convolution interpolation of the values at neighboring grid points.
- Akima: This interpolation is based on the piecewise function of polynomials evaluated using the values of neighboring grid points.
- Spline: This method is based on cubic interpolation of the values at neighboring grid points using not-a-knot end conditions.

The interpolation step is implemented in MATLAB by the following script:

```
Z1_dense = interp2(X1,Y1,Z1,X2,Y2,'cubic');
```

After interpolating the defectless low-density dataset and obtaining a high-density data grid, it will be added to the defect dataset which was extracted by the Gaussian filtering from the high-density dataset. This is the final product of the fusion process.

$$Z1_{\text{gaus\_defect}} = Z1_{\text{dense}} + \text{gaus\_diff};$$

This result can be compared with the actual surface dataset (without noise) which was generated in the beginning to evaluate the accuracy of the fusion strategy. The final result's accuracy would be dependent upon different methods that can be used for interpolation or filtering steps. To analyze the fusion accuracy, generated results by each of the interpolation methods are compared with the actual surface to evaluate the deviation by each method.

$$\text{fusion\_deviation} = \text{actual\_surface} - Z1_{\text{generated}};$$

## 3.4 2D experiment

### 3.4.1 Instruments and workpiece specs

In the last section, we developed the 2D model for fusing datasets from 2 channels. In this section, we aim to generate the raw dataset from two devices that are generating point clouds located in the metrology labs at UNCC:

- 1- CMM: low-density, higher-accuracy dataset
- 2- Laser scanner: high-density, low-accuracy dataset

The CMM machine (Figure 21) brand and model are Leitz PMM-F 30.20.16 located at Siemens lab in EPIC building. This machine has a resolution of  $0.02\text{ }\mu\text{m}$ , repeatability of  $1.4\text{ }\mu\text{m}$ , a maximum throughput of 35 probes per minute, and a measuring range of  $3000 \times 2000 \times 1600\text{ mm}$  along the X, Y, and Z axes respectively.



Figure 21. CMM: Leitz PMM-F 30.20.16

The articulate arm laser scanner (Figure 22) brand and model is Romer Absolute Arm – 7525 SEI located at Precision Lab in the Duke building. This machine has a resolution of 500 nm with an arm measuring range of 2.5 m.



*Figure 22. Laser Scanner: Romer Absolute Arm – 7525 SEI*

The workpiece that is used for this experiment is a rotational sine surface part made of Aluminum using a CNC machine as illustrated in Figure 23.

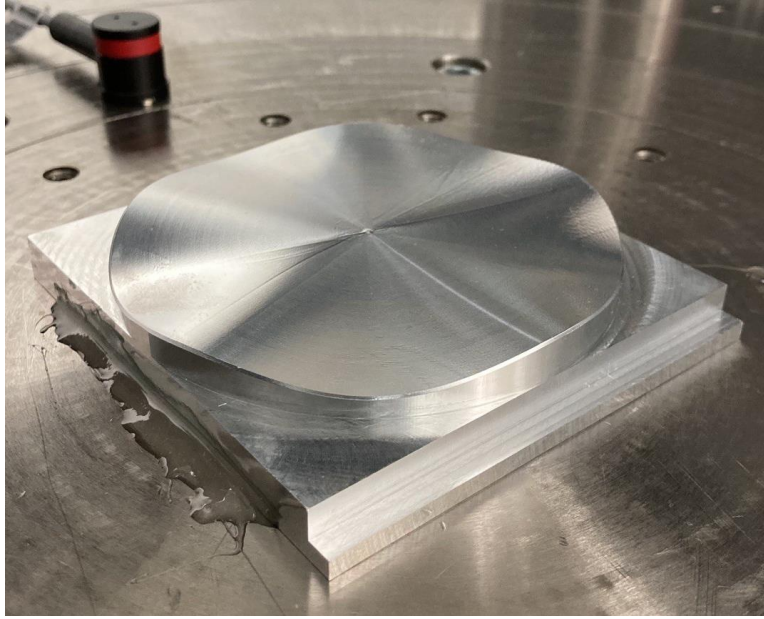


Figure 23. Aluminum workpiece used for the 2D experiment with a local thermometer on the rotary table

This part surface has the nominal surface function of:

$$z(r, \theta) = \frac{r^3}{75000} [\cos(\theta) - \sin(5\theta)]$$

Equation 8. Workpiece surface nominal function

In equation 8,  $z$  and  $r$  have units of mm. The part has a radius of 50 mm, with a range for  $z$  of  $\pm 3.06$  mm.

To measure the part with the CMM tool, it is attached to the CMM rotary table with Epoxy glue. It is important to avoid clamping the part to the table to prevent any surface form imposed on the part by the clamping force. The CMM lab is always kept at 20 °C and two thermometers monitor the instant temperature and control it by the HVAC system dedicated to the room. One of these thermometers is on the tool wall as shown

in Figure 24 and the other one is placed on the rotary table close to the workpiece. The workpiece is placed on the table for a whole day before starting to measure. This will allow the part to be in equilibrium with room temperature.



*Figure 24. CMM ambient thermometer*

To measure the workpiece with the articulate arm laser scanner, it is placed on the workbench for 24 hours before obtaining the measurements. Since the laser scanner is not in physical contact with the part, it is not necessary to attach it to the bench using any adhesive component such as epoxy glue that was used for CMM. (Figure 25)

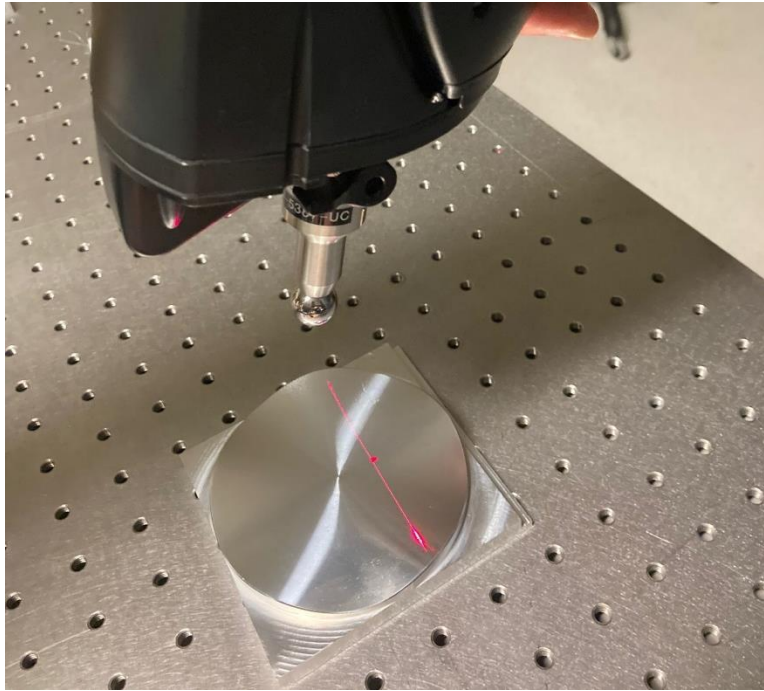


*Figure 25. Workpiece measured by articulate arm laser scanner*

### 3.4.2 CMM measuring strategy

In this section, we first focus on the CMM measurement method and then will explain the laser scanner measurement procedure.

The CMM uses the QUINDOS language to script and uses the glossary of commands to perform predefined functions. To start any measurement the type of stylus that is going to make the measurement should be selected. The stylus shape, length, and tip radius are important values to take into the software parameters. The stylus tip is made of two main materials. The first is ruby and the other is silicon nitride ( $\text{Si}_3\text{N}_4$ ). Ruby is generally used for steel workpieces and silicon nitride is suitable for aluminum parts. If a ruby stylus is used for the aluminum part, its surface may scratch a tiny amount of the workpiece which would accumulate on the sphere surface and result



in measurement error. Hence, silicon nitride which has a lower coefficient of friction and higher hardness than ruby is well suited for our application.

After adhering the part to the rotary table and choosing the proper stylus for measurement, the CMM should be homed to zero any potential offset or drift from the tool. This would be performed by the “AUTZER” command in QUINDOS which would take the column bridge to (0,0,0) position and rotate the rotary table to the 0 ° angle. Then by putting “NOINCH” the metric units could be selected to use for the data acquisition. To enable or disable the rotary table rotation the “ENBRTMOV” and “DSBRTMOV” could be used respectively. If the table is rotating, the operator can enable or disable the coordinate system rotation along with the table by “ENBRTCSY” and “DSBRTCSY” commands. The tool has a safety feature to control the rotary table rotation and column travel speed lock that can be temporarily disabled by the “CRECMPAR” command.

After setting up the preliminary settings, the bridge column can be moved to pick up the selected stylus to get qualified. Therefore, the reference coordinate system (“REFR\$CSY”) which is the tool’s native coordinate system should be selected by the “USECSY” command. (Figure 26)

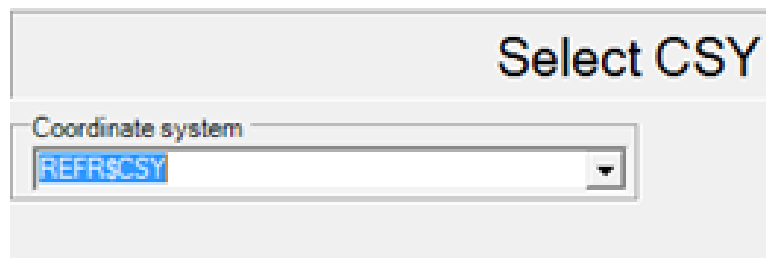
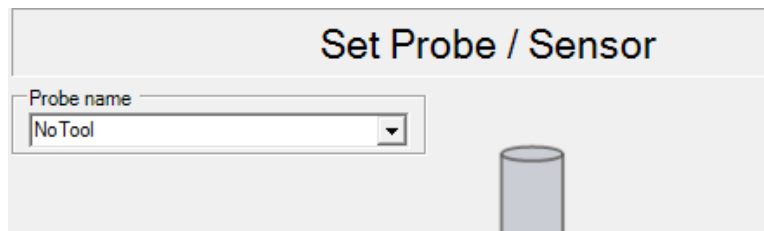


Figure 26. USECSY command: select a defined coordinate system for the tool

Next, the active probe which is mounted to the stylus holder should be selected by the “SetActiveTool” command. In this case, the “NoTool” should be selected to secure the tool to mount a new stylus. (Figure 27)



*Figure 27. Set the active probe on the tool*

Then, the stylus that the operator intends to mount to the holder should be selected by the “USEPRB” command. The stylus rack has 3 spots to store the stylus for regular use. The operator is responsible for ensuring the right placement of the stylus on the rack. By running the “USEPRB” command the column bridge starts moving toward to selected rack number to mount the stylus in its holder. (Figure 28-29)

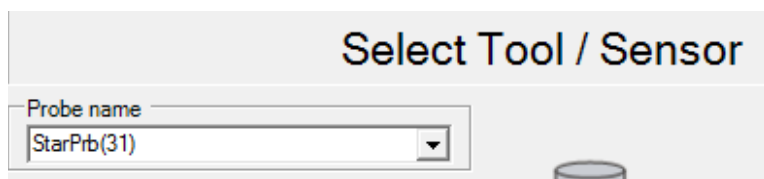


*Figure 28. Selecting the prob to be mounted on the holder*

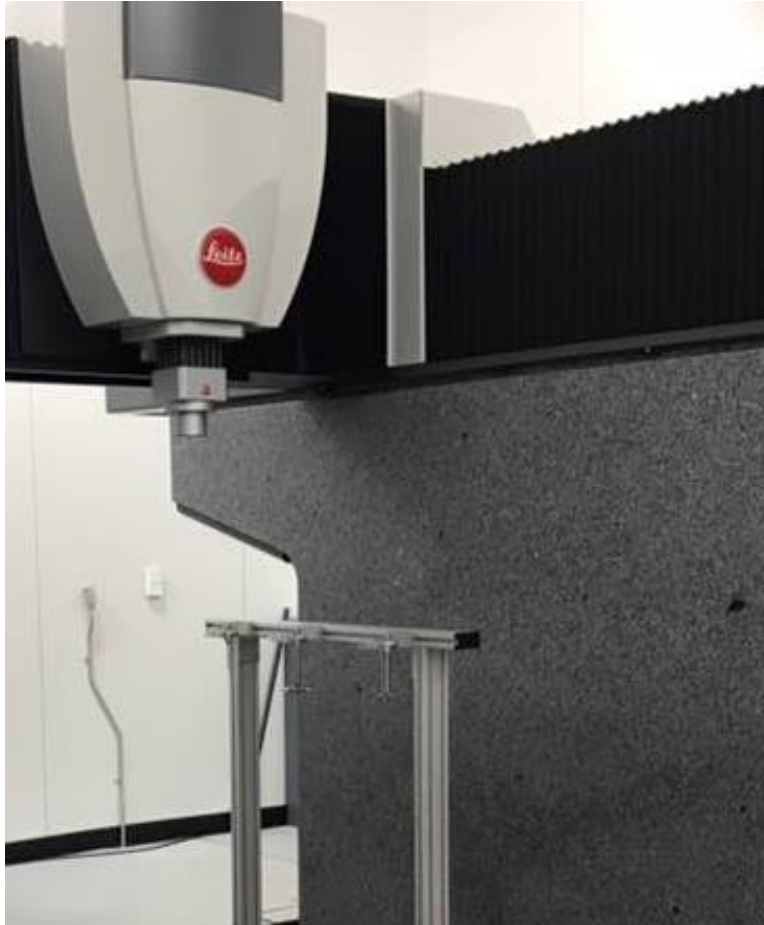


*Figure 29. CMM ram taking stylus from the rack*

After mounting the stylus in the holder, it should be qualified for its dimensions and angles. This is performed by using an artifact as the reference to evaluate the stylus. This artifact is a round ceramic spherical ball with 29.9496 mm in diameter and 90° orthogonal to the XY plane. First, these specifications are defined as the artifact dimensions by using the “DfnArtefact” command. (Figure 30)

### Define Qualification Artefact

Name of qualification artefact <input style="width: 90%;" type="text" value="ATFD30PZ"/>	Sphere diameter <input style="width: 90%;" type="text" value="29.9496"/>
	Azimuth (angle: +X -> +Y) <input style="width: 90%;" type="text" value="0.0"/>
	Elevation (angle: XY -> +Z) <input style="width: 90%;" type="text" value="90.0"/>
	Shaft diameter at sphere <input style="width: 90%;" type="text" value="8.0"/>
	Artefact on rotary table <input type="checkbox"/>  <b>Attention !</b>  Is supported from firmware 7.18 (B4) resp. 8.18 (B5)

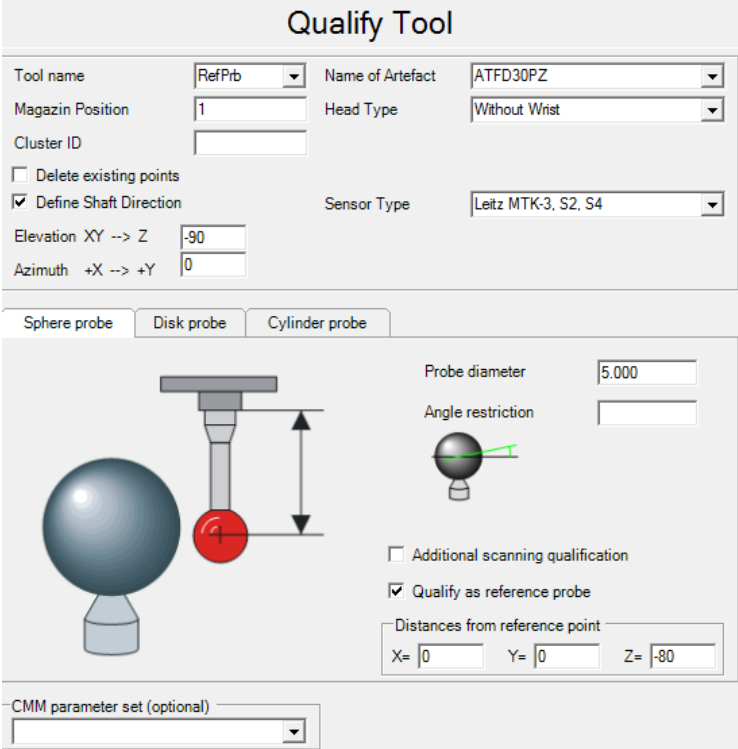
Figure 30. Defining artifact by the "DfnArtefact"

The specified values for the artifact dimensions are retrieved from the manufacturer spec. (Figure 31)

KALIBRIERZERTIFIKAT / CALIBRATION CERTIFICATE			
Gegenstand Object	Kalibrierkugel Calibration ball	Auftrags-Nr., Datum Order No., date	1063624
Material Material	Al2O3 Keramik	Serien-Nr. Serial No.	N6486
Durchmesser (mm) Diameter	29.94960	Rundheit (µm) Roundness	0.062
Messunsicherheit Ø (µm) Uncertainty of measurement	0.3	Messunsicherheit Ø (µm) Uncertainty of measurement	0.04
Datum Date	24.10.2013	Für die Messung For the Measurement	H.Mathys

Figure 31. Artifact specs

In the next step, to qualify the mounted stylus, using the “QualifyTool” command, will open the settings to enter the probe type, orientation, and dimensions by the operator. (Figure 32)



The 'Qualify Tool' dialog box contains the following settings:

- Tool name:** RefPtb
- Name of Artefact:** ATFD30PZ
- Magazin Position:** 1
- Head Type:** Without Wrist
- Cluster ID:** (empty)
- ☐ Delete existing points
- ☒ Define Shaft Direction
- Sensor Type:** Leitz MTK-3, S2, S4
- Elevation XY --> Z:** -90
- Azimuth +X --> +Y:** 0

Below these settings are three tabs: 'Sphere probe', 'Disk probe', and 'Cylinder probe'. The 'Sphere probe' tab is selected, showing a diagram of a sphere and a probe. To the right of the diagram are the following settings:

- Probe diameter:** 5.000
- Angle restriction:** (empty)
- ☐ Additional scanning qualification
- ☒ Qualify as reference probe
- Distances from reference point:**
  - X=** 0
  - Y=** 0
  - Z=** -80

At the bottom, there is a dropdown menu for 'CMM parameter set (optional)'.

Figure 32. "QualifyTool" command settings

By running this command, the tool starts the probe qualification procedure in reference to the artifact by asking the operator to touch the north pole of the spherical artifact to locate the first searching point. (Figure 33)



Figure 33. Artifact north pole touch from Quindos software

During this process, the tool will take up to 96 measure points from the artifact to precisely calculate the stylus tip dimensions.

Once the stylus is quailed by the artifact, the rotary table coordinate system can be calibrated as well. This process will be performed by putting in at least 3 different table angles to perform short artifact qualifications to calibrate any potential table tilt or angle deviations. (Figure 34)

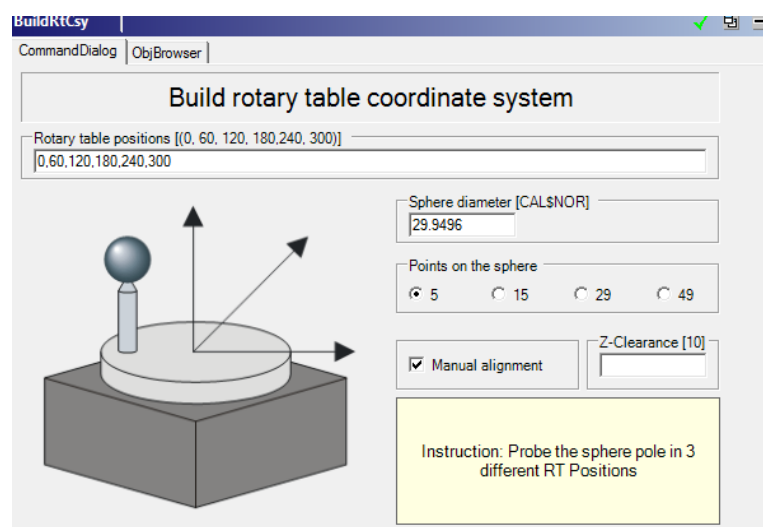
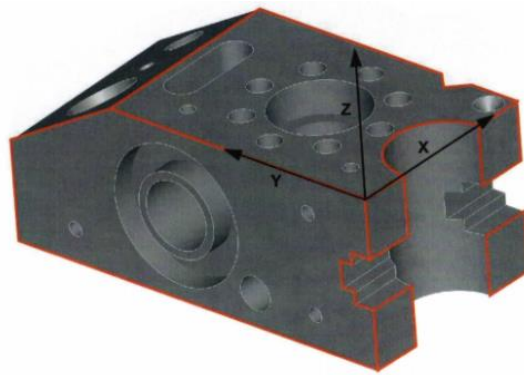


Figure 34. Rotary table coordinate system calibration

After this step, the tool is calibrated and ready to create the preliminary setups for the part measurement.

One of the early requirements for the part measurement is to set up the dedicated coordinate system for the workpiece. Our workpiece is a square-shaped plate that has a sinusoidal round part on its top. We can use the edges of the square platform to create the local coordinate system.

There are different strategies to create a coordinate system. For each one of these strategies, the intersection between the X, Y, and Z and the direction of 2 axes should be designated. The first approach is by defining 3 points to represent the first plane, 2 points to characterize the orthogonal plane to the first one, and 1 point to represent the last plane. (Figure 35)



*Figure 35. Create a coordinate system with 3 planes*

For the second approach, 2 planes and a center bore can be used. So, it will require at least 3 points to define the bore circumference, 2 points to define the perpendicular plane to the bore axis line, and one last point to characterize the perpendicular plane to the last one. (Figure 36)

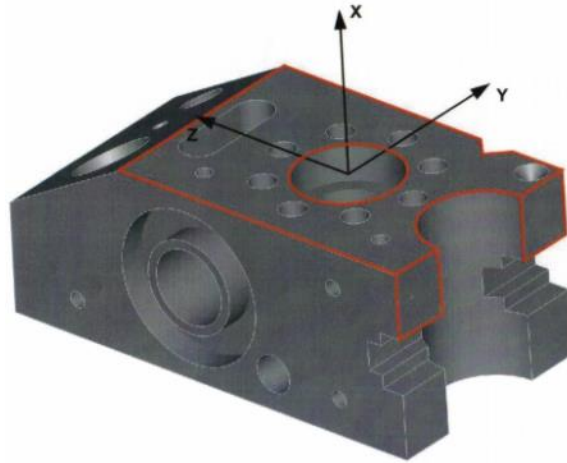


*Figure 36. Create a coordinate system from 2 planes and a center bore*

In the last approach, 1 center bore should be identified by at least 3 points and then 2 points to identify the perpendicular plane to the bore axis and lastly characterize another circle or cylinder center. (Figure 37)

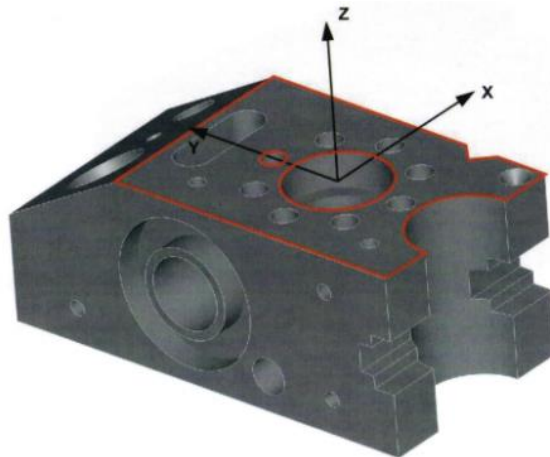


*Figure 37. Create a coordinate system by 1 plane, a center bore, and a directing cylinder*

According to the above approaches, the second method has been used here to identify the coordinating system on our workpiece as in Figure 38. By using “MEPLA”



and identifying at least 3 points on the blue surface, a plane will be created on it. The normal vector to this plane will be used to determine the direction of the Z-axis.

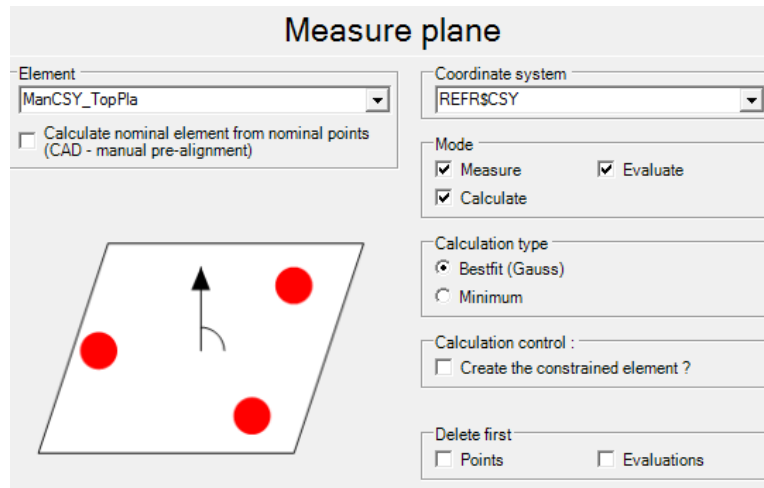


*Figure 38. Create a plane on a surface with 3 points*

In the next step, by using the “MEAXI” command, an axis will be created to characterize the direction of the +Y axis. This axis can be defined by 2 points which will be placed on the frontal slim plane of the part from left to right. (Figure 39)

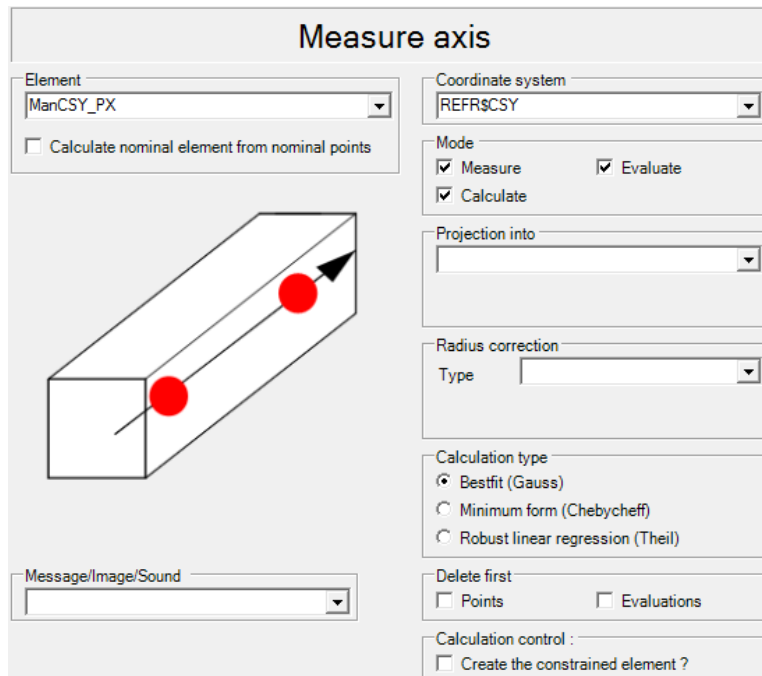


Figure 39. Create an axis using 2 points

After that, the center of the coordinate system should be specified. It would be best to set it up at the center of the short cylindrical shape. So, without changing the probe height, at least 3 points should be located on the cylinder's outside surface to represent a circle. The center of this circle will be where the (0,0,0) of the new coordinate system is going to be addressed. The “MECIR” will create a circle for the system. (Figure 40)

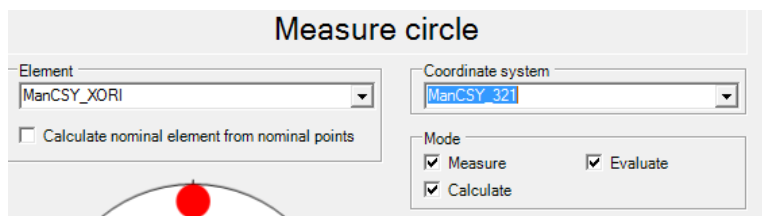


Figure 40. Create a circle by measuring 3 points

In the last step, using the “BLDCSY” command will create and name the coordinate system where these 3 elements meet each other in space. We will use the Cartesian system for our use. (Figure 41)

Figure 41. Create a coordinate system based on 3 elements

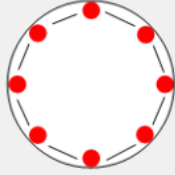
The above procedure to create the coordinate system was performed by the operator controlling the probe navigation. To increase the accuracy of this new coordinate system, it can be replaced by performing automated tool probing for all these steps to eliminate human error on probe movement and angles of incidents to the part.

So, similar to the above steps, first the base plane is measured, and then the +Y axis is measured and lastly a few points around the cylindrical shape will be measured to find its circumference axis.

To create and measure the base plane the “GENCIR” command will create the desired number of points on a selected location on the part by the operator. (Figure 42)

### Generate nominal points on circle

Name of circle <input type="text" value="NXCIR_Upper"/> <input checked="" type="checkbox"/> Delete existing points	Coordinate system <input type="text" value="ManCSY_321"/>
Center coordinate of circle X <input type="text" value="0"/> Y <input type="text" value="30"/> Z <input type="text" value="-5"/>	Measuring plane <input checked="" type="radio"/> XY <input type="radio"/> YZ <input type="radio"/> ZX
Circle diameter <input type="text" value="25"/> <input type="button" value="Get position from CAD"/>	Circle type <input checked="" type="radio"/> Internal <input type="radio"/> External <input type="radio"/> positiv <input type="radio"/> negativ



Number of points <input type="text" value="10"/>	Rotary table position <input type="text" value="0"/>	Start angle of arc <input type="text" value="-85"/>
Clearance point distance <input type="text" value="10"/>	Rotary table offset <input type="text" value="0"/>	End angle of arc <input type="text" value="85"/>

Figure 42. Create circular points to measure the plane surface

The “COLNPT” collects the nominal points in a measurement group. (Figure 43)

### Collect nominal points (NPT's)

Result element <input type="text" value="NYPLA_COLNPT"/> <input checked="" type="checkbox"/> Delete existing points <input checked="" type="checkbox"/> Override NPT names	Coordinate system <input type="text" value="ManCSY_321"/> From point ... <input type="text"/> ...to point <input type="text"/>
Elements with nominal points <input type="text" value="NYPLA_Sec1, NYPLA_Sec2"/>	

Figure 43. Collect nominal points

The “MEPLA” will start measuring the two groups of five points on two sides of the part to create the base plane passing through the average height of all the ten points.

Similar to plane creation, to create the +Y axis, the “GENAXI” is used to define the considered points on the frontal slim surface of the part to be measured. Then the “MEAXI” will start measuring those points.

After that, to find the cylinder center, since it has five taller lateral walls, by using “GENCIR” five times and limiting measuring angles for each to the pertaining wall, 27 points are created around the cylindrical shape, and by “COLNPT” they are collected in one same group together to be measured. The “MECIR” will measure the designated angles of the round shape to measure all 27 points.

Lastly, to create the newer coordinate system with these collected measurements, the “BLDCSY” is used and the generated normal vector to the base plane as the +Z direction, the +Y axis direction, and the center of the circle is used to establish the more accurate coordinate system at the center of the cylindrical part which the Z=0 is at the blue base plane level. From this point, this new coordinate system will be used to address the part measurement points by the “USECSY” command. (Figure 44)

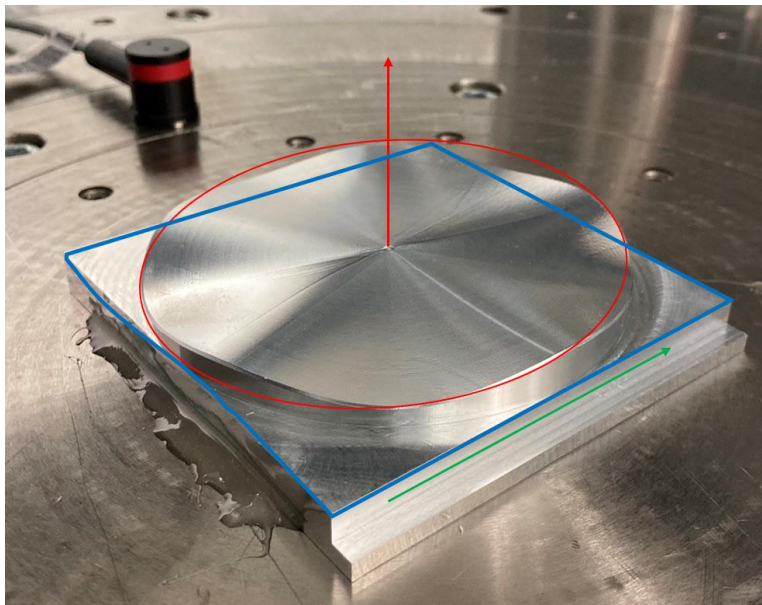


Figure 44. Coordinate system on the workpiece

After setting up the high-accuracy coordinate system with automatic commands in the center of the round shape, the part is ready to be measured. Hence, there are two datasets that CMM needs to take. First is the high-accuracy, low-density dataset which will be comprised of 135 points and second is the high-accuracy, high-density dataset including 4680 points which is used as the reference dataset to compare the final fusion result.

The reason for 135 points as the high-accuracy low-density dataset is to spread the points in the part surface with the same arc distance from each other. Since the part has a radius of 50 mm, we decided to spread the points on the radial interval of 5 mm from each other. So, on the imaginary circle with a 5 mm radius, we have 3 points. It means that the arc distance between them is  $2 \cdot 5 \cdot \pi / 3$  which is equal to 10.472 mm.

Therefore, to keep the same arc distance, on the circle with a 10 mm radius, we need 6 points. With the same logic, the total number of points for the whole part will follow the rule in Figure 45.

Radius	Diameter	Circumference	# of points	Arc length
5	10	31.42	3	10.472
10	20	62.83	6	10.472
15	30	94.25	9	10.472
20	40	125.66	12	10.472
25	50	157.08	15	10.472
30	60	188.50	18	10.472
35	70	219.91	21	10.472
40	80	251.33	24	10.472
45	90	282.74	27	10.472
			135	

Figure 45. 135 points for the high-accuracy low-density dataset

To create a route map of these points, we use the “GENCIR” command to generate the points on each ring. Since there are 9 rings with 5 mm intervals, we use this command 9 times to construct the data grid separately. Once all the 135 points are generated, by using the “COLNPT” we collect all the 135 nominal points in one group.

One of the reports to look at when this measurement is complete is the surface flatness which will be compared to the distance from the based plane where  $Z=0$ . Therefore, we call that plane again by the “MEPLA” command, and then by using the “FLATNES” command we address the reference plane to calculate the results.

The last part to measure all these points is to write a for loop to get the value of each measurement and put it into a list. To open this list, we use the “OPEN” command and address the destined file. (Figure 46)

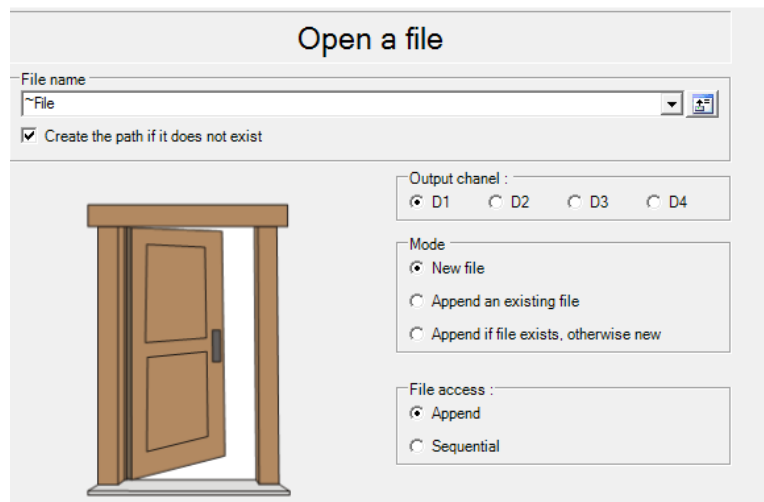


Figure 46. OPEN a new file on QUINDOS

To start the for loop we use the “DO” command to create chain rules to be iterated. (Figure 47)

The image shows a software interface titled "Loop of commands". It contains a central graphic of a circle with the word "DO" in the middle and a downward arrow at the top and a rightward arrow at the bottom, indicating a loop. To the right of this graphic are four input fields: "Loop variable" with the value "K", "From" with the value "1", "To" with the value "Npts", and "Step" with the value "1".

Figure 47. For loop command

The first command in the for loop is the “GETVALS” to navigate the probe to the destination point and take the measurement. Then by using “DFNUVS” the height of the measured point is defined based on the new coordinate system and by using the “LISUVS” will be stored in the list that was created earlier.

The for loop above will be iterated 135 until all the points are measured and to finish this cycle, “ENDDO” will end the for loop, and “CLOSE” will close the generated list of the surface height at each given X and Y. Finally, to save this script the “SAVE” command will rewrite it on the destination path. (Figure 48)



**Save workpiece data (program)**

File name  
C:\Quindos7Users\YP5\2018SGMM\GMMIpp\_YP

Workpiece

Save ...  
☒ Command buffer    ☐ with password  
☐ Analyze file  
 Number of old versions kept:

Objects

Liste CHS and QUE

Status  
 Save NDB?

Database  
 Source:   
 Destination:

Name of history record

If used in parallel buffer  
☒ Standard execution  
☐ Execute in procedure, then stop in main program  
☐ Execute in procedure, then continue

*Figure 48. Save the script*

For the high-accuracy high-density dataset, which is comprised of 4680 points, the same concept will be repeated. The reason for choosing 4680 points is to increase the number of measurement nodes by the CMM on the part. These points are spread through concentric rings around the center of the part. The smallest radius is 1.25 mm, and they are increased by increments of 0.25 mm until they reach the radius of 48.75 mm. This will generate 39 rings, where all the points on each ring are distributed with the same arc length from each other. The number of points on each ring is in Figure 49.

Radius	Diameter	circumference	# of points	Arc length
1.25	2.5	7.85	6	1.308997
2.5	5	15.71	12	1.308997
3.75	7.5	23.56	18	1.308997
5	10	31.42	24	1.308997
6.25	12.5	39.27	30	1.308997
7.5	15	47.12	36	1.308997
8.75	17.5	54.98	42	1.308997
10	20	62.83	48	1.308997
11.25	22.5	70.69	54	1.308997
12.5	25	78.54	60	1.308997
13.75	27.5	86.39	66	1.308997
15	30	94.25	72	1.308997
16.25	32.5	102.10	78	1.308997
17.5	35	109.96	84	1.308997
18.75	37.5	117.81	90	1.308997
20	40	125.66	96	1.308997
21.25	42.5	133.52	102	1.308997
22.5	45	141.37	108	1.308997
23.75	47.5	149.23	114	1.308997
25	50	157.08	120	1.308997
26.25	52.5	164.93	126	1.308997
27.5	55	172.79	132	1.308997
28.75	57.5	180.64	138	1.308997
30	60	188.50	144	1.308997
31.25	62.5	196.35	150	1.308997
32.5	65	204.20	156	1.308997
33.75	67.5	212.06	162	1.308997
35	70	219.91	168	1.308997
36.25	72.5	227.77	174	1.308997
37.5	75	235.62	180	1.308997
38.75	77.5	243.47	186	1.308997
40	80	251.33	192	1.308997
41.25	82.5	259.18	198	1.308997
42.5	85	267.04	204	1.308997
43.75	87.5	274.89	210	1.308997
45	90	282.74	216	1.308997
46.25	92.5	290.60	222	1.308997
47.5	95	298.45	228	1.308997
48.75	97.5	306.31	234	1.308997
			4680	

Figure 49. 4680 points for the high-accuracy high-density dataset

Similar to the previous measurement, to program the CMM to measure these 4680 points, we use the “GENCIR” command 39 times to create all the rings and distribute the points proportionately. Then by the “COLNPT”, we collect all the 4680 points into one group, and by recalling “MEPLA” and “FLATNES” we establish the

flatness measurement. Then the same for loop is used to measure all the 4680 points on the part and finally save them in a separate txt file. This will conclude the whole process for CMM data acquisition.

### 3.4.3 Laser scanner measuring strategy

The articulate arm laser scanner is the low-accuracy high-density data channel that compared to the CMM, has a much faster data acquisition and less complication to set up. Since there is no physical contact with the part, there is no need to attach the part to the measurement table as long as the part is stationary during the measurement.

To enhance the laser scanner measurement accuracy the operator should adjust the arm distance and hovering speed over the part. The laser scanner illuminates two separate patterns on the part. One is a dot, and the other is a line. They are designed to identify the ideal distance of the arm from the workpiece. Therefore, the operator should adjust the distance to keep the dot on the line most of the time. There is a bar chart on the computer software that shows the arm's ideal distance and speed in real time. In the end, the measurement profile will be saved as a \*.xit64 file extension which can be opened by "SpatialAnalyzer" software. In this software, the user can analyze a variety of actions on the 3D model. (Figure 50)



*Figure 50. Articulate arm laser scanner over the part*

One of the steps before measuring the part is to define the coordinate system (CS) as the initial reference point. One of the software options for this reference point is the base center of the articulate arm pole. By taking this as the initial reference point the measurement can be started. After measuring the part and importing the xit64 file to the SpatialAnalyzer software, there are a few things that need to be prepared before analyzing the dataset. Firstly, the data from the surrounding part is not needed here and should be trimmed from the original dataset. Secondly, the data density is not consistent across the part, therefore it should be purified to get uniform data density. The raw dataset shows about 4,400,000 lines for X, Y, and Z. This is a huge amount of data for a small part to process. (Figure 51)

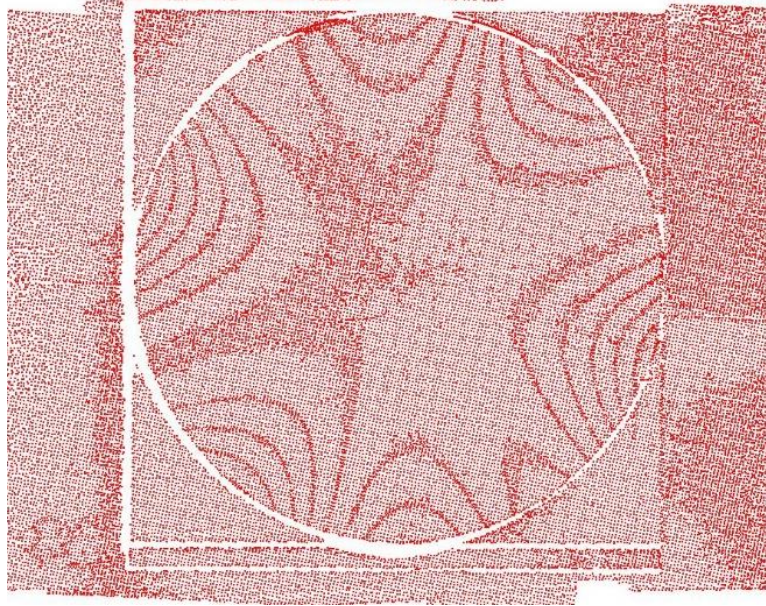


*Figure 51. Laser scanner raw dataset of the part*

After trimming the excessive dataset, to normalize its density, two approaches can be taken to thin the data. The first is to scale the dataset by taking 1 point in every  $N$  dataset as their representative. The issue with this method is that it will not eliminate the uneven data density across the part.

The second method is by using a spatial filter to define small voxels in the dataset area, and for every point that fits in voxels, the  $Z$  average value will be its representer. There is another advantage in this method which can eliminate the outliers in the dataset by defining the minimum points per voxel. If any voxel does not meet that threshold, it will be removed from the dataset. In this study, we defined our voxels as 0.635 mm cubes, and the threshold for each is considered as 65 points. This will squeeze down the number of points from 4,400,00 to 26,400.

The next step in preparing this dataset is to define the coordinate system in the same way as the CMM. It is a crucial step to align these two coordinate systems in the same direction and orientation. For this purpose, in the SpatialAnalyzer software, we define the cylindrical part, the base platform, and the two-step walls. Similar to the CMM, a plane is represented by taking at least 3 points on the base platform. The normal vector to this plane is characterized as the +Z vector direction. Then by defining a line along the vertical frontal wall, the +Y direction of the coordinate system is specified. Lastly, by calculating the center of the cylindrical part over points on its circumference, it serves as the center of the coordinate system. By assembling the +Y and +Z vectors over that center, the part's coordinate system based on the articulate arm laser scanner is defined in Figure 52. One last step before analyzing the dataset is to transform the points from the initial coordinate system, which was built over the articulate arm base center, to the new coordinate system at the center of the part. This process is called the "Homogeneous Transformation Matrix" which applies the translation vector and rotation matrix to the coordinate values within the initial CS to transform them into the new CS.[70]

The translation and rotation matrix that was applied to the laser scanner raw coordinates were as below:

Translation (mm):  $dx = 658.72$ ,  $dy = 11.93$ ,  $dz = 1.53$ ,  $dMag = 658.83$

Rotation (deg):  $Rx = -0.0777$ ,  $Ry = 0.0436$ ,  $Rz = 0.7811$ , Total Angle = 0.7862



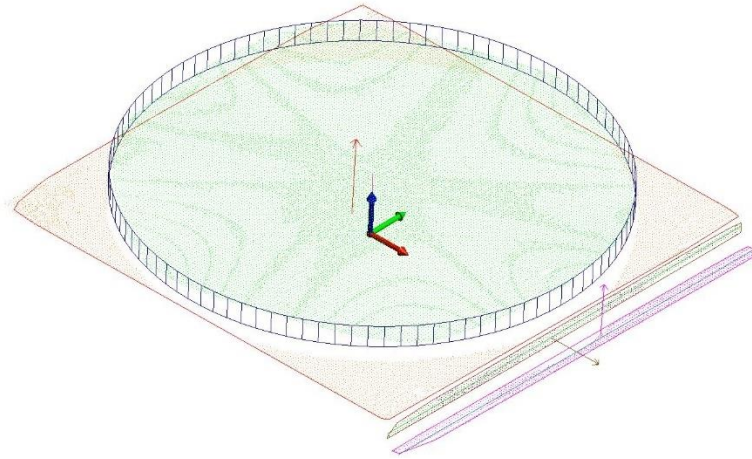


*Figure 52. A new coordinate system on the workpiece geometry acquired by the laser scanner*

#### 3.4.4 Data fusion strategy

After acquiring the high-accuracy and low-accuracy raw datasets from our different channels, there are multiple steps to prepare the data for the fusion process. To start using the high-accuracy low-density dataset obtained from the CMM we should consider the fact that the part does not have a flat surface and the angle of incident between the CMM stylus tip, and the part surface is not always along the Z vector.

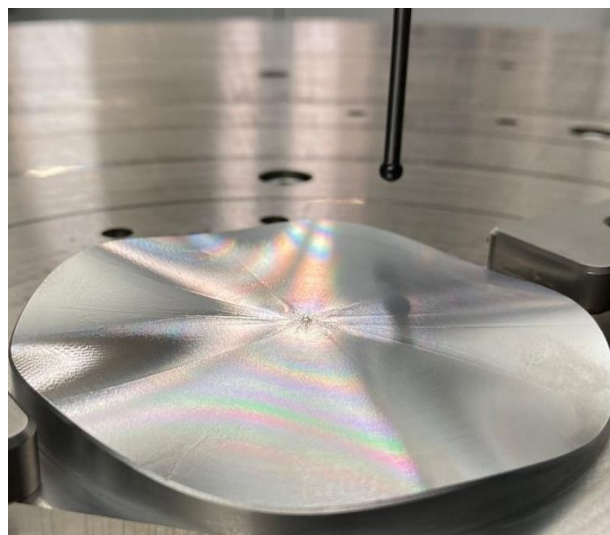


*Figure 53. Freeform surface workpiece and the CMM stylus tip*

When the CMM stylus touches the surface of a workpiece, the recorded data points are the coordinates of the stylus center in that location. Since we are looking for the actual incident coordinates of the surface, we need to compensate for this offset. The point of incident between the workpiece surface and the stylus tip is always orthogonal to the surface slope.

Hence, by calculating the surface partial derivative components at the point of CMM contacts, their products would indicate the normal vectors. By using the normal vector directions, we can calculate the coordinates of the stylus surface at the incident points. This can be achieved by using the stylus center coordinates and moving 2.5 mm (stylus radius) backward along the corresponding normal vector direction toward the workpiece and computing the coordinate of the stylus surface. The resulting data points are the coordinates where the stylus touches the workpiece surface. (Figure 54-55)

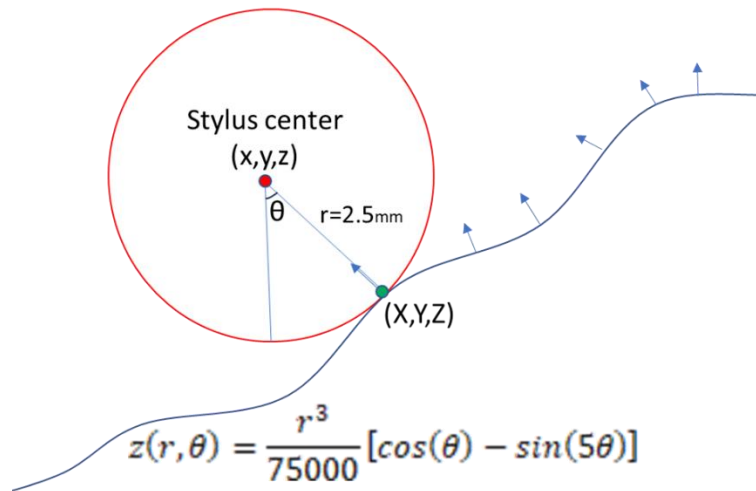


Figure 54. Correction for the stylus nominal height through the surface slope



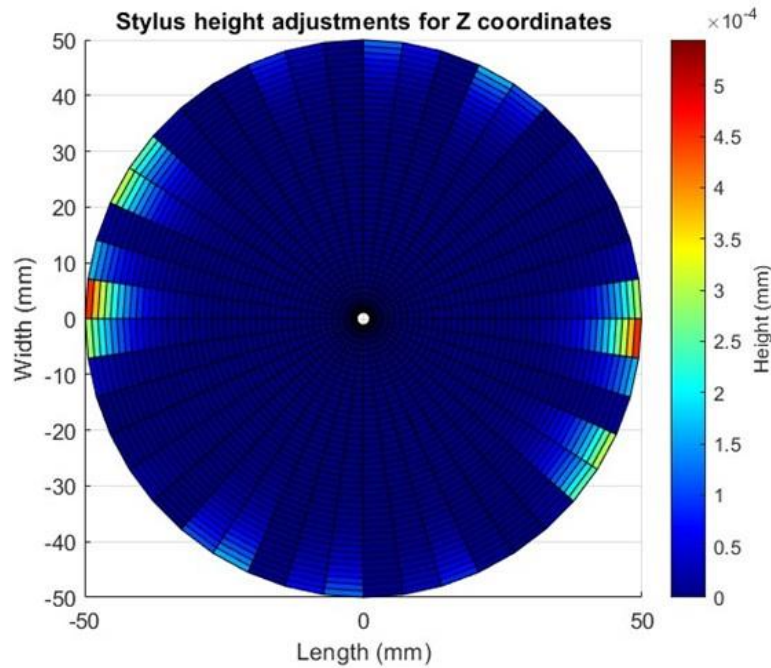


Figure 55. Stylus height adjustment based on surface partial derivative

After finding the height correction values, they should be subtracted from the nominal Z value for all measured points by CMM. The new dataset will be used for the next steps. Figure 56 schematically shows both datasets together.

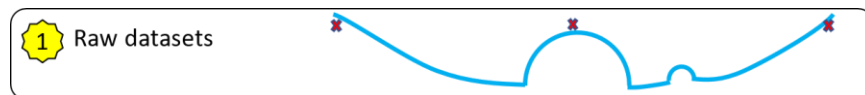


Figure 56. High-density low-accuracy and low-density high-accuracy datasets

Similar to the 2D model strategy, we start with Gaussian filtering by passing the low-accuracy high-density data between two bands which are defined by the sigma value. The sigma value performs as data filtering by standard deviation using a Gaussian smoothing kernel. The sigma value should be determined based on the data specification and error frequencies. The low-pass Gaussian filter is used for smoothing

and noise reduction while preserving large-scale features, whereas the high-pass Gaussian filter is used for isolating fine details and small-scale variations while filtering out large-scale features. Subtracting the high-density low-accuracy raw dataset from the summation of the low-pass and high-pass Gaussian filters yields extracted defects from the surface.

```
Z2_gaus_low = imgaussfilt(Z2_sml,0.25);
Z2_gaus_high = imgaussfilt(Z2_sml,25);
Z2_gaus_band = (Z2_gaus_low + Z2_gaus_high)-Z2_sml;
```

The product of this bandpass filter would be a high-density point cloud in which its surface shape is removed by the high-pass filter its surface noise is removed by the low-pass filter and the local defects are the only surface features that are left. Figure 57 shows this step schematically.



*Figure 57. Gaussian filtered defects from high-density low-accuracy dataset*

In the next step, we will make the high-density dataset sparse by separating selected points from it. These selected points are the same number as the low-density dataset. The specification of these 135 points from the high-density dataset, is that they are the closest neighbors to their corresponding low-density dataset counterparts. This selection is applied to the Gaussian-filtered defects dataset and therefore it does not have the surface shape or surface noise with it. The script and schematic are as Figure 58.

```

nbr_LD = knnsearch(AA_LD_sm1(:,1:2),CMM_LD_cor(:,1:2));
Z2_adj = Z2_gaus_band(nbr_LD,1);

```



Figure 58. Separated points from the Gaussian-filtered high-density low-accuracy dataset

In the next step, these 135 points from the Gaussian-filtered high-density low-accuracy dataset are subtracted from their corresponding 135 points on the low-density high-accuracy dataset. With this step, the remainder would be the surface which keeps the shape feature of the part but its local defects are removed. This would represent the CMM points without the local defects. The script and schematic are as Figure 59.

```

Z1_adj = Z1 - Z2_adj;

```



Figure 59. Subtracting 135 points laser arm data from their CMM points counterparts

In the next step, the 135 points from the previous step will be interpolated to get as condensed as the initial high-density dataset (26,400 points). This will generate a dataset over the CMM defect-free points which are connected through Biharmonic spline interpolation. There are different interpolation methods for 2D scattered data including "linear" which is triangulation by linear interpolation, "nearest" which is triangulation by nearest neighbor interpolation, "cubic" which is a triangulation by cubic interpolation, "natural" which is a triangulation by natural neighbor interpolation and is an efficient tradeoff between linear and cubic and lastly, "v4" which is Biharmonic spline

interpolation. The Biharmonic spline interpolation surface is a linear combination of Green functions centered at each data point and its amplitudes are found by solving a linear system of equations.[71, 72] The script and schematic are as Figure 60.

```
Z1_dense = griddata(X1,Y1,Z1_adj,X2_sml,Y2_sml, 'v4');
```



Figure 60. Interpolated CMM defect-free points

The last step in achieving the fusion result is to add the Gaussian-filtered local defects from the second step to the interpolated CMM defect-free dataset from the previous step. Both datasets are comprised of the same density and their corresponding matrices can be summed up. The script and schematic are as Figure 61.

```
Z_fused = Z2_gaus_band + Z1_dense;
```

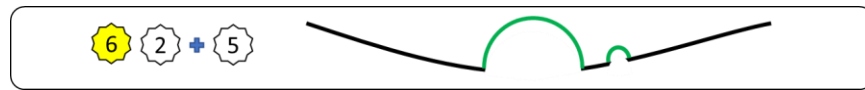


Figure 61. Adding the extracted local defects to the CMM defect-free interpolated dataset

The result generated from this step would conclude the final fusion result from the two input channels.

### 3.4.5 Data fusion analysis

To evaluate the generated fusion result, we can compare it with the high-density high-accuracy dataset which was measured by the CMM according to the 4680 points that were explained at the beginning of this chapter.

First, the 135 high-accuracy low-density points are compared to their counterpoint from the 4680 high-density high-accuracy datasets (reference benchmark dataset) to check their initial offset.

Next, the same process is pursued for the articulate arm laser scanner to compare the raw Z values with the reference dataset. Hence, the 4680 points from the laser scanner dataset which are the closest neighbors to the CMM points, are compared to evaluate the initial Z differences. At this point, we have compared the raw CMM and laser scanner measurements with the reference value to understand our baseline.

Then, the fusion result generated based on the 135 CMM points and 26,400 laser scanner points are compared with the reference dataset. Since the data fusion result has 26,400 points and the reference dataset has 4680 points, we need to select corresponding points for comparison. Therefore, the 4680 points from the fusion result which are closest neighbors to their high-density CMM points counterparts are selected for this comparison. Then the average Z difference and the standard deviation between them will be calculated. This will reveal the resulting improvement from the data fusion compared to each one of the input channels.

On the next move, we want to evaluate the data fusion accuracy dependency on the CMM (low-density high-accuracy channel) number of the points. For this purpose, we would decrease the number of CMM points from 135 points down to lower values and compare the fusion-generated result with the reference benchmark dataset. These lower CMM point steps are 75 points, 45 points, and 15 points. By this comparison, the CMM contribution to the generated fusion result accuracy can be assessed.

### 3.5 3D experiment

For the 3D project, we used a steam turbine exhaust muffler workpiece which has a cylindrical shape and various diameters at different cross sections. These diameters range from 250 mm to 270 mm for the outer surface of the measuring area where the low-density high-accuracy dataset was collected. (Figure 62)



*Figure 62. steam turbine exhaust muffler used for the 3D data fusion*

This part was measured by the ATOS GOM 3D Scan with 12 megapixels resolution for the high-density low-accuracy dataset. The 3D scanner was placed and locked in place to make a complete measurement of the inner and outer walls. This measurement generated a point cloud containing approximately 5 million points. Then the result was analyzed using SpatialAnalyzer software. (Figure 63-64)

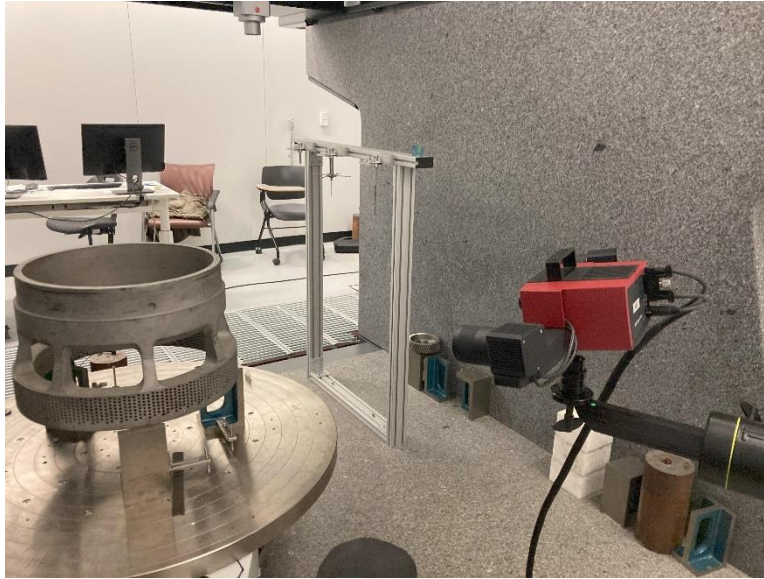


*Figure 63. ATOS GOM 3D Scan to measure the aerial topography*

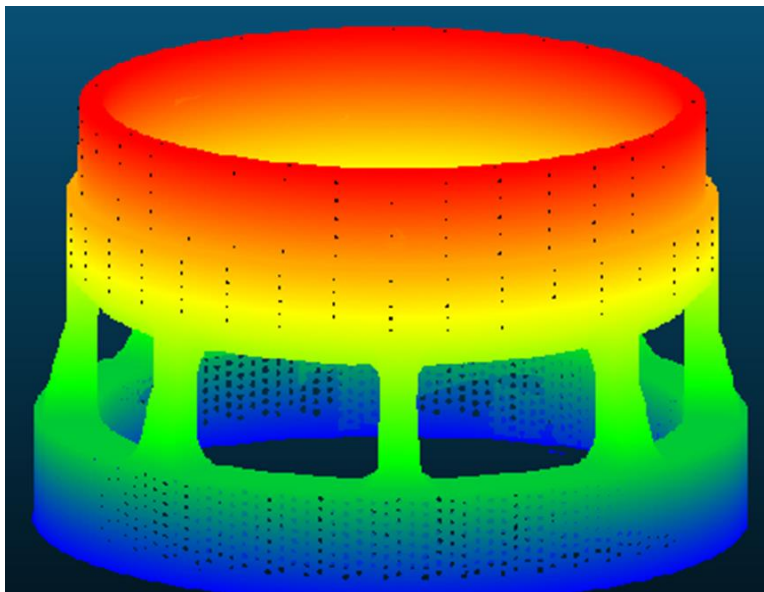


*Figure 64. High-density point cloud of the cylinder part which measured by the 3D scanner*

Next, to collect the low-density high-accuracy dataset from CMM, the workpiece was placed on the CMM rotary table and allowed to rest for 1 day to reach thermal equilibrium with the lab temperature. (Figure 65-66)





*Figure 65. The cylinder part on the CMM rotary table*

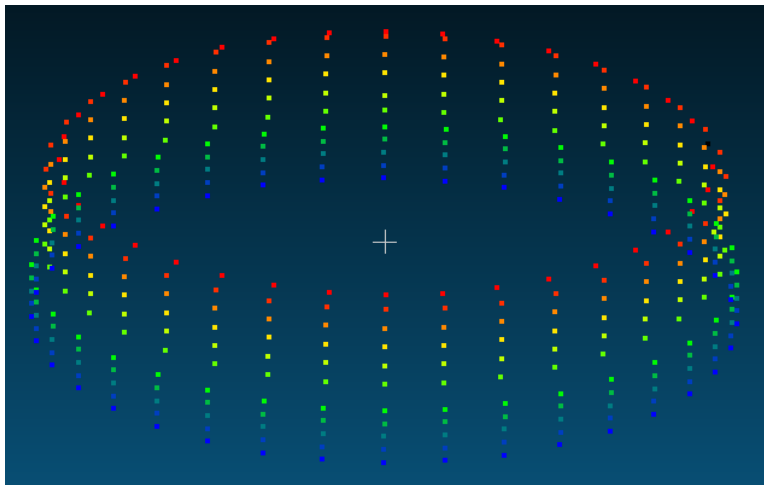


*Figure 66. High-accuracy low-density point cloud collected by CMM*



Similar to 2D, the two datasets were aligned to maintain the same coordinate system center and axes directions. Hence, in the beginning for the coarse alignment of the two datasets, the two indicators on the workpiece were used. These indicators are four small holes located on the cylinder's outer surface. Two points of the CMM dataset are taken from of pair of these holes which makes the alignment possible. (Figure 67)

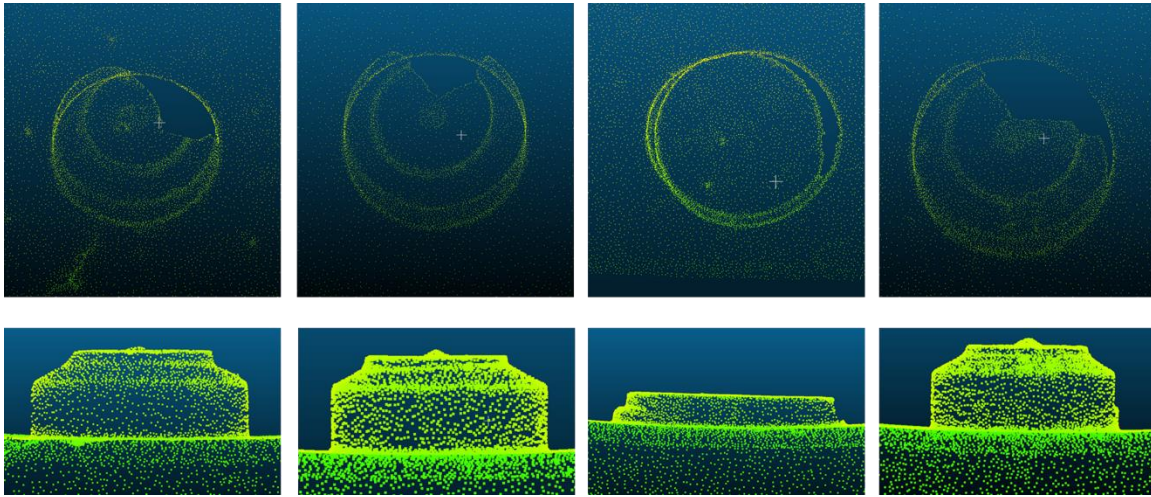


*Figure 67. Alignment markers on part surface front view and top cross-section*

After aligning two datasets, the new retrieved coordinates are utilized for further processing. To classify the points based on their radius, the coordinates are converted from Cartesian to cylindrical. Similar to the 2D section mentioned above, the Gaussian filter was applied to remove the noise and leave us with the residual local defects. In the next step, the nearest neighbor of CMM points from the Gaussian-filtered dataset were extracted. The defects were detracted from the CMM dataset, and the remaining points were interpolated by comparing linear, nearest, cubic, and radial basis functions. Lastly, the extracted defects were added to the interpolated surface to generate the fused surface point cloud.

## 4 Results

In this section, the scripts that are developed in MATLAB are executed and the results for the 1D model, 2D model, and 2D experiments are explained.

### 4.1 1D model

As explained in the methodology section there are 3 approaches for the 1D model that are implemented to fuse the high-accuracy (spars) and low-accuracy (dense) datasets. The results for each of these approaches are explained in this section.

#### 4.1.1 Polynomial and moving average fitting

In the first approach, the high-accuracy model is comprised of 10 points with 100 mm intervals along a 1000 mm profile. (Figure 68)

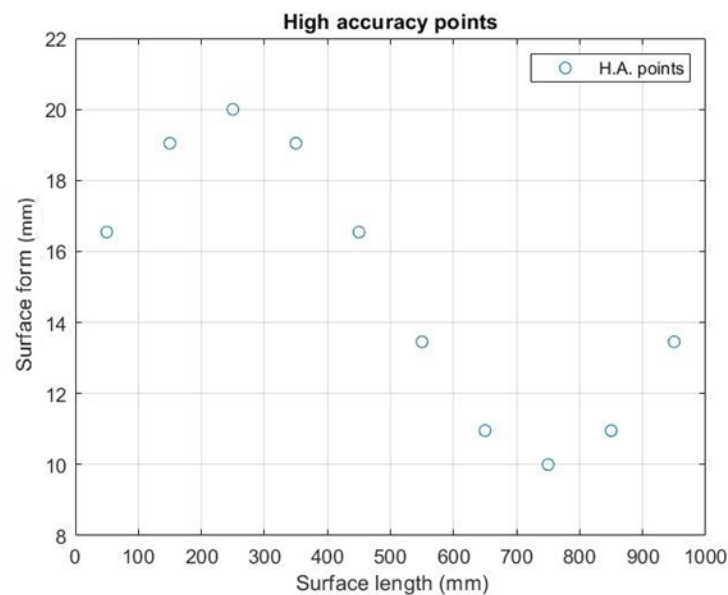


Figure 68. High accuracy points

Next, the high-accuracy points are fitted with the same resolution as the low-accuracy dataset (1mm interval) using the Polynomial fitting with order 9. This will result in a smooth line passing through all the high-accuracy points. (Figure 69)

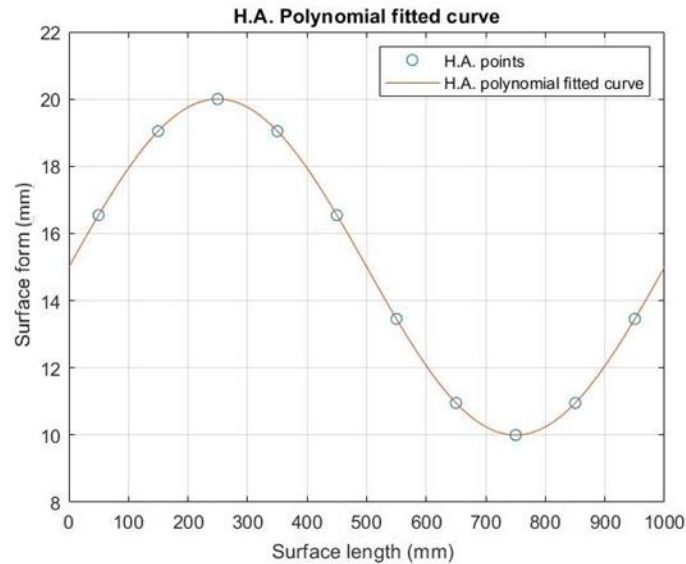


Figure 69. Polynomial fitted high accuracy points

The low-accuracy dataset is comprised of 1001 points along the 1000 mm distance with intervals of 1 mm. This dataset is noisy and therefore is coarse. (Figure 70)

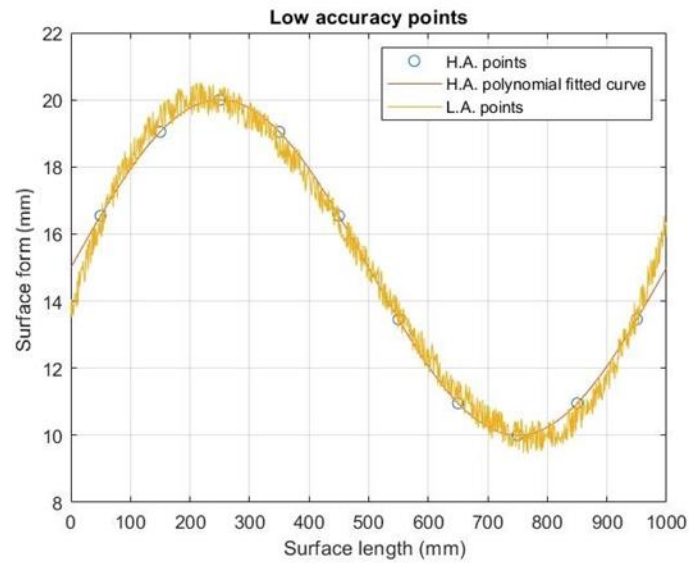


Figure 70. Low accuracy dataset

The moving average of the low-accuracy dataset is calculated at over 15 points in Figure 71.

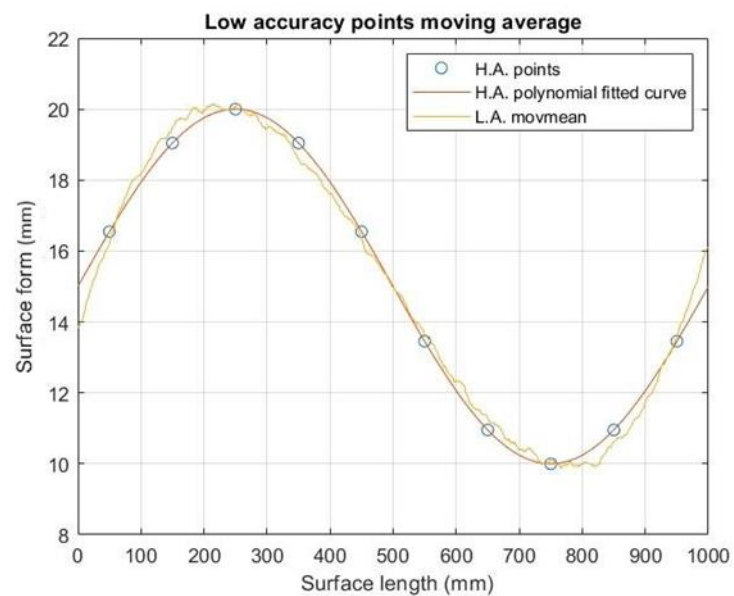


Figure 71. Low accuracy moving average

As the next step, the low accuracy dataset difference with its moving average is calculated to represent the noise level as shown in Figure 72.

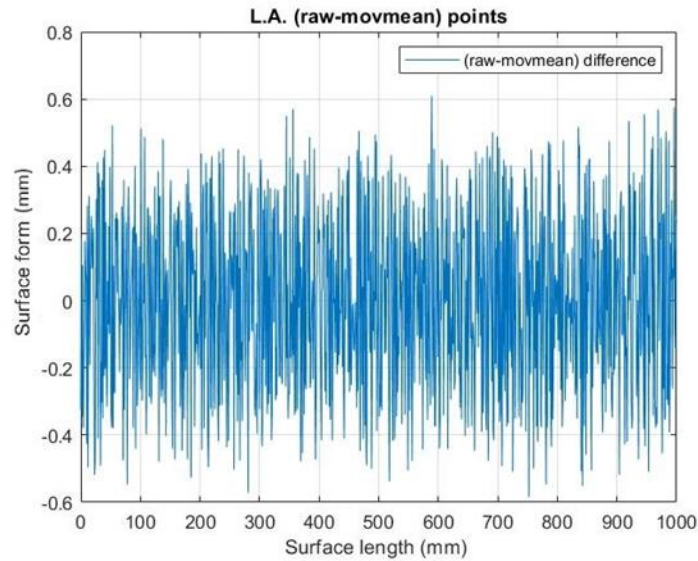


Figure 72. Difference between low accuracy and its moving average

In the next step, the offset calculated in the step above is added to the high-accuracy polynomial fitted curve as illustrated in Figure 73. This procedure aims to take the residuals of the intermediate areas into account for the high-accuracy dataset. This will generate a curve inheriting the surface behavior of the low-accuracy dataset and the local specification of the high-accuracy dataset.

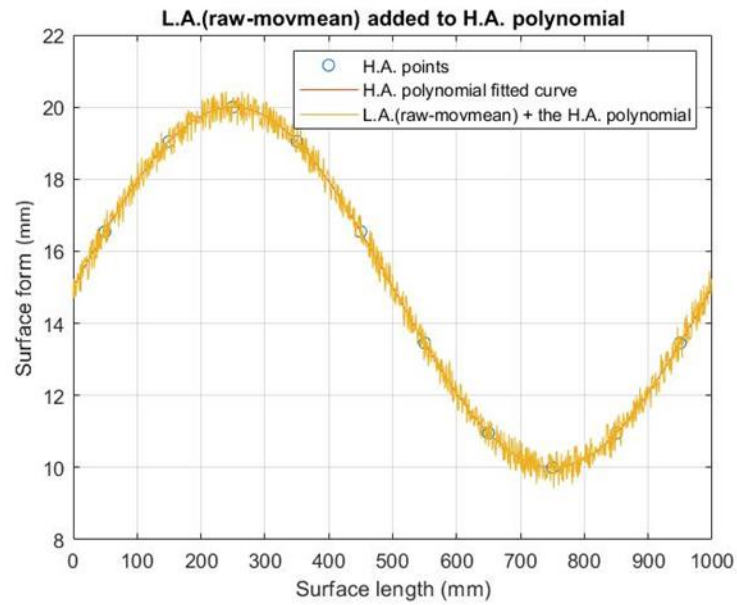


Figure 73. High-accuracy dataset with high-frequency offsets

#### 4.1.2 Spline fitting and moving averages

Here the high accuracy points are fitted by the cubic smoothing spline (Figure 74)

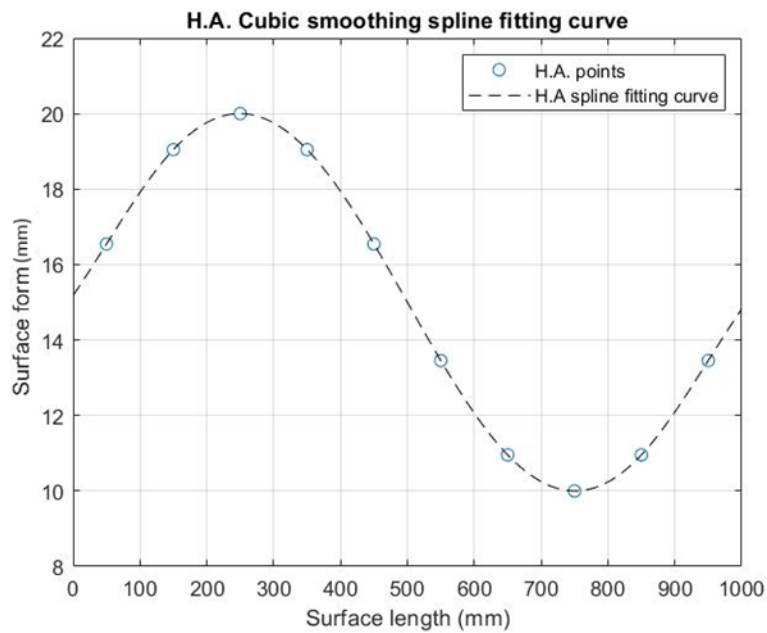


Figure 74. Spline fitted high accuracy points

By applying the moving average on the low accuracy points once by the 15 points and next time by the 45 points two different curves are obtained as Figure 75.

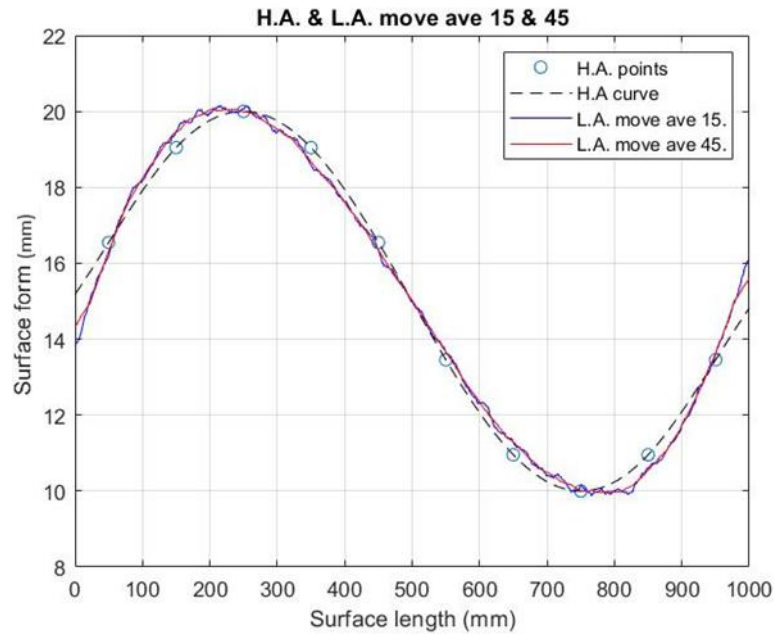
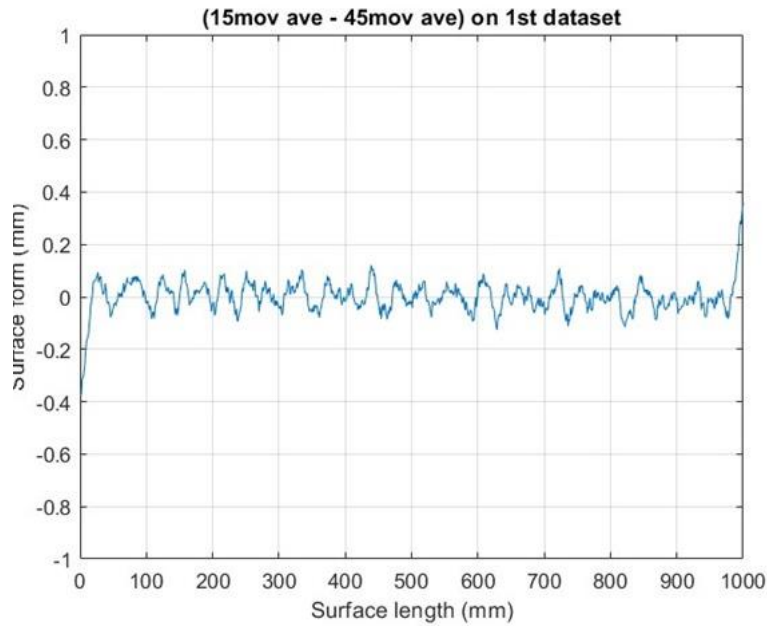


Figure 75. 15 and 45 moving averages on Low accuracy points

Then the difference between these two curves is calculated at each data point as in Figure 76.



*Figure 76. 15 and 45 moving average difference*

This figure can be represented as the high frequency coordinated for the area between the high-accuracy points. So, by adding this figure to the high-accuracy fitted curve the following measurement will be generated as in Figure 77.



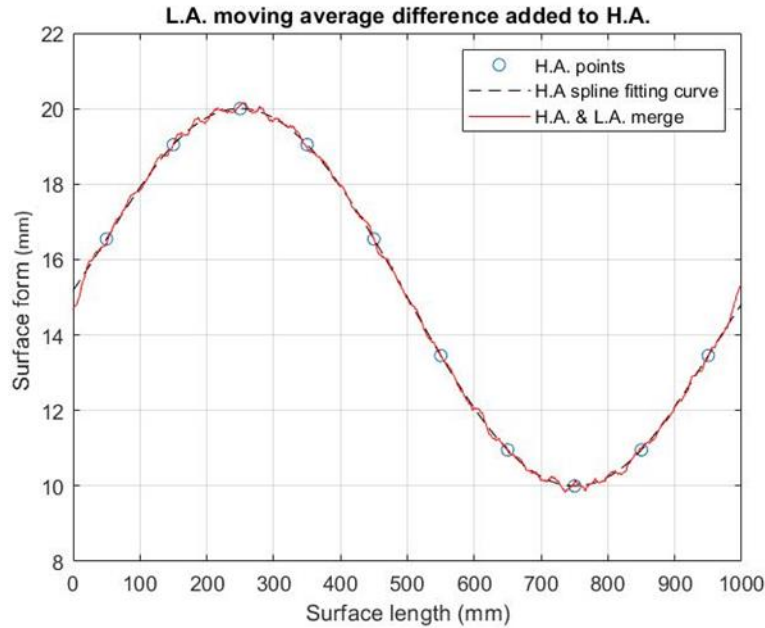


Figure 77. The difference between 15 and 45 moving averages is added to the H.A. fitted curve

The above figure is the representation of the fusion between low-accuracy and high-accuracy datasets based on the spline fitting and moving averages respectively.

#### 4.1.3 Spline fitting and Gaussian filtering

In this method the high-accuracy dataset was fitted by the cubic smoothing spline (similar to the last method) and the coordinates between the high-accuracy points were extracted from the difference between the Gaussian filtering and the 15-moving average on the low-accuracy dataset. (Figure 78)

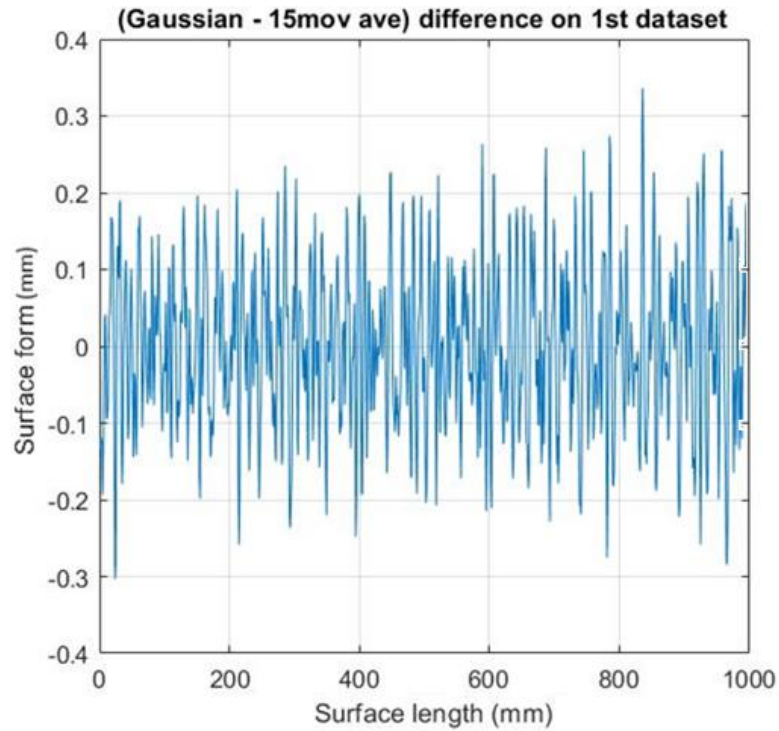


Figure 78. Gaussian filtering and 15 moving average difference on low accuracy dataset

Adding the difference values from Figure 78 to the high-accuracy dataset generates fused data. This fused data is the product of the high-accuracy data points and the local high-frequency positions from the low-accuracy dataset. (Figure 79)

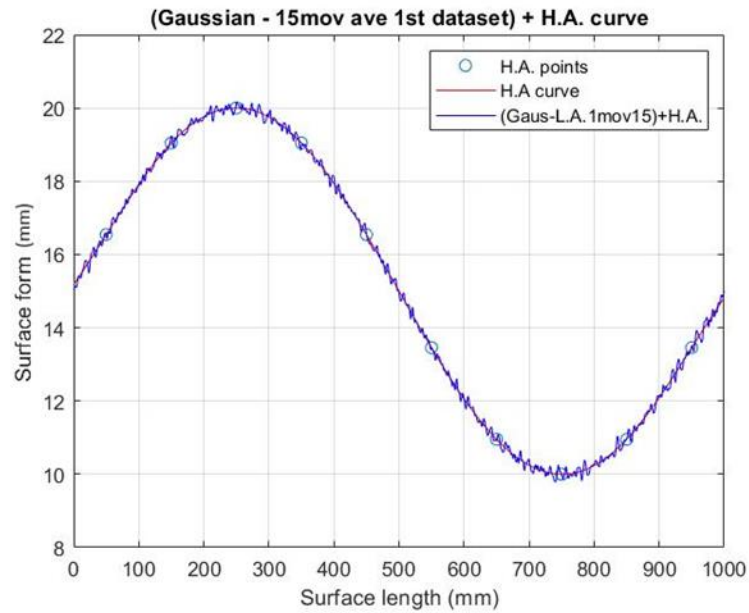


Figure 79. Gaussian fitting and 15 points moving average difference over the low accuracy dataset added to the high accuracy fitted curve

Similar fusion can be performed by 45 moving averages (Figure 80).

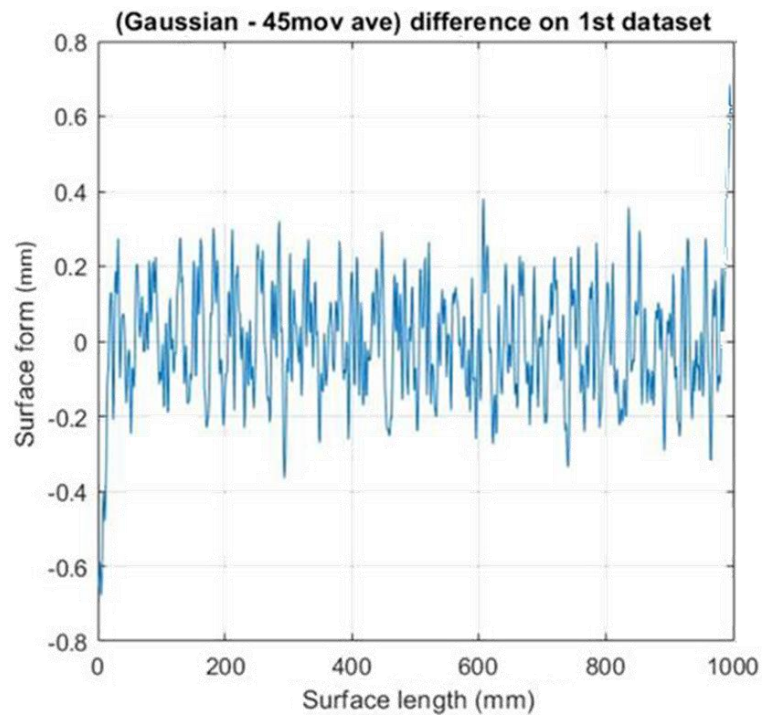


Figure 80. Gaussian filtering and 45 moving average difference on low accuracy dataset

Similarly, by adding this difference value to the Gaussian-filtered low-accuracy dataset Figure 81 is generated.

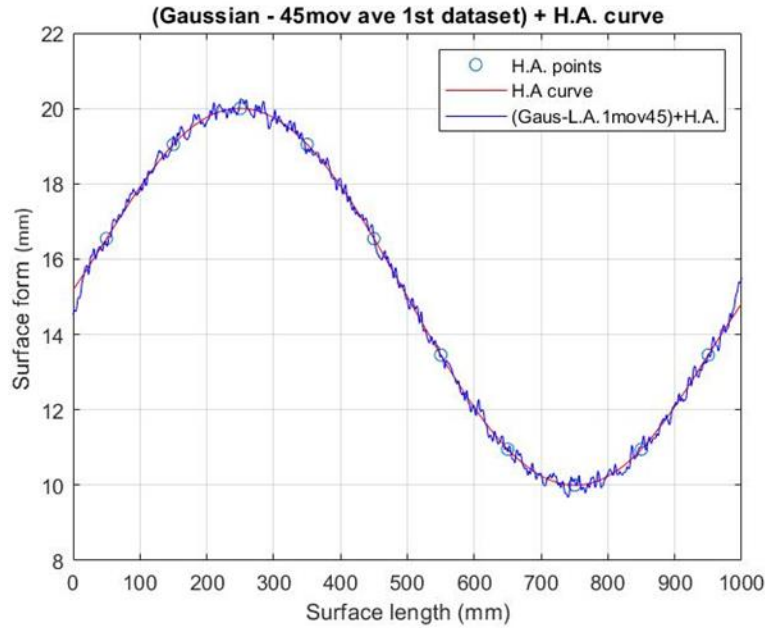


Figure 81. Gaussian fitting and 45 points moving average difference over the low accuracy dataset added to the high accuracy fitted curve

By comparing the 1D results from the above proposed methods, filtering the noise by the Gaussian window has better performance and then adding it to the spline fitted curve of the high-accuracy dataset represents a less deviated result. Hence, for the 2D model, we will utilize the suggested method to separate the noise and add the remaining defects to the interpolated high-density points. It would be important to distinguish the noise from the defects to prevent the elimination of the surface features.

## 4.2 2D model

For the 2D model, we first started creating the actual surface with defects but no noise with 100 mm x 100 mm dimension at high-density resolution. This surface is used as the reference to evaluate the final fusion product's accuracy. (Figure 82)

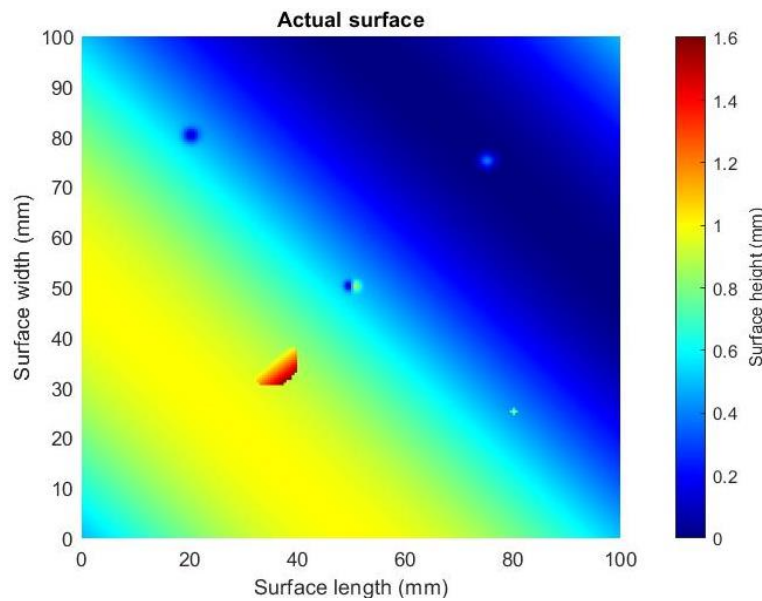


Figure 82. The actual surface model with defects and no noise

Then the low-density, high-accuracy dataset from this model which has the same dimension made by 11 x 11 points (10 mm apart) is created. (Figure 83)

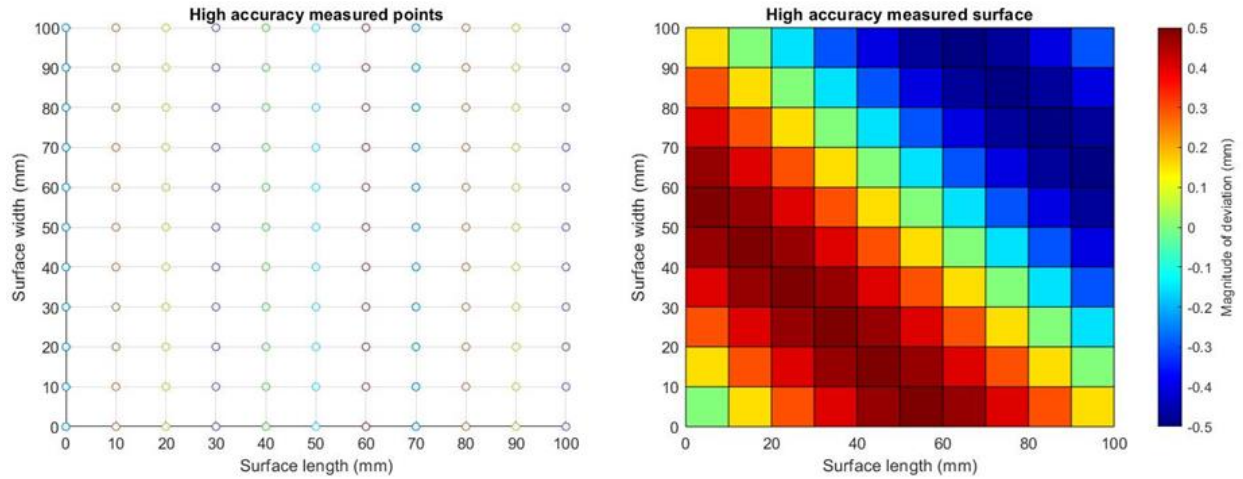


Figure 83. Low-density high-accuracy dataset

On the other hand, the high-density, low-accuracy dataset is generated from the actual surface with the same dimension and resolution of 201 x 201 points (0.5 mm apart) plus added random noise to the surface. (Figure 84)

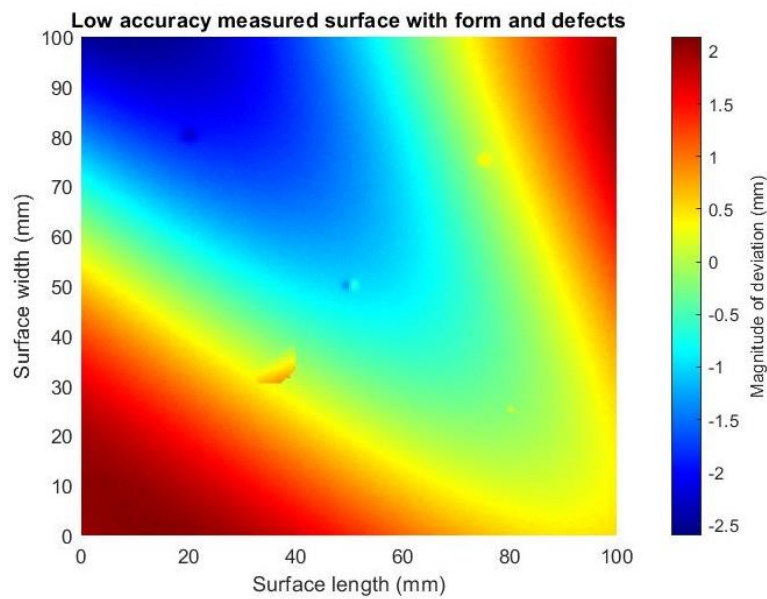


Figure 84. High-density, low-accuracy dataset

In the next step, the Gaussian filter is applied to the low-accuracy, high-density dataset to remove the low-frequency and high-frequency noise by applying the low-pass and high-pass filters separately. By subtracting these two vectors the remainder is the surface which is only inherited from the defects. (Figure 85)

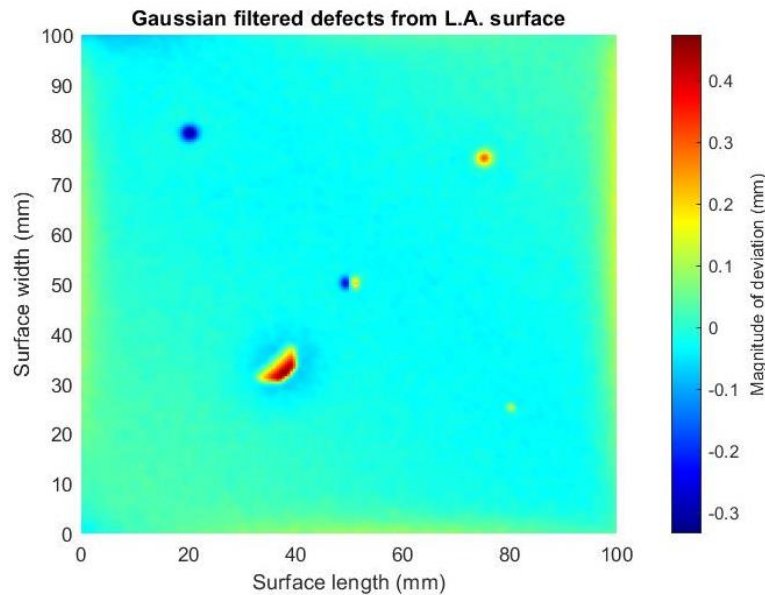


Figure 85. Gaussian-filtered defects from low-accuracy high-density dataset

Then the high-accuracy, low-density dataset with 11x11 datapoints is interpolated to become 201x201 points same as the other dataset density. (Figure 86)

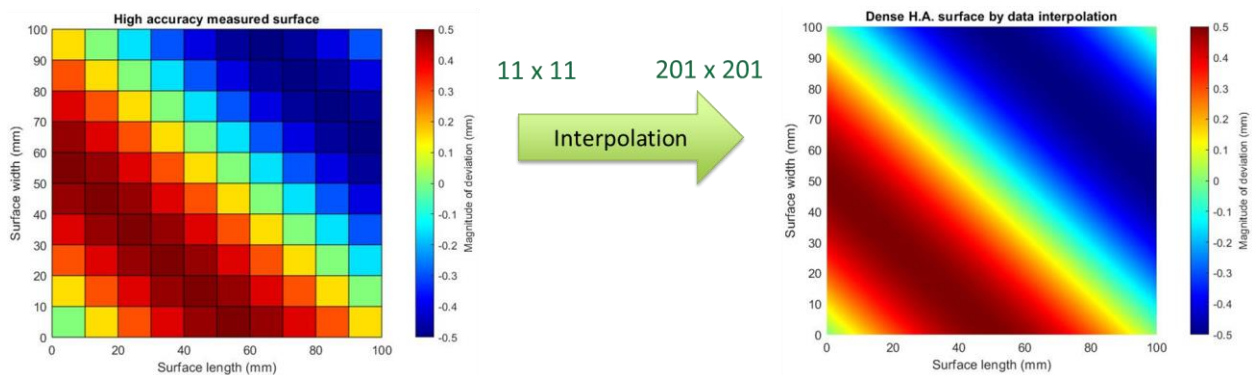
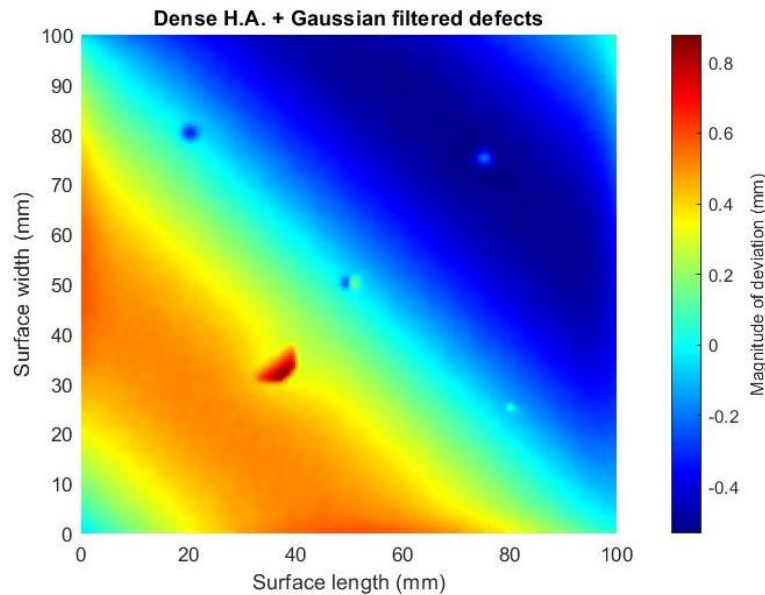


Figure 86. Condensing the high-accuracy dataset by interpolation



After interpolating the high-accuracy dataset it becomes ready to be added to the extracted defects by the Gaussian filter. This would create the estimated surface data fused from both channels. This is the final product of the fusion steps in 2D dimensions.

(Figure 87)



*Figure 87. Estimated surface fused from both channels*

To evaluate the estimated surface, the final fusion result can be compared with the actual surface generated in the early steps. By subtracting the fusion product from the actual surface, Figure 88 is obtained.



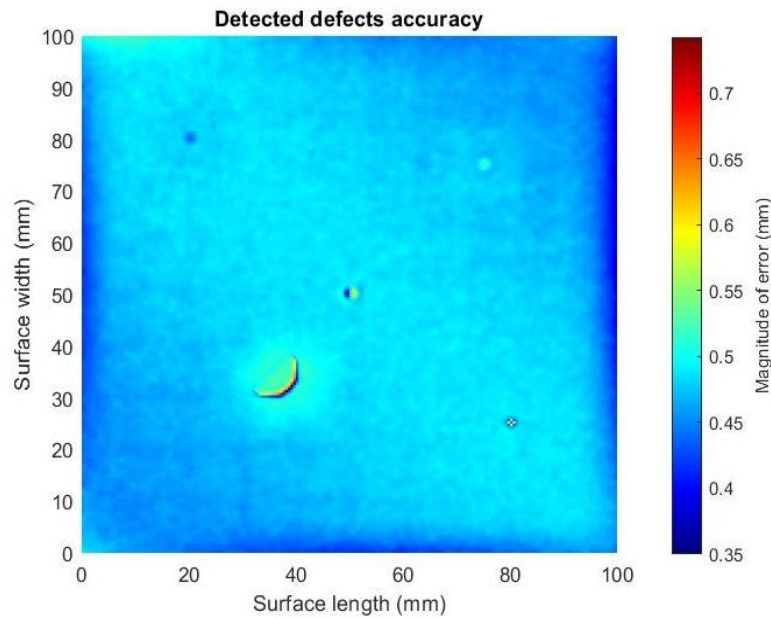


Figure 88. Actual surface and fused data difference

This difference between the actual surface and the fusion result is more severe on the defects' edges and the interpolation method has a more prominent contribution to the intensity of this deviation. Hence, the fusion results generated by the different interpolation methods are compared to investigate their impact on the final product.

To check the final fusion accuracy the range, average, and standard deviation are compared for the linear, spline, cubic, and Akima interpolation methods. (Figure 89-93)

Method	Range (mm)	Average (mm)	StDev (mm)
Linear	0.16667	0.0013	0.0188
Spline	0.1568	0.0012	0.0192
Cubic	0.1524	0.0012	0.0187
Akima	0.152	0.0012	0.0187

Figure 89. Low-density dataset Interpolation methods comparison with the initial actual surface

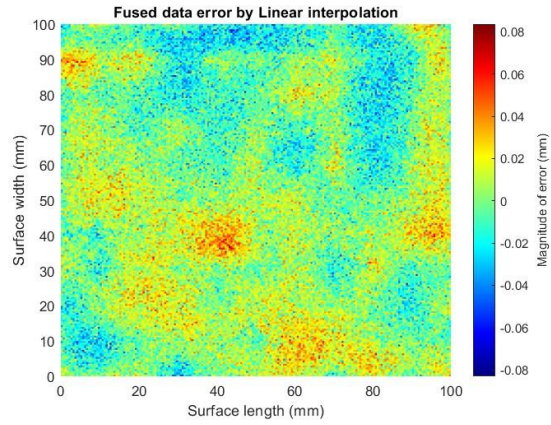


Figure 90. Difference between actual surface and fusion result made by linear interpolation

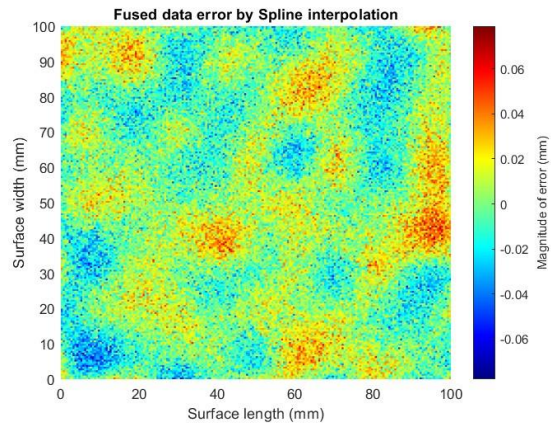


Figure 91. Difference between actual surface and fusion result made by spline interpolation

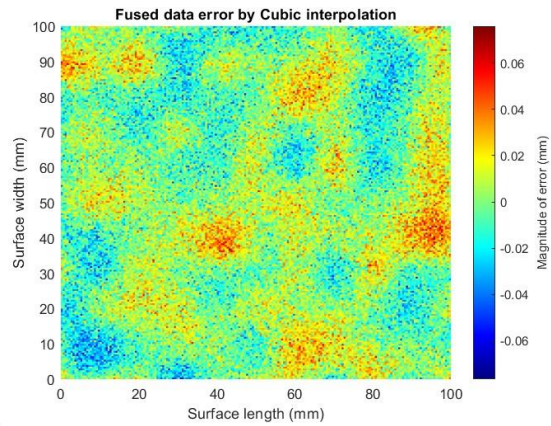


Figure 92. Difference between actual surface and fusion result made by cubic interpolation

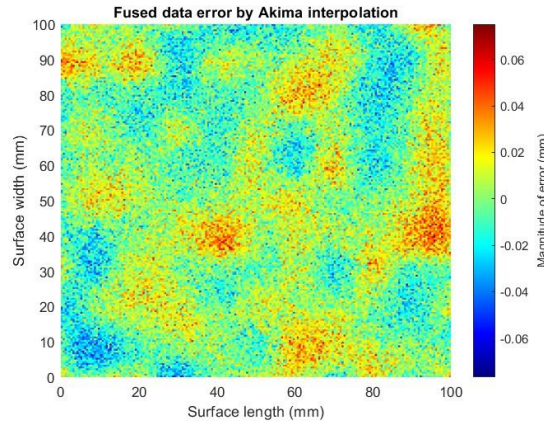


Figure 93. Difference between actual surface and fusion result made by Akima interpolation

According to the results shown above, the fusion result made by linear interpolation had the largest deviation from the actual surface having a 0.16667 mm difference range, 0.0013 mm in difference average, and 0.0188 mm in difference standard deviation. The Spline interpolation showed mediocre results across the measured variables. We got the minimum deviation from the actual surface using the Cubic and Akima interpolation methods with 0.1524 mm and 0.1520 mm difference range, respectively. Similarly, we obtained a difference average of 0.0012 mm and a difference standard deviation of 0.0187 mm in both Cubic and Akima methods. This indicates that Akima is the best interpolation method. Hence, this will be our selected interpolation method for this research moving forward.

## 4.3 2D experiment

### 4.3.1 Data acquisition

In the 2D experiment, we have 2 channels of data inputs which are the CMM that counts for the high-accuracy low-density terminal and the articulate arm laser scanner that represents the low-accuracy high-density dataset.

The CMM data was collected by programming QUINDOS software to control the CMM probe and measure the workpiece topography. One of the criteria to measure the part surface is the routing map of the probe. In the beginning, we decided to have a rectangular-shaped path on the part with serpentine directions. This path was comprised of 100 points which were on a 10 x 10 grid. (Figure 94-95)

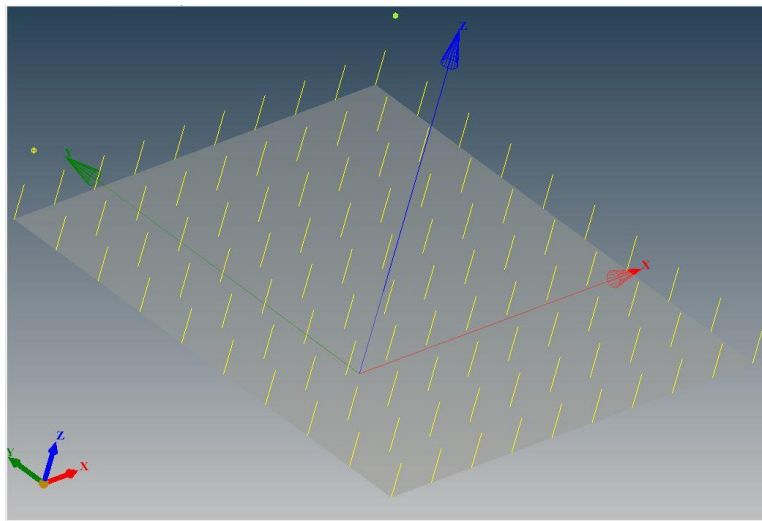
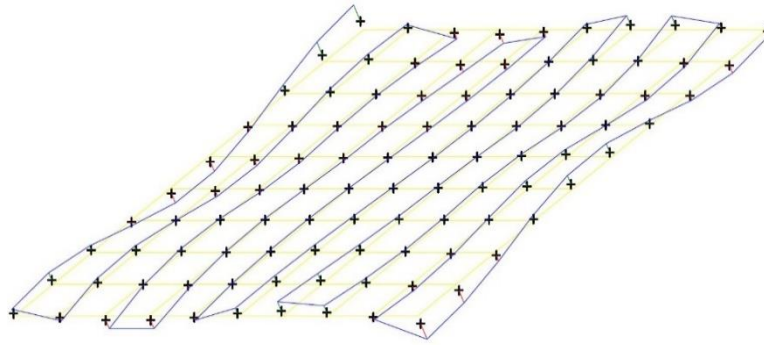


Figure 94. Rectangular probing path for part measurement (100 points)



*Figure 95. Workpiece topography by a rectangular grid (100 points)*

Since the workpiece has a round shape, the rectangular scanning path does not cover all the part edges uniformly and we end up with diagonal edge measurements of the part and this will result in an insufficient measurement of the part.

Hence, to better cover the workpiece, a radial probing path would be ideal. To keep the same distance between all the measurement points, the arc length was used as the basis for distributing the measurement spots. So, with this strategy, we divided the part into 9 radial paths starting at a 5 mm radius and expanded it with a 5 mm step size. Putting 3 points on the inner circle yielded 10.472 mm as the arc length between them. The same arc length was replicated for all the next outer circles. (Figure 96-97)

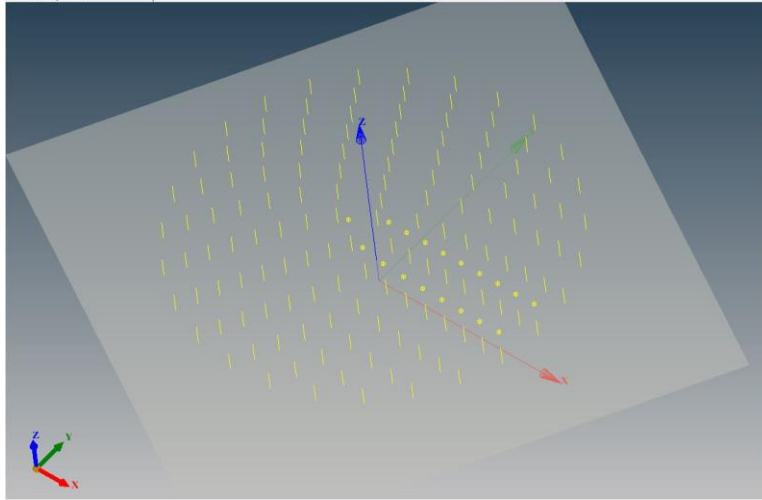


Figure 96. Radial probing path for part measurement (135 points)

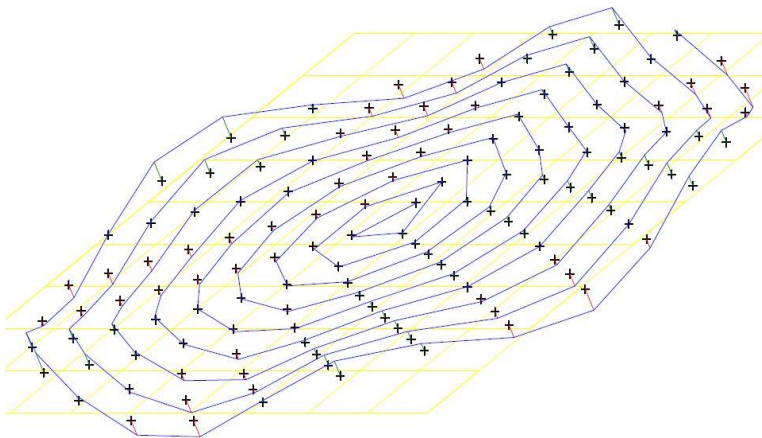


Figure 97. Workpiece topography by a radial grid (135 points)

The same method was implemented for the high-density high-accuracy dataset by CMM to be used as a reference benchmark dataset with 4680 points. In that process, the smallest radius was 1.25 mm, and it was expanded with 1.25 mm step size until it reached 48.75 mm on the outer boundary. For the smallest circle, 6 points were



collected and the arc length between them was 1.309 mm, and this arc length was kept consistent until the last outer circle with 234 points. (Figure 98-99)

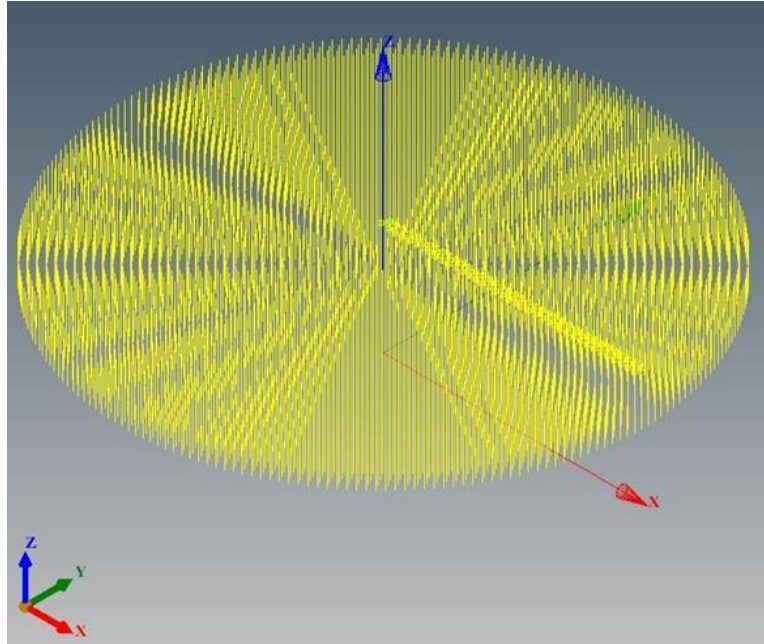


Figure 98. Radial probing path for part measurement (4680 points)

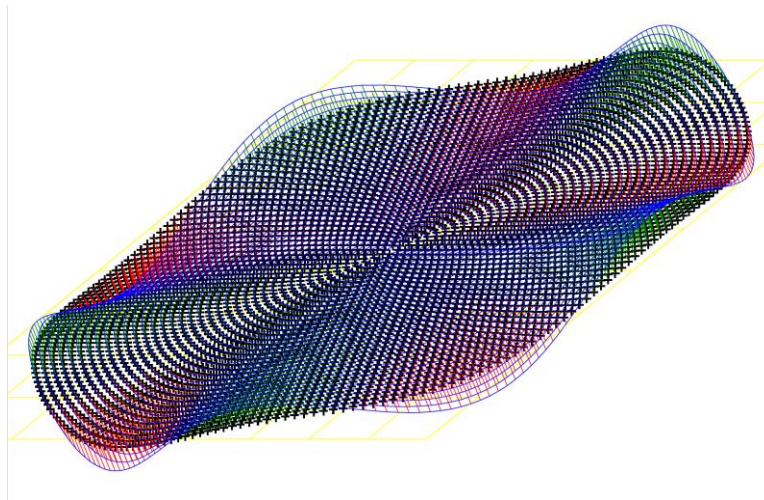


Figure 99. Workpiece topography by a radial grid (4680 points)

#### 4.3.2 Data fusion

After we measured the part with the laser scanner to collect the surface point cloud topography, we trimmed the dataset to cover the surface area. Then we created voxels on the surface to surround the points. Then by taking the average of the Z value of the points within each voxel, we uniformed the surface data density with one point representing each voxel. Considering a threshold for the points per voxel helped us to eliminate the outlier points. The next step in preparing the laser scanner dataset was to create a coordinate system for it in the same way that we built one through the CMM measurement. This resulted in 26,400 points at the end representing the laser scanner high-density, low-accuracy dataset. On the other hand, the 135 CMM points were corrected for stylus height differences on the rotational sine surface area of the part. By these steps, we made two dataset groups from each data channel, and their coordinate systems are aligned with each other. (Figure 100-101)



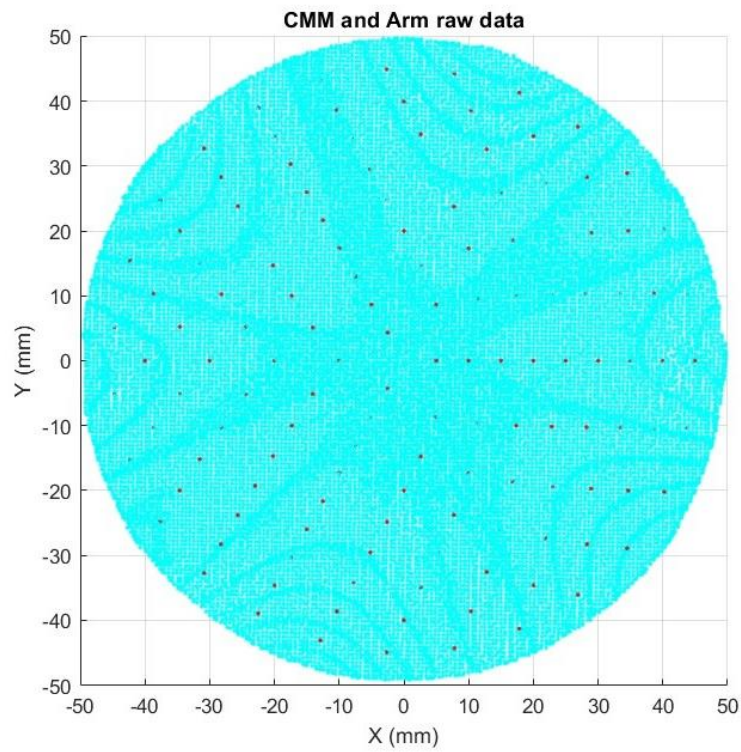


Figure 100. 135 CMM points and 26400 laser scanner points aligned

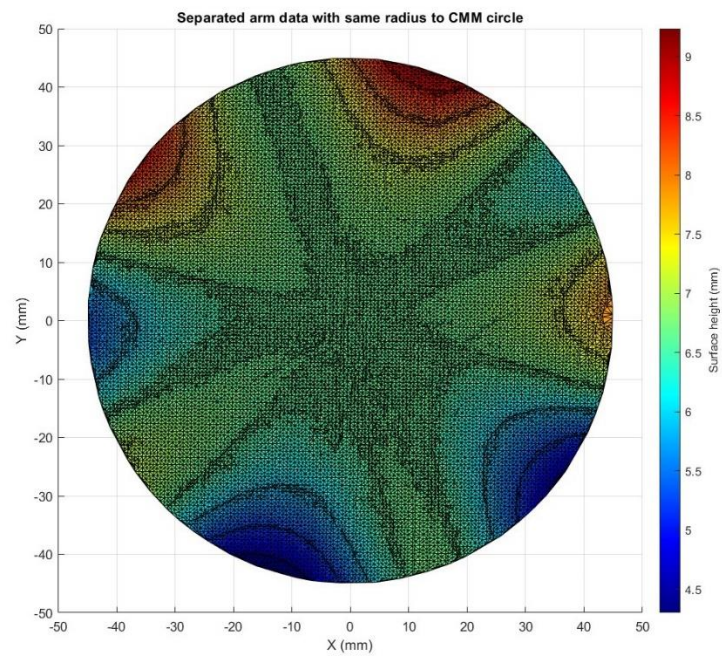


Figure 101. Separated 26400 laser scanner points with the same circumference as the CMM dataset

In the next step, we separated the local defect of the laser scanner dataset (high-density, low-accuracy) by using a Gaussian filter. The high-pass filter separates the surface form and shape, and the low-pass filter separates high-frequency noise from the surface. (Figure 102-103)

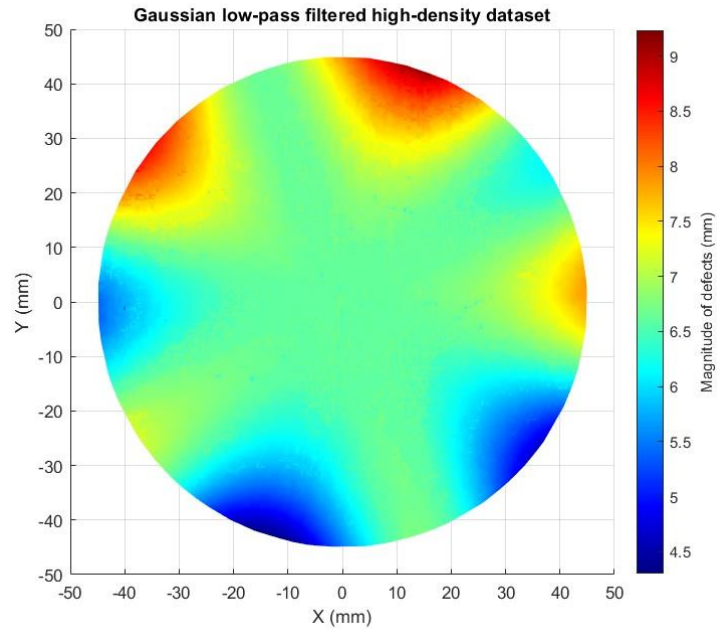
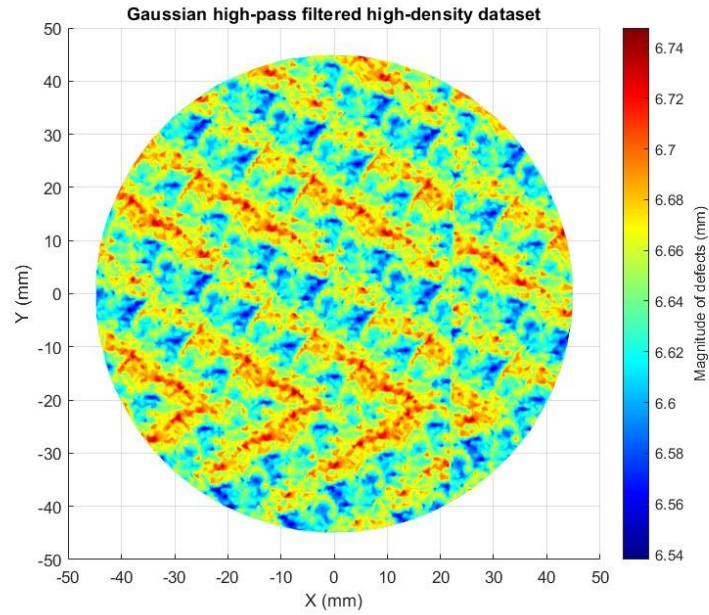


Figure 102. Gaussian low-pass filtered defects on arm dataset



*Figure 103. Gaussian high-pass filtered defects on arm dataset*

By subtracting the raw high-density low-accuracy dataset from the summation of the low-pass and high-pass Gaussian filters, the remainder would be a surface in which its form features and high-frequency noise are removed, and it represents the surface defects. (Figure 104)

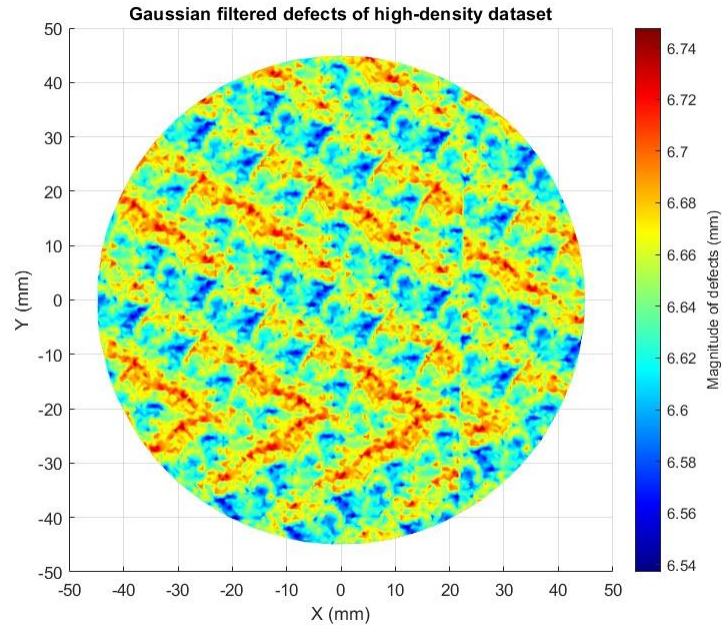


Figure 104. Gaussian-filtered defects from high-density low-accuracy dataset

This Gaussian-filtered dataset retains its data density through this process with 26,400 points. In the next step, to be able to find these defect locations on the CMM dataset, we need to find the corresponding points on the laser scanner dataset. Consequently, the Gaussian-filtered laser scanner dataset should be converted to the 135-point grid to be comparable with the CMM dataset. Hence, on the Gaussian-filtered laser scanner dataset, the nearest neighbor points to their CMM counterpart are separated and create a new dataset. This dataset consists of 135 points representing the defects on the workpiece. (Figure 105)

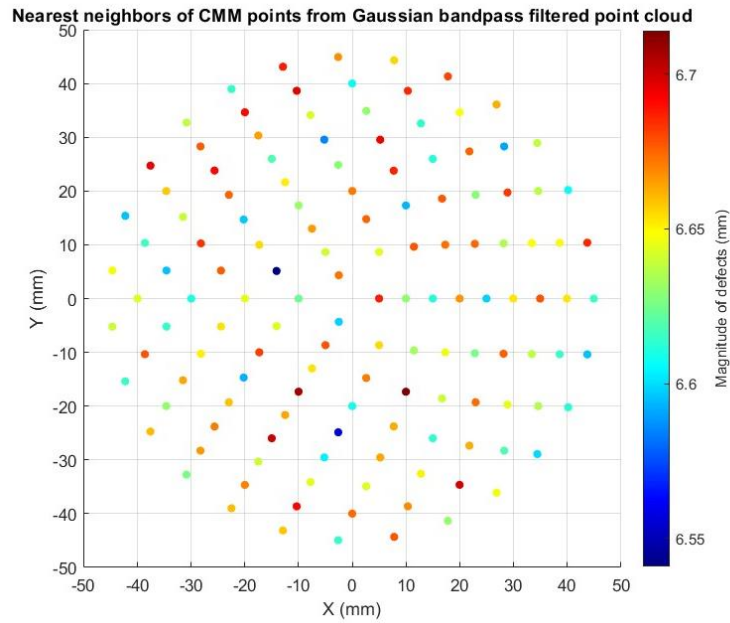


Figure 105. 135 points from Gaussian-filtered high-density dataset that are nearest neighbors to the CMM points

In the next step, the newly generated dataset is subtracted from the CMM dataset to yield a defect-free, low-density high-accuracy result. This dataset contains 135 points. (Figure 106)

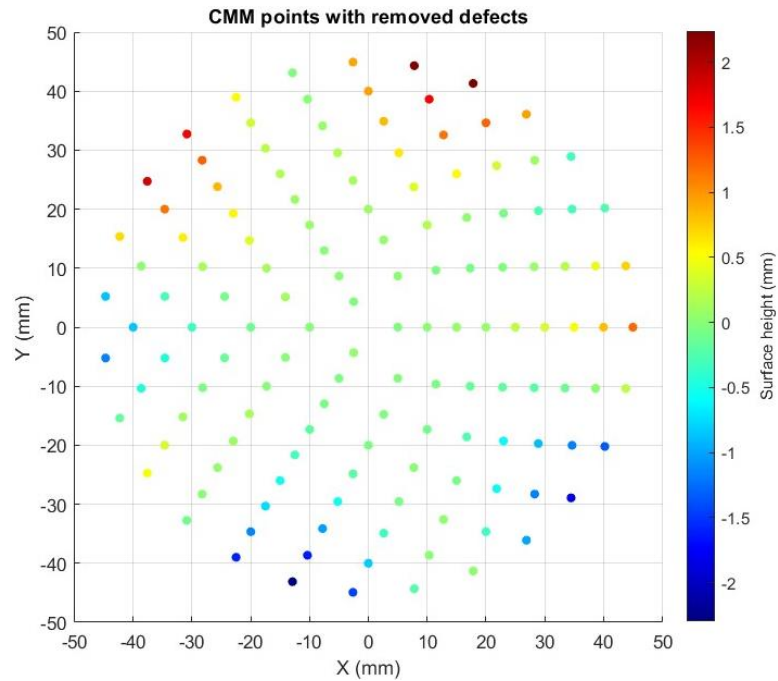
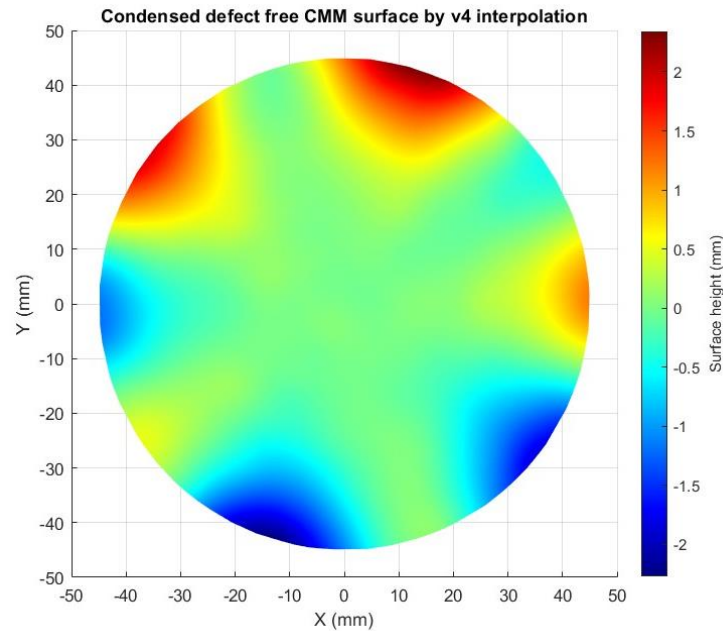


Figure 106. Subtracted defects from the CMM points

After that, we condensed the defect-free CMM dataset to contain 26,400 points as the laser scanner dataset. To condense this dataset from 135 points to 26,400 points we used Biharmonic spline interpolation which imposes the minimum curvature among the available methods. (Figure 107)



*Figure 107. V4 interpolated defect-free CMM dataset*

As the last step, the separated local defects by the Gaussian filter from the laser scanner will be added to the previous step results and will build a dataset that its surface shape is inherited from the low-density, high-accuracy CMM dataset, and its local defects are succeeded from the high-density, low-accuracy laser scanner dataset. (Figure 108)



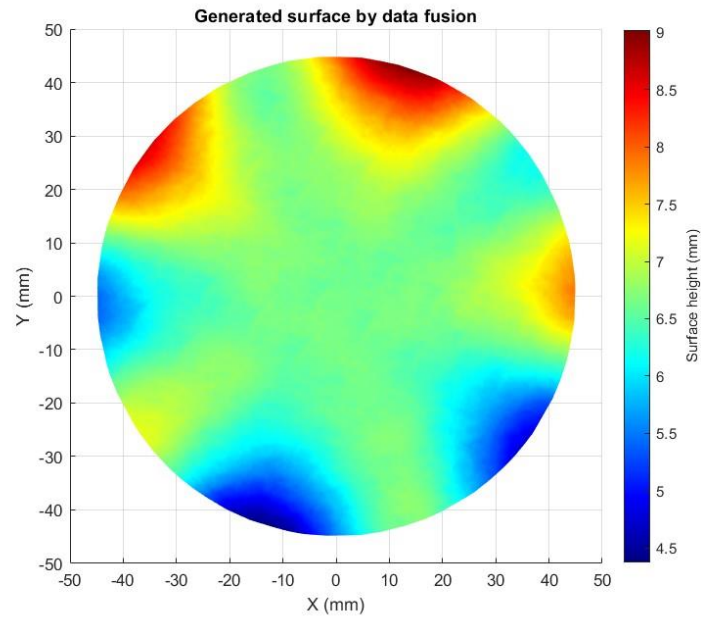


*Figure 108. Data fusion result from the CMM and laser scanner*

#### 4.3.3 Data fusion analysis

The difference between the generated fused data and the raw high-density low-accuracy dataset is plotted in Figure 109-110.



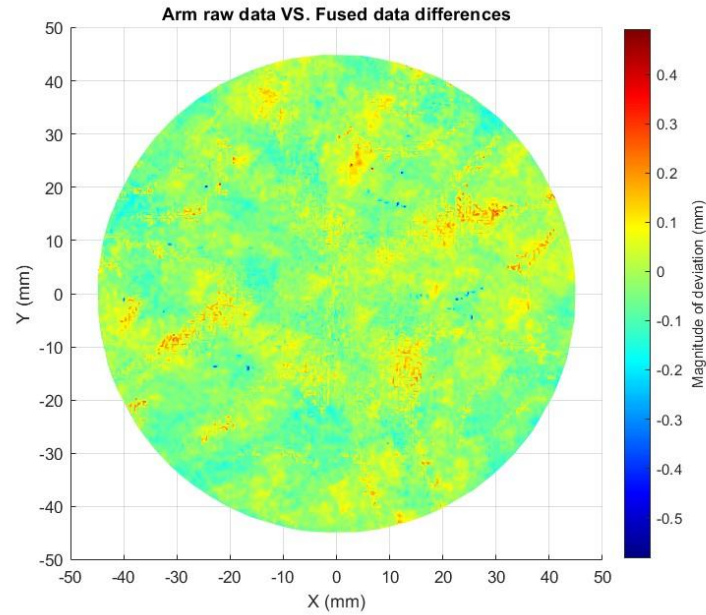


Figure 109.  $\Delta Z$  of High-density low-accuracy vs. generated fused dataset

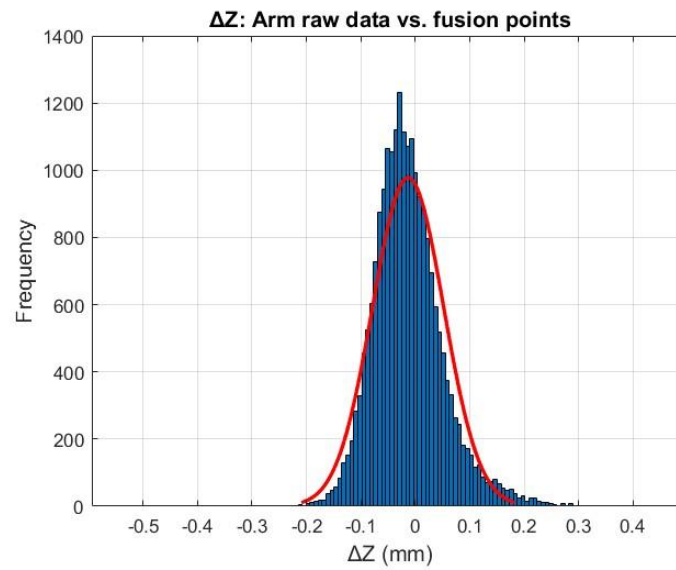


Figure 110.  $\Delta Z$  of High-density low-accuracy vs. generated fused dataset histogram

To evaluate the accuracy of the generated fusion result, the CMM measurement with 4680 points (high-accuracy, high-density) can be used as the reference benchmark

dataset. So, first, we measured the height difference between the 4680 CMM points with the 135 CMM points. With this comparison, we would be able to check the  $\Delta Z$  of the same 135 points from these two datasets. This comparison showed there is a 0.6  $\mu\text{m}$  difference between the average height of the two datasets. Also, the standard deviation of the difference between them was 0.6  $\mu\text{m}$  as well. This is a very negligible error between the two measurements showing the precision and repeatability of the CMM tool. Aligning the two datasets on the same plot would be as in Figure 111 and Figure 112.

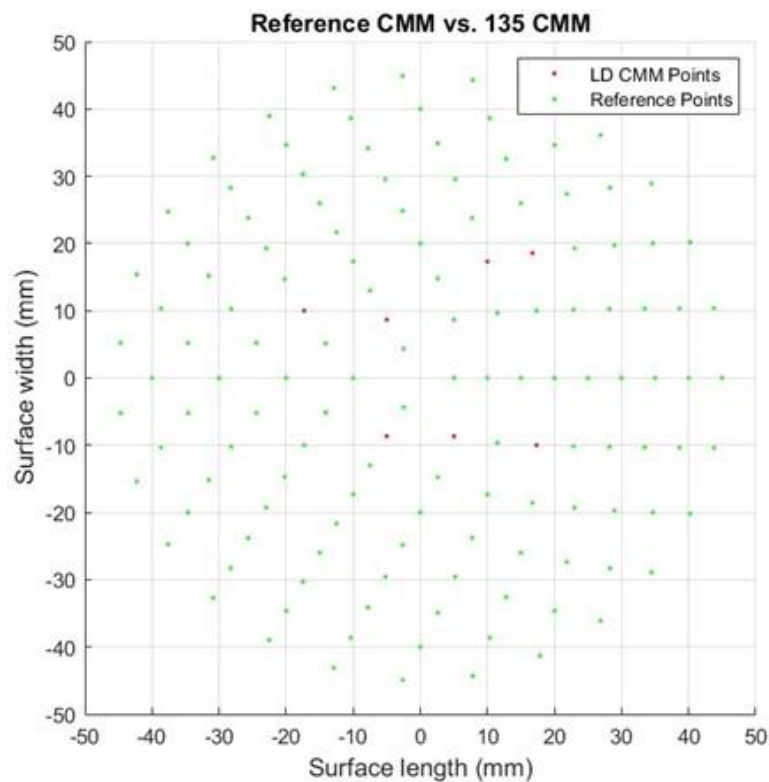


Figure 111. 135 CMM points vs. nearest neighbor points from 4680 reference CMM dataset

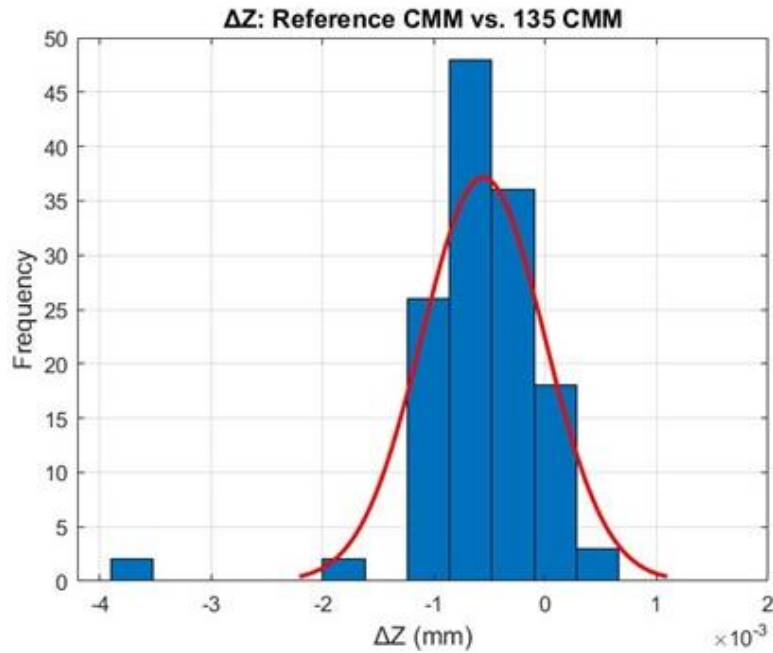


Figure 112.  $\Delta Z$  histogram of the reference 4680 and 135 CMM points datasets

The same comparison was made between the 4680 reference benchmark CMM points and the nearest counterpart neighbors from the 26400-point laser scanner dataset. This comparison showed the  $\Delta Z$  has an average of 0.0206 mm and a standard deviation of 0.0522 mm between the two 4680 points groups as shown in Figure 113-114.

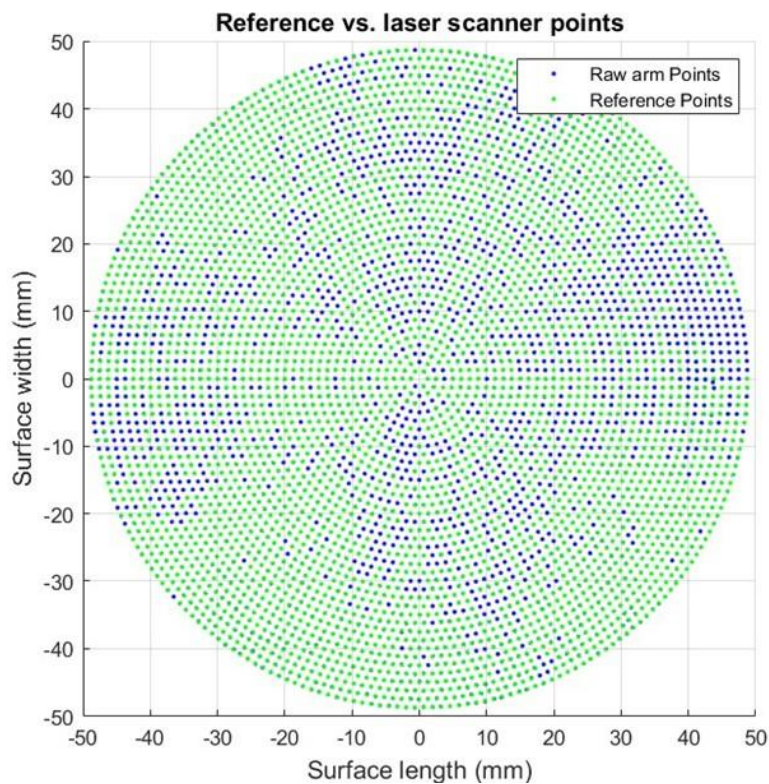


Figure 113. Reference 4680 CMM points vs. their nearest neighbors from the laser scanner dataset

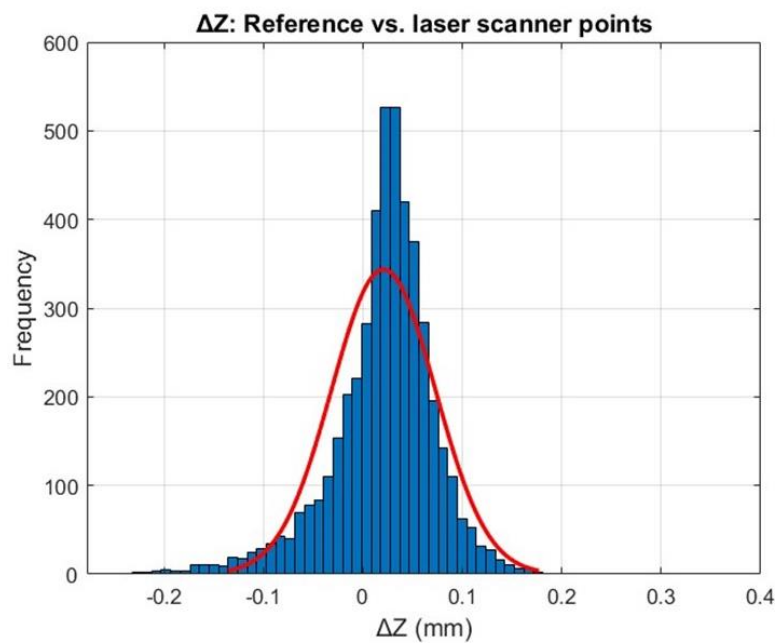


Figure 114.  $\Delta Z$  histogram of reference 4680 points and their laser scanner nearest neighbors

Finally, the 4680 points CMM benchmark dataset is compared with the generated data fusion result. So, 4680 points from the fusion result which were nearest neighbors to the reference CMM points were separated for this comparison. In this plot, the fusion points, the reference points, and the 135 CMM points are illustrated. This comparison showed the  $\Delta Z$  has an average of 0.0049 mm and a standard deviation of 0.0739 mm between the two point groups. (Figure 115-116)

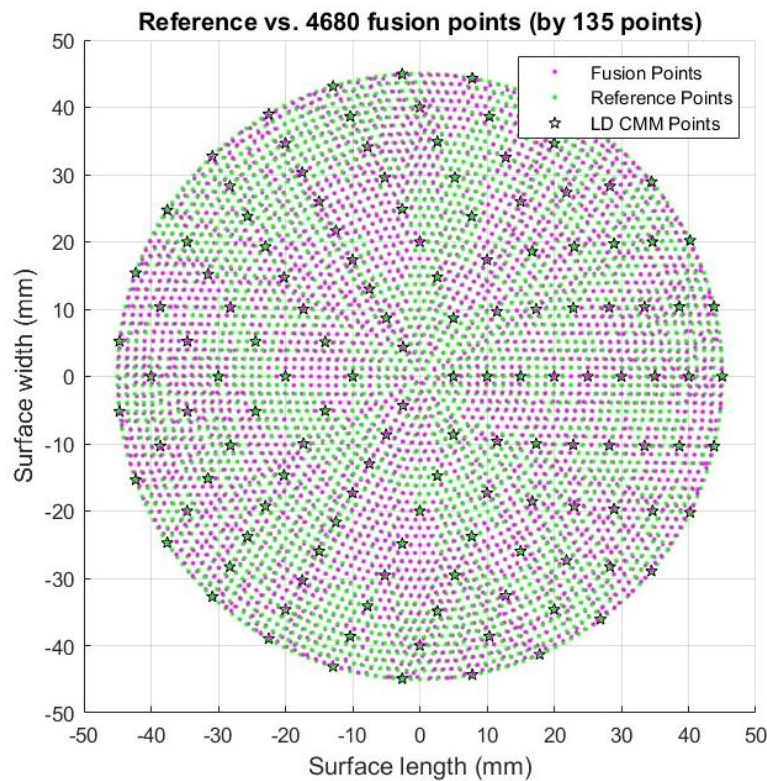


Figure 115. Reference 4680 CMM points vs. their nearest neighbor fusion points (135 CMM points)

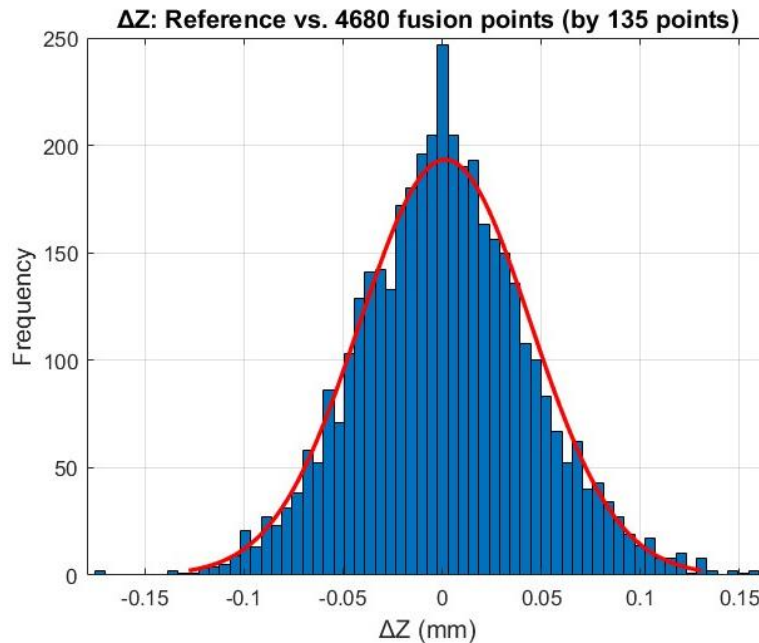


Figure 116.  $\Delta Z$  histogram of the 4680 reference CMM points and their nearest neighbor fusion points (135 CMM points)

On the next assessment, we are curious to see how the CMM points would contribute to the fusion accuracy by decreasing their numbers. The objective of reducing the CMM points is to save time on extensive CMM measurements. Hence, we will compare the fusion results which are generated by different quantities of CMM points with the reference benchmark CMM dataset to better understand the fusion tolerance based on the CMM data density. We will review the data fusion results made by 75, 45, and 15 CMM points accordingly. The CMM points layout for each of these compositions is as in Figure 117-119.

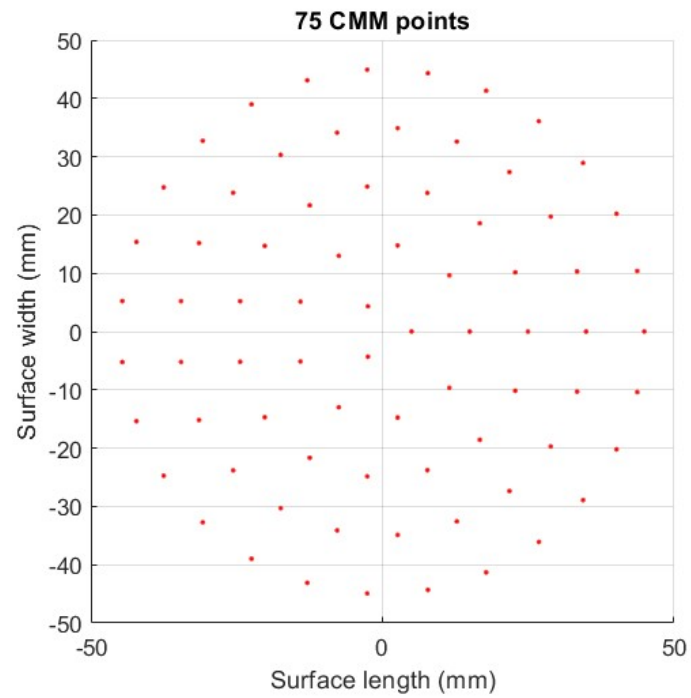


Figure 117. 75 CMM points serve as a low-density, high-accuracy dataset

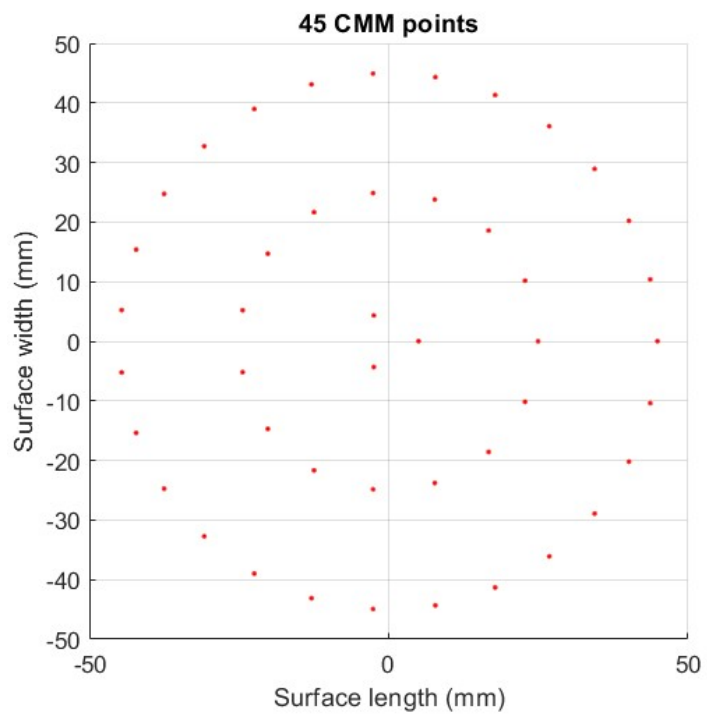


Figure 118. 45 CMM points serve as low-density, high-accuracy dataset



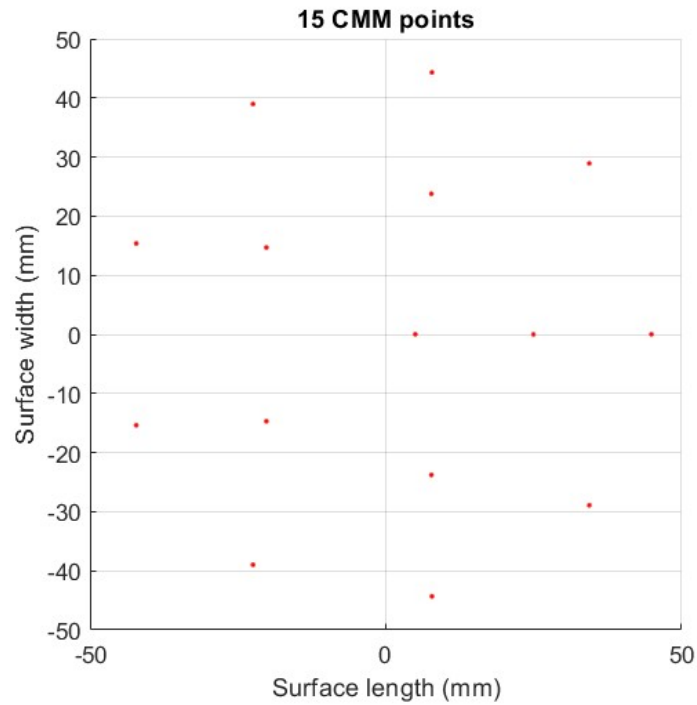


Figure 119. 15 CMM points serve as low-density, high-accuracy dataset

By generating fusion results with each of these low-density, high-accuracy datasets, we can compare them with the reference CMM dataset (4680 points) to evaluate the fusion efficiency and CMM dataset contribution to the final result.

First, the fusion result made by 75 CMM points showed 0.0065 mm in average  $\Delta Z$  and 0.0836mm in  $\Delta Z$  standard deviation between the reference CMM dataset and the 4680 nearest counterpart points from the fusion result based on the 75 CMM points. (Figure 120-121)



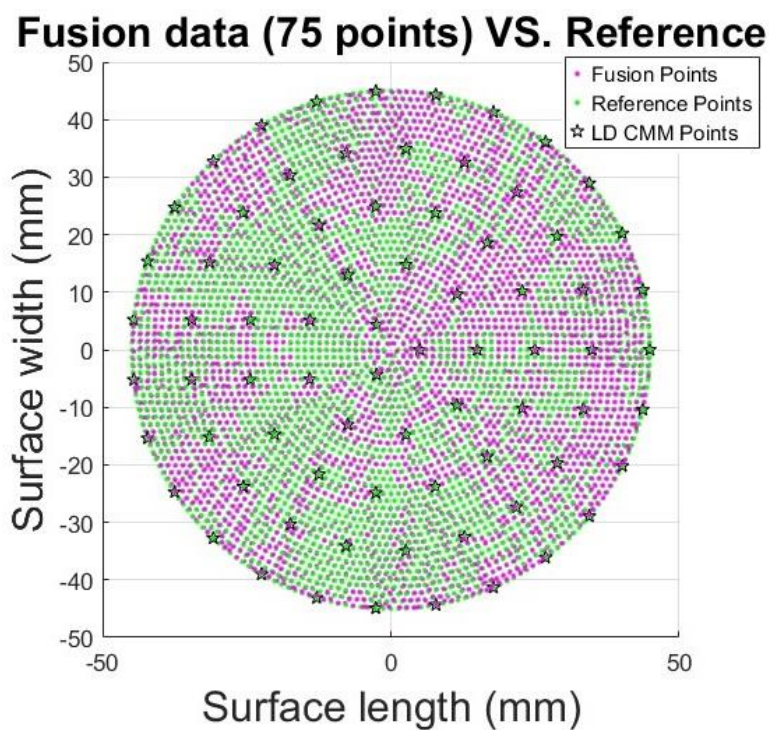


Figure 120. Reference 4680 CMM points vs. their nearest neighbor fusion points (75 CMM points)

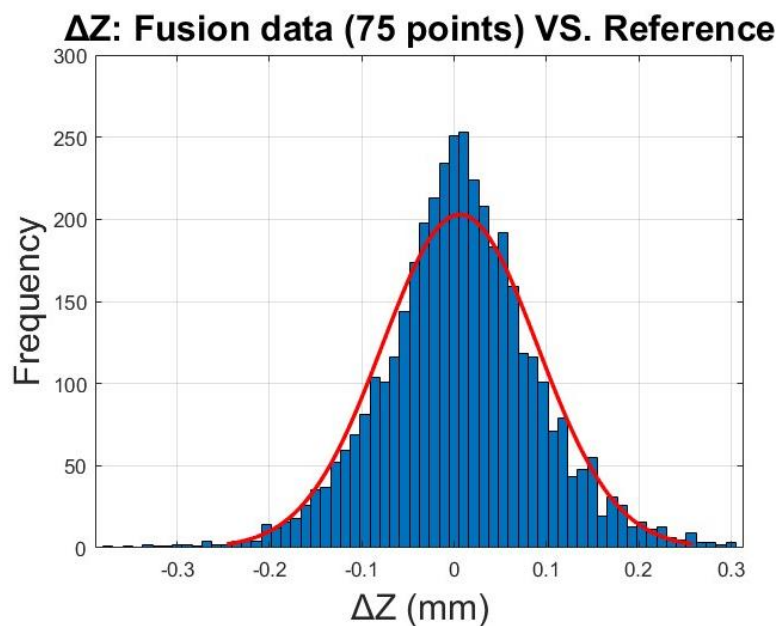


Figure 121.  $\Delta Z$  histogram of 4680 reference CMM points and their nearest neighbor fusion points (75 CMM points)

Next, the fusion result made by 45 CMM points showed -0.0259 mm in average  $\Delta Z$  and 0.0942 mm in  $\Delta Z$  standard deviation between the reference CMM dataset and the 4680 nearest counterpart points from the fusion result based on the 45 CMM points.

(Figure 122-123)

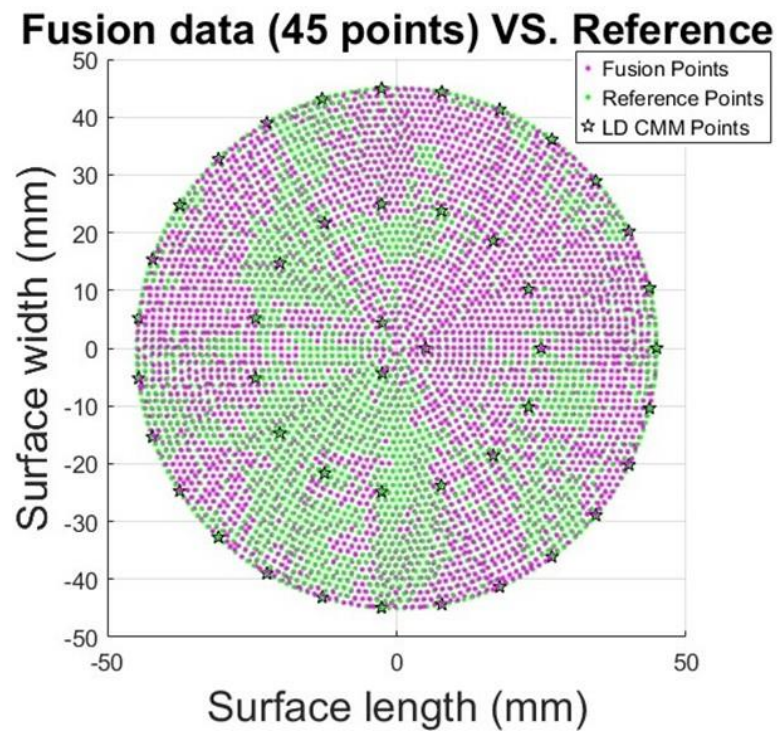


Figure 122. Reference 4680 CMM points vs. their nearest neighbor fusion points (45 CMM points)

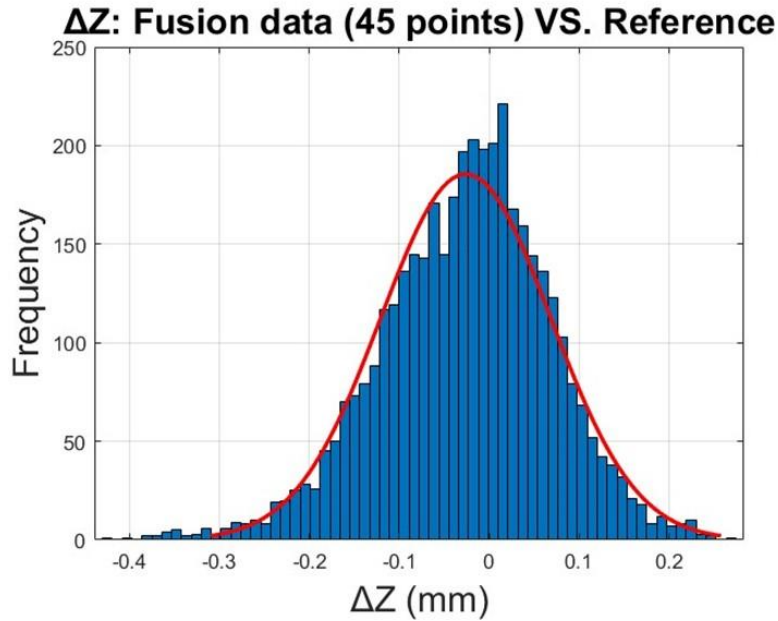


Figure 123.  $\Delta Z$  histogram of 4680 reference CMM points and their nearest neighbor fusion points (45 CMM points)

Lastly, the fusion result made by 15 CMM points showed -0.1116 mm in average  $\Delta Z$  and 0.4256 mm in  $\Delta Z$  standard deviation between the reference CMM dataset and the 4680 nearest counterpart points from the fusion result based on the 15 CMM points. (Figure 124)

In Figure 125, the real data in the histogram indicates the Leptokurtic distribution compared to the red Gaussian line, which is a normal distribution, and has a smaller standard deviation. This indicates that our data is more concentrated around the mean which attributes higher accuracy.

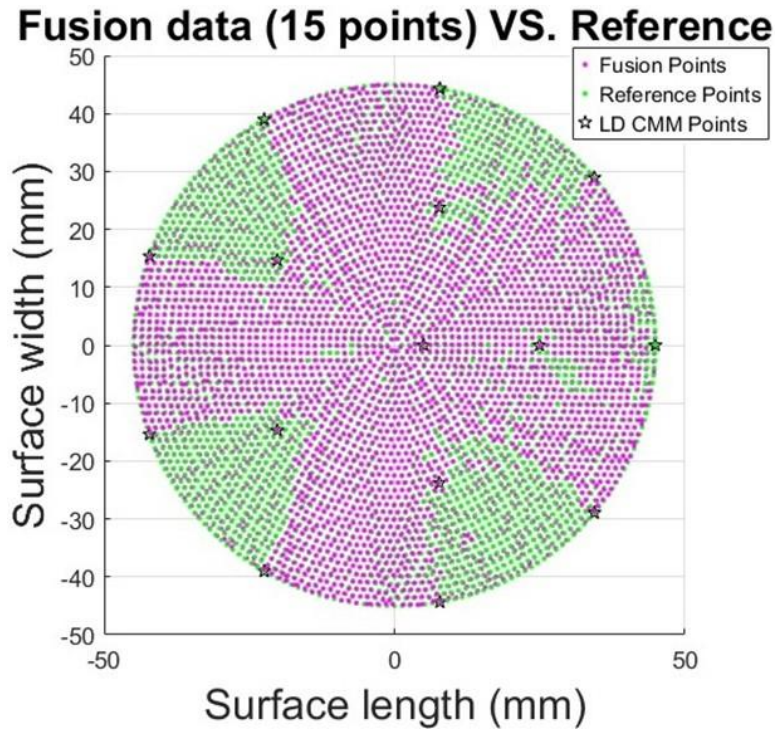


Figure 124. Reference 4680 CMM points vs. their nearest neighbor fusion points (15 CMM points)

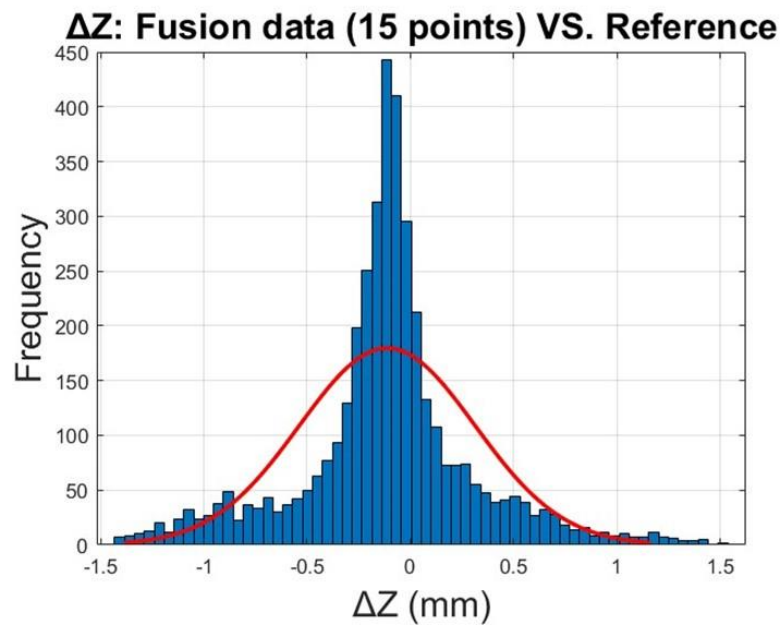


Figure 125.  $\Delta Z$  histogram of 4680 reference CMM points and their nearest neighbor fusion points (15 CMM points)

In the end, by comparing all the fusion method results with the reference benchmark CMM, we observe that fusion with 135 points has 76%, and fusion with 75 points has 68% improvement in mean  $\Delta Z$  compared to the raw laser scanner dataset. (Figure 126)

		Raw CMM 135 points	Raw laser scanner 26400 points	Fusion by 135 CMM points	Fusion by 75 CMM points	Fusion by 45 CMM points	Fusion by 15 CMM points
Reference benchmark CMM (4680 points) vs.	Mean $\Delta Z$ (mm)	-0.0006	0.0206	0.0049	0.0065	-0.0259	-0.1116
	STD $\Delta Z$ (mm)	0.0006	0.0522	0.0739	0.0836	0.0942	0.4256

Figure 126. Benchmark CMM points vs. raw and fusion datasets

#### 4.4 3D experiment

By measuring the 3D cylindrical workpiece with CMM and 3D scanner, the two datasets were aligned as the first step. This alignment is based on the minimum RMS between the distances of the corresponding points. As a result, the CMM and 3D scanner point clouds are defined based on the uniform coordinate system. (Figure 127)

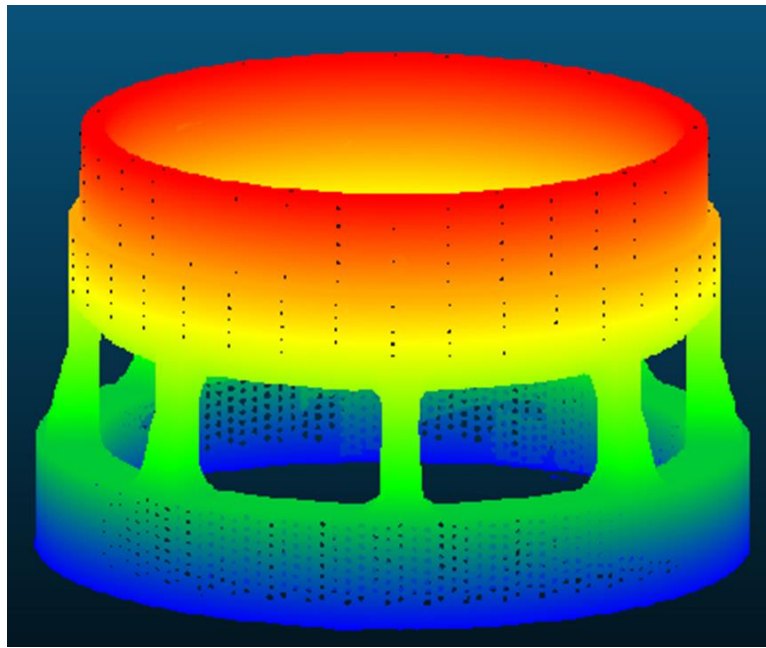


*Figure 127. CMM and 3D scanner point cloud alignment*

Based on the new coordinate system each point cloud is redefined and illustrated separately as in Figure 128 and Figure 129.



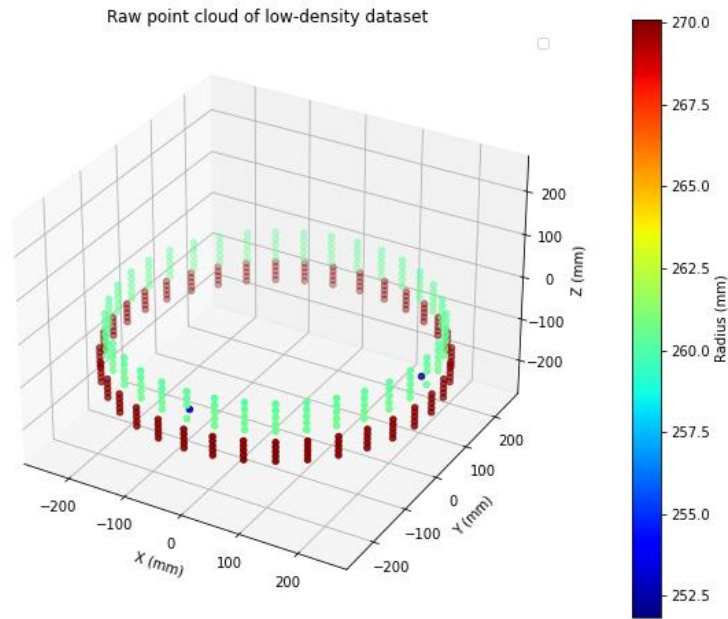


Figure 128. Raw CMM point cloud

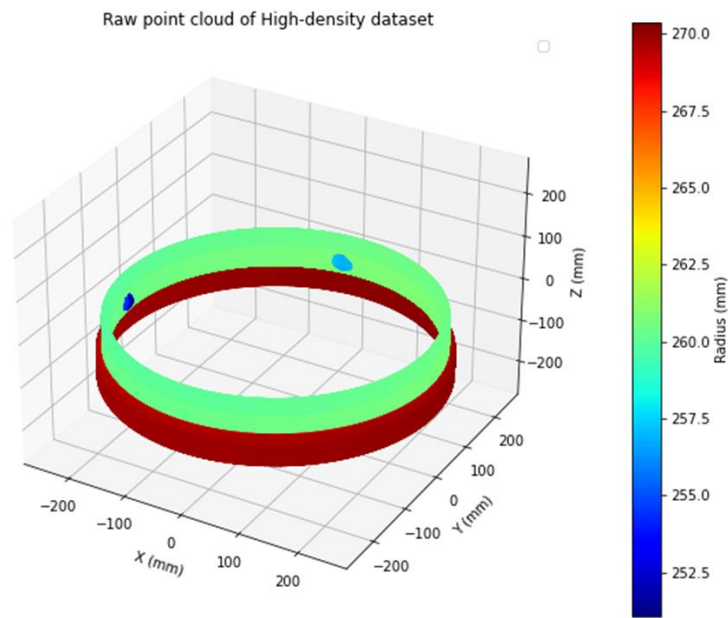


Figure 129. Raw 3D scanner point cloud

In the next step, the Gaussian filters extract the defects from the cylinder surface as in Figure 130.

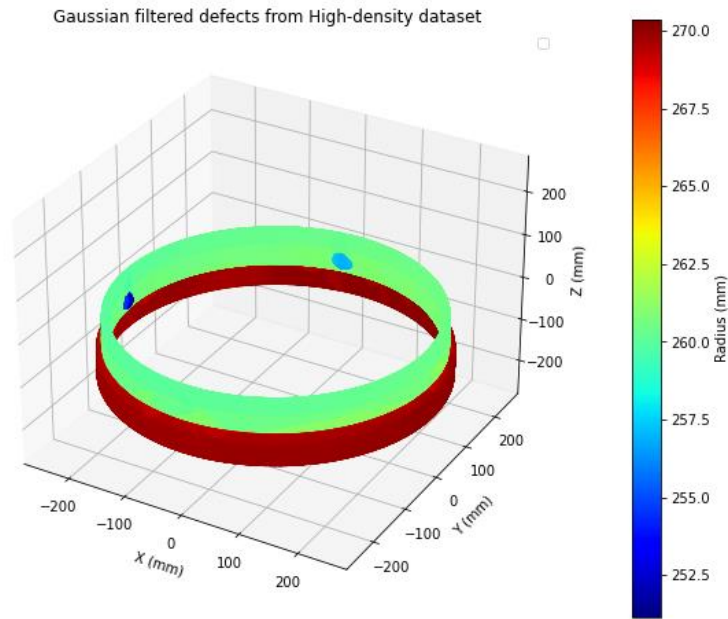


Figure 130. Gaussian-filtered defects from high-density dataset

Next, the nearest neighbor points to the CMM dataset are selected from the Gaussian-filtered defect dataset. This was achieved by using the kdtree function. Figure 131 is the histogram of the distances between the CMM points and their corresponding nearest neighbors.

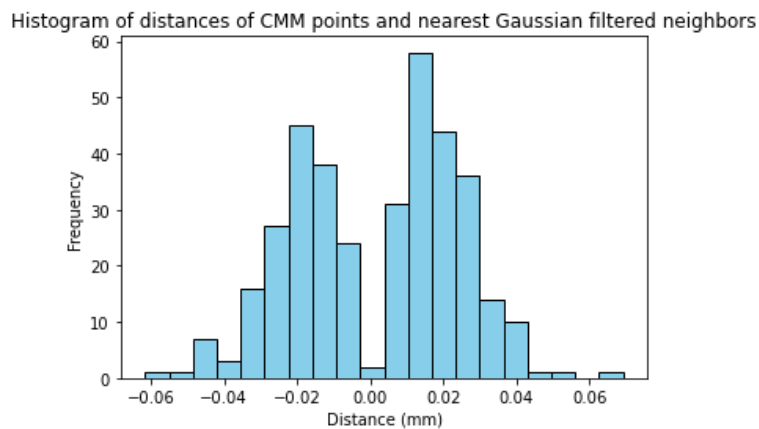


Figure 131. Distances between the CMM points and their corresponding nearest neighbors



The average distance shown above is 0.0018 mm with a standard deviation of 0.0222 mm.

After that, the radius of the CMM nearest neighbor points from the Gaussian-filtered dataset is subtracted from the radius value of the raw CMM points. This will result in a defect-free surface. (Figure 132)

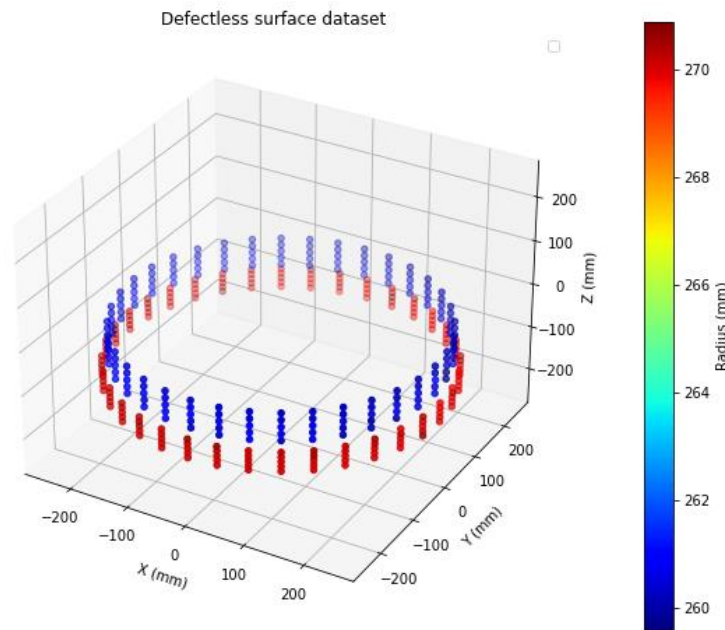


Figure 132. The defect-free surface of the cylinder

Consequently, these sparse points are interpolated to generate a point cloud with the same density as the high-density dataset. There are a couple of different interpolation methods including linear, nearest, cubic, and thin plate radial basis function (RBF). Interpolating the surface with the mentioned techniques shows the nearest interpolation method generates the best result for the 3D part since it is continuous near the boundary of the surface and does not generate NaN values by query of the points outside the convex hull of the sample data. (Figure 133)

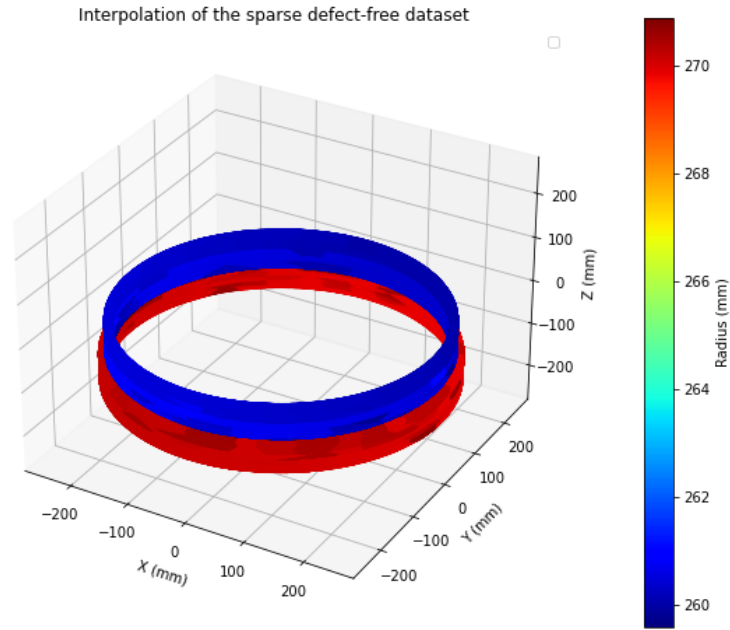


Figure 133. Linear interpolation of the defect-free dataset

Finally, by adding the extracted defects from the Gaussian filters to the interpolated defect-free surface, the fused data is generated. (Figure 134)

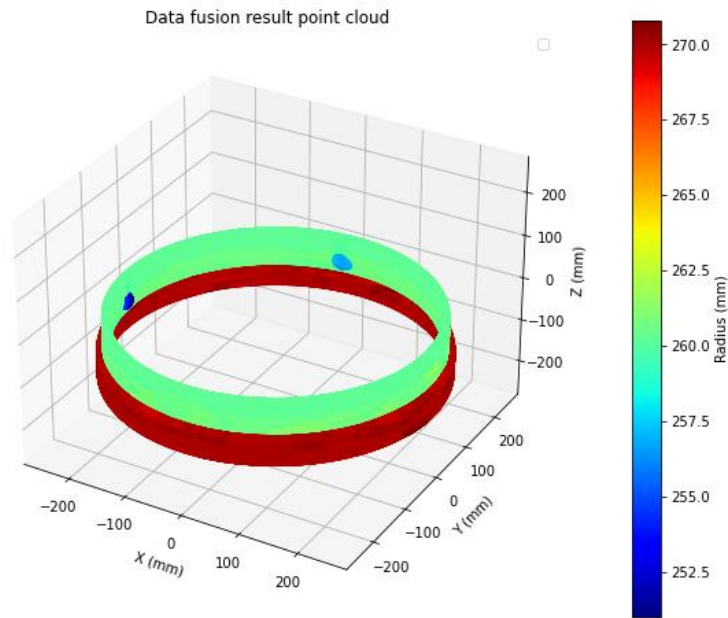


Figure 134. The point cloud of the data fusion result

The histogram of the distances between the fusion dataset and the raw high-density dataset with an average of  $-0.0001$  mm and a standard deviation of  $0.2758$  mm is shown in Figure 135.

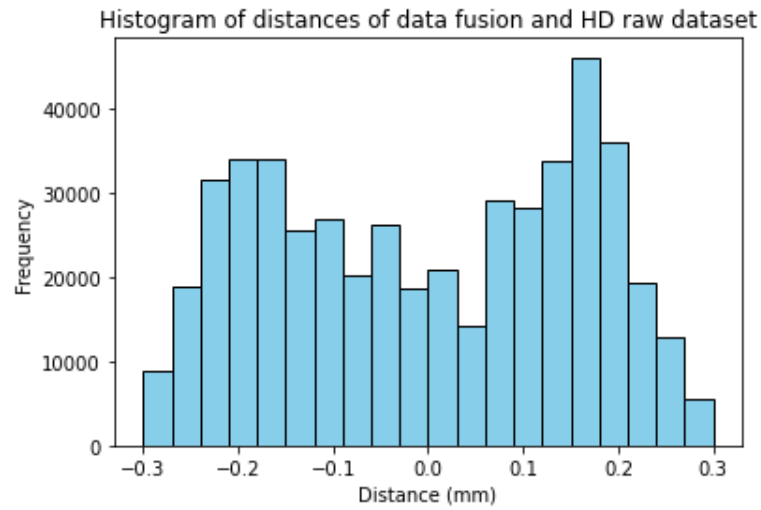


Figure 135. Histogram of the distances between data fusion and raw high-density dataset

## 5 Discussion

In this work, we used two tools (CMM and laser scanner) to collect the surface topography of a workpiece and then by combining these two datasets, try to achieve a higher accuracy. This goal was obtained for fusion made by 135 and 75 CMM points as the low-density, high-accuracy dataset channel. It is obvious that the more CMM points we can have, the more accurate results we can obtain. But there is a tradeoff between CMM points numbers, and the amount of time required to generate the final measurement result. Hence, depending on the industry type and the level of necessary precision, the data accuracy and density of each channel should be determined accordingly.

CMM can measure the workpiece either by probing the stylus on the predefined coordinates and measuring the geometry or it can scan the surface by continuously capturing the surface geometry. The scanning mode might seem to be faster and denser, but it does not have the same accuracy as the probing mode since the probe sensor is influenced by unexpected height changes while moving along the surface. Thus, it is best to use the probing mode for the high-accuracy channel dataset.

This project helped to strategize a method to efficiently integrate the two datasets without sacrificing the important surface feature information. It is important to understand the advantages and disadvantages of each measuring tool before starting to measure any workpiece. With this suggested method in this work, the user can decide to combine measurement tools that can cover each other's flaws and generate a robust result with high accuracy and high density.

Different parameters can contribute to the uncertainty of the results. These parameters can be environmental conditions including lab temperature, humidity, air pressure, vibration, and magnetic fields. Other parameters are measurement equipment's calibration, measurement setup strategy, software and calculation accuracy, operator skill level and ability to reproduce the results, workpiece geometric stability and rigidity, experiment procedure, and physical constraints.

It is important to note that the data fusion in 2D may be time-consuming to set up preliminary measurements and particularly sensitive to the inputs from the high-accuracy channel. The reason behind this statement is that the high-accuracy channel is construed to be our reference dataset in the fusion process. Therefore, any error or bias from this channel can easily deviate the fusion result from the true value. So, the operator's attention to the intricacies and specifications of the tool and the robustness of the data integration techniques plays a crucial role in the accuracy of the final measurement.

When the 45 and 15 CMM points were used for the fusion process, they did not meet the raw laser scanner mean  $\Delta Z$  value compared to the 4680 benchmark CMM points. So, it is important to find the proper number of CMM points that can positively impact the fusion result accuracy.

We expanded this research to 3-dimensional space and measured a steam turbine exhaust muffler by CMM and 3D ATOS GOM scanner. By delineating a similar approach as the 2D part, we measured the surface with each one of the tools and proceeded with the data fusion steps. The coordinate systems alignment must be performed accurately to prevent imposing systematic errors on the datasets. By

converting the Cartesian coordinate system to the cylindrical coordinate system, mapping the perimeter features of the workpiece to the surface geometry became feasible. To extract the surface defects by using the Gaussian filter, it is important to use proper sigma values to avoid over-correcting the surface by eliminating important surface features.

This method proved to be an efficient model to fuse datasets obtained by different terminals to both speed up the measurement process and enhance accuracy. The distances between the fused datasets and the high-density low-accuracy dataset with an average of 0.1  $\mu\text{m}$  demonstrate the bias-free methodology and the small range and standard deviations prove the accuracy and precision of the results. This technique can be scaled up to larger parts and point clouds as well.

## 6 Conclusion

This research objective was to find a way to integrate the measurement data generated from two separate resources to increase the measurement quality. This improvement could be obtained either by higher accuracy, data density, or data acquisition speed. First, we elaborated the problem statement by simplifying the model in 1D space. Then we expanded it to a 2D space model and applied it to the 2D experiment part. Lastly, we expanded the model to compute data fusion on a 3D part and evaluated the model performance on a cylindrical workpiece. This data was generated by two measurement tools with specific features. First, the CMM, which was our higher accuracy but slower in measurement channel, and the second tool was the ATOS GOM 3D scanner which was much faster in obtaining surface topography but less accurate compared to the CMM.

One of the criteria to make fusion possible is to align the two dataset's coordinate systems so the points on each one can correspond to the other. After so, by processing the data through various steps, these two datasets were integrated, and a dataset that inherited advantages from both was constructed. The generated fusion result is a high-accuracy high-density point cloud. By comparing the fusion result with different compositions of the CMM and 3D scanner data, the small bias, high accuracy, and precision can qualify this method.

## References

1. Weckenmann, A., et al., *Multisensor data fusion in dimensional metrology*. CIRP annals, 2009. **58**(2): p. 701-721.
2. Abackerli, A., B. Butler, and M. Cox, *Application of data fusion techniques to thermometry data*. 1999.
3. Beyerer, J., *Fusion heterogener Informationen: Essay*. 2005.
4. Boudjemaa, R. and A. Forbes, *Parameter estimation methods in data fusion*. 2004.
5. Liu, J., et al., *Urban big data fusion based on deep learning: An overview*. Information Fusion, 2020. **53**: p. 123-133.
6. Treinish, L.A., *Visual data fusion for applications of high-resolution numerical weather prediction*. 2000: IEEE.
7. Lee, P., et al., *A peer-to-peer collaboration framework for multi-sensor data fusion*. Journal of network and computer applications, 2012. **35**(3): p. 1052-1066.
8. Chou, K.C., A.S. Willsky, and A. Benveniste, *Multiscale recursive estimation, data fusion, and regularization*. IEEE transactions on Automatic Control, 1994. **39**(3): p. 464-478.
9. Clark, J.J. and A.L. Yuille, *Data fusion for sensory information processing systems*. Vol. 105. 2013: Springer Science & Business Media.
10. Mitchell, J.P., et al. *Sensor fusion of laser trackers for use in large-scale precision metrology*. in *Intelligent Manufacturing*. 2004. SPIE.
11. Thomopoulos, S.C., *Sensor integration and data fusion*. Journal of Robotic Systems, 1990. **7**(3): p. 337-372.
12. Hossein-Nejad, Z., H. Agahi, and A. Mahmoodzadeh, *Image matching based on the adaptive redundant keypoint elimination method in the SIFT algorithm*. Pattern Analysis and Applications, 2021. **24**: p. 669-683.
13. Fu, S., et al., *A non-contact measuring system for in-situ surface characterization based on laser confocal microscopy*. Sensors, 2018. **18**(8): p. 2657.
14. Brown, M. and D.G. Lowe, *Automatic panoramic image stitching using invariant features*. International journal of computer vision, 2007. **74**: p. 59-73.
15. Esteban, J., et al., *A review of data fusion models and architectures: towards engineering guidelines*. Neural Computing & Applications, 2005. **14**: p. 273-281.
16. Durrant-Whyte, H.F., *Sensor models and multisensor integration*. The international journal of robotics research, 1988. **7**(6): p. 97-113.
17. Puente León, F., *Komplementäre Bildfusion zur Inspektion technischer Oberflächen (Complementary Image Fusion for Inspection of Technical Surfaces)*. 2002.
18. Müller, M., *Szeneninterpretation unter Verwendung multimodaler Sensorik und Salienzmaßen*. 2022: KIT Scientific Publishing.
19. Pallauf, J. and F. Puente León, *Modellgestützte Objektverfolgung für verteilte autonome Systeme*. tm-Technisches Messen, 2016. **83**(2): p. 85-95.
20. Birch, K. and M. Downs, *An updated Edlén equation for the refractive index of air*. Metrologia, 1993. **30**(3): p. 155.
21. Seeger, S. and X. Laboureux, *Feature extraction and registration: An overview*. Principles of 3D image analysis and synthesis, 2002: p. 153-166.



22. Marinello, F., et al., *Increase of maximum detectable slope with optical profilers, through controlled tilting and image processing*. Measurement Science and Technology, 2007. **18**(2): p. 384.
23. Dasarathy, B.V., *Sensor fusion potential exploitation-innovative architectures and illustrative applications*. Proceedings of the IEEE, 1997. **85**(1): p. 24-38.
24. Beyerer, J., F. Puente León, and K.-D. Sommer, *Informationsfusion in der Mess- und Sensortechnik*. 2006: KIT Scientific Publishing.
25. Klein, L.A., *Sensor and data fusion: a tool for information assessment and decision making*. Vol. 138. 2004: SPIE press.
26. Zitova, B. and J. Flusser, *Image registration methods: a survey*. Image and vision computing, 2003. **21**(11): p. 977-1000.
27. Schön, N. and G. Häusler. *Automatic coarse registration of 3D surfaces*. in *Vision, modeling, and visualization*. 2005. Citeseer.
28. Schwenke, H., et al., *Optical methods for dimensional metrology in production engineering*. CIRP Annals, 2002. **51**(2): p. 685-699.
29. Wagner, C., *Informationstheoretische Grenzen optischer 3D-Sensoren*. 2003, Friedrich-Alexander-Universität Erlangen-Nürnberg (FAU).
30. KEFERSTEIN, C.P., D. HONEGGER, and M. RITTER, *Marktanalyse Optischer 1D-, 2D-, 3D-Sensoren und Optischer KMG: Vielfalt erschwert die Auswahl*. QZ. Qualität und Zuverlässigkeit, 2006. **51**(8): p. 40-41.
31. Savio, E., L. De Chiffre, and R. Schmitt, *Metrology of freeform shaped parts*. CIRP annals, 2007. **56**(2): p. 810-835.
32. Weckenmann, A., P. Kraemer, and J. Hoffmann. *Manufacturing metrology—state of the art and prospects*. in *Proc. ISMQC*. 2007.
33. Horbach, J., *Verfahren zur optischen 3D-Vermessung spiegelnder Oberflächen*. 2007.
34. Schmitt, R., P. Hafner, and S. Pollmanns, *Kompensation von Metallartefakten in tomografischen Aufnahmen mittels Bilddatenfusion*. 2008: na.
35. Weckenmann, A., et al., *Probing systems in dimensional metrology*. CIRP annals, 2004. **53**(2): p. 657-684.
36. Bartscher, M., et al., *Enhancement and proof of accuracy of industrial computed tomography (CT) measurements*. CIRP annals, 2007. **56**(1): p. 495-498.
37. Hoffmann, J., A. Schuler, and A. Weckenmann, *Construction and evaluation of a traceable metrological scanning tunnelling microscope*. Measurement, 2009. **42**(9): p. 1324-1329.
38. Brassard, M., et al. *Combined NDT inspection techniques for corrosion detection of aircraft structures*. in *Proc. 15th World Conf. Nondestructive Testing*. 2000.
39. Heger, T., *Erfassung dreidimensionaler Strukturen mit 2D-Bildverarbeitung unter Einsatz gesteuerter Beleuchtung*. 2005: Shaker.
40. Heizmann, M. and F.P. León, *Fusion of image signals*. 2008.
41. Neuschaefer-Rube, U., M. Bartscher, and U. Hilpert. *Application of multisensor measurements and sensor data fusion in coordinate metrology*. in *Workshop & Symposium Metrology's Impact on Business, USA—Proceedings*. 2008.
42. Fan, Y., et al. *Registration of tapping and contact mode atomic force microscopy images*. in *2006 Sixth IEEE Conference on Nanotechnology*. 2006. IEEE.

43. Pohl, C. and J.L. Van Genderen, *Review article multisensor image fusion in remote sensing: concepts, methods and applications*. International journal of remote sensing, 1998. **19**(5): p. 823-854.
44. Zhang, J., *Multi-source remote sensing data fusion: status and trends*. International Journal of Image and Data Fusion, 2010. **1**(1): p. 5-24.
45. Vosselman, G., et al., *Recognising structure in laser scanner point clouds*. International archives of photogrammetry, remote sensing and spatial information sciences, 2004. **46**(8): p. 33-38.
46. seven orgonlziatiarls Supportedthe, T., *Guide to the Expression of Uncertainty in Measurement*. 1995.
47. Institute, A.N.S. and N. International. *American National Standard for Calibration: US Guide to the Expression of Uncertainty in Measurement*. 1997. National Conference of Standards Laboratories.
48. Costa, S.R.R.d., et al., *EA-4/02 Expression of the Uncertainty of Measurement in Calibration*. 1999.
49. Plowucha, W., et al., *Geometrical product specification and verification as toolbox to meet up-to-date technical requirements*. 2014.
50. Guide, I., *99 (2007) International vocabulary of metrology—basic and general concepts and associated terms, VIM*. International Organization for Standardization: Switzerland, 2007.
51. Kunzmann, H. and F. Wäldele, *Performance of CMMs*. CIRP annals, 1988. **37**(2): p. 633-640.
52. Phillips, S.D., et al., *A careful consideration of the calibration concept*. Journal of research of the National Institute of Standards and Technology, 2001. **106**(2): p. 371.
53. Chang, Y.-W., et al., *Training and testing low-degree polynomial data mappings via linear SVM*. Journal of Machine Learning Research, 2010. **11**(4).
54. Gergonne, J.D., *The application of the method of least squares to the interpolation of sequences*. Historia Mathematica, 1974. **1**(4): p. 439-447.
55. Smith, S.W., *The scientist and engineer's guide to digital signal processing*. 1997, California Technical Pub. San Diego.
56. Arce, G., *Nonlinear Signal Processing: A Statistical Approach Wiley: New Jersey*. 2005, USA.
57. Kahu, S.Y., *Figure extraction from scanned electronic theses and dissertations*. 2020, Virginia Tech.
58. Booth, E., J. Mount, and J.H. Viers, *Hydrologic variability of the Cosumnes River floodplain*. San Francisco Estuary and Watershed Science, 2006. **4**(2).
59. Kimeldorf, G.S. and G. Wahba, *A correspondence between Bayesian estimation on stochastic processes and smoothing by splines*. The Annals of Mathematical Statistics, 1970. **41**(2): p. 495-502.
60. Craven, P. and G. Wahba, *Smoothing noisy data with spline functions*. Numerische Mathematik, 1978. **31**(4): p. 377-403.
61. Reinsch, C.H., *Smoothing by spline functions*. Numerische Mathematik, 1967. **10**(3): p. 177-183.
62. Orwiler, B., *Oscilloscope Vertical Amplifiers: Circuit Concepts*. 1969: Tektronix.

63. Andrews, J.R., *Low-pass risetime filters for time domain applications*. Piscosecond Pulse Labs, Boulder, CO, 1999: p. 1-6.
64. Haddad, R.A. and A.N. Akansu, *A class of fast Gaussian binomial filters for speech and image processing*. IEEE Transactions on Signal Processing, 1991. **39**(3): p. 723-727.
65. Grinshpan, A.Z., *An inequality for multiple convolutions with respect to Dirichlet probability measure*. Advances in Applied Mathematics, 2017. **82**: p. 102-119.
66. Ghasemi, S.H. and A.S. Nowak, *Reliability index for non-normal distributions of limit state functions*. Structural Engineering and Mechanics, 2017. **62**(3): p. 365-372.
67. Domínguez, A., *A history of the convolution operation [Retrospectroscope]*. IEEE pulse, 2015. **6**(1): p. 38-49.
68. Diggle, P., *A kernel method for smoothing point process data*. Journal of the Royal Statistical Society: Series C (Applied Statistics), 1985. **34**(2): p. 138-147.
69. Obeid, H., et al., *Evaluation of arterial stiffness by finger-toe pulse wave velocity: optimization of signal processing and clinical validation*. Journal of hypertension, 2017. **35**(8): p. 1618-1625.
70. Fonseca, P., *Application of Homogeneous Transformation Matrices to the simulation of VLP systems*. 2017.
71. Sandwell, D.T., *Biharmonic spline interpolation of GEOS-3 and SEASAT altimeter data*. Geophysical research letters, 1987. **14**(2): p. 139-142.
72. Deng, X. and Z.-a. Tang, *Moving surface spline interpolation based on Green's function*. Mathematical geosciences, 2011. **43**: p. 663-680.